Model Calculations of Current and Density Distributions in Dissipative Hall Bars

Dissertation zur Erlangung des
naturwissenschaftlichen Doktorgrades
der Bayerischen Julius-Maximilians-Universität
Würzburg

vorgelegt von

AFIF SIDDIKI

aus Ankara, Türkei

angefertigt am
MAX-PLANCK-INSTITUT FÜR FESTKÖRPERFORSCHUNG
STUTTGART

Würzburg 2005

Eingereicht am: 17.03.2005
bei der Fakultät für Physik und Astronomie

1. Gutachter: Prof. Dr. R. R. GERHARDTS
2. Gutachter: Prof. Dr. R. KÜMMEL
der Dissertation.

1. Prüfer: Prof. Dr. R. R. GERHARDTS
2. Prüfer: Prof. Dr. R. KÜMMEL
3. Prüfer: Prof. Dr. E. BATKE
im Promotionskolloquium

Tag des Promotionskolloquiums: 30.06.2005

Doktorurkunde ausgehändigt am: .....

Contents

Symbols and Abbreviations

2DES	Two-dimensional electron system .
$2d$	Sample width.
$a_B^* = \bar{\kappa}\hbar^2/(me^2)$	Effective Bohr radius.
$a_0 = a_B^*/2$	Screening length.
$\mathbf{A}$	Vector potential.
a.u.	Arbitrary units .
$\alpha_{sc} = \pi a_0/d$	Screening parameter.
$\mathbf{B}$	Magnetic field strength .
$\widetilde{B} = \hbar\omega_c/E_F$	Dimensionless magnetic field strength.
b	Depletion length.
Chap.	Chapter.
DOS	Density of states .
$D_0 = g_{\rm s}m/2\pi\hbar^2$	Constant density of states of a 2DES.
e	Elementary charge.
E_F	Fermi energy.
E_N	Energy of the Nth Landau level.
$E_0 = 2\pi e^2 n_0 d/\bar{\kappa}$	Pinch-off energy.
$\epsilon(q)$	Dielectric function.
Eq.	Equation.
Fig.	Figure.
$f(\epsilon) = 1/[\exp(\epsilon) + 1]$	Fermi function.
$g_{\rm s}$	Spin degeneracy.
$\hbar$	Planck's constant.
κ	Dielectric constant.
k_B	Boltzmann's constant.
$\bar{\kappa}$	Average dielectric constant.
IS(s)	Incompressible strip(s).
$l = \sqrt{\hbar/m\omega_c}$	Magnetic length.
LL(s)	Landau level(s).

m_0	Electron mass.
m	Effective electron mass($= 0.067m_0$ for GaAs).
μ^*	Electrochemical potential.
ν	Filling factor.
$\bar{\nu}$	Average filling factor.
$\nu(0)$	Filling factor at the center.
$n_0(x)$	Donor (background charge) density.
$n_{el}(x)$	Electron density.
$n_g(x)$	Induced charge density on the gates.
QH	Quantum Hall .
QHE	Quantized Hall effect.
Sec.	Section.
TDOS	Thermodynamic density of states .
TFA	Thomas-Fermi approximation .
TFPA	Thomas-Fermi-Poisson approach.
$\omega_c = eB/mc$	Cyclotron frequency.
$\Omega \equiv \hbar\omega_c$	Cyclotron energy.
Ω_2	Cyclotron energy at average filling factor 2.
$V(\mathbf{r})$	Total electrostatic potential energy.
$V_H(x)$	Hartree potential energy.
$V_{bg}(x)$	Background potential energy.

Chapter 1

Introduction

A two-dimensional electron system (2DES) in a strong perpendicular magnetic field has unusual low-temperature screening properties [1, 2], since the highly degenerate Landau-quantized energy levels lead to a strong variation of the thermodynamic density of states (TDOS) with varying strength of the magnetic field, i.e., with varying filling factor ν of the Landau levels (LLs). If a LL is close to half filled, the TDOS is very high (inversely proportional to the temperature T), and static potential fluctuations are nearly perfectly screened. We will consider only spin-degenerate 2DESs, so that this happens if the value of ν is close to an odd integer, while at even-integer ν the Fermi energy lies in the gap between two adjacent LLs and a spatial redistribution of electrons and, therefore, a screening of (weak) potential fluctuations is impossible. In an inhomogeneous 2DES with sufficiently strong long-range density fluctuations, screening effects lead to quasi metallic (so called "compressible") regions with high TDOS, in which screening is nearly perfect and a LL is "pinned" to the Fermi energy, and to insulator-like "incompressible" regions, which separate adjacent compressible regions. In the incompressible regions the Fermi energy falls into the gap between two LLs and the electron density $n_{\rm el}(\mathbf{r})$ is constant (even-integer filling factor), while in the compressible regions $n_{\rm el}(\mathbf{r})$ adjusts itself so that the self-consistent electrostatic potential energy $V(\mathbf{r})$ of an electron differs from the Fermi energy (more precisely the electrochemical potential μ^*) by a Landau energy $\hbar\omega_c(n + 1/2)$, where $\omega_c = eB/m$ is the cyclotron frequency in the magnetic field B. As a consequence, $V(\mathbf{r})$ becomes nearly constant within a compressible region and differs by integer multiples of $\hbar\omega_c$ between different compressible regions. Landau level pinning and the interplay of compressible and incompressible regions lead to strongly nonlinear screening effects. This screening scenario has been established some time ago [1, 2] and was applied, e.g., to calculate, at zero temperature, the electronic DOS [3] and transport [4, 5] through 2DESs in smooth periodic and random potentials. The explanation [6, 7] of several experimental results [8, 9], relies also on these ideas. A systematic investigation of these interesting nonlinear screening effects was, however, apparently not available in the literature.

Models for half-space and Hall-bar geometries with planar charge distributions have been proposed that allow closed solutions of Poisson's equation (i.e., the calculation of the potential for given electron density), and estimates of position and widths of the incompressible strips have been given [10, 11]. By adding the non-linear Thomas-Fermi approximation for the calculation of the electron density from the potential, that work was extended to a self-consistent approach, which allows to calculate both electron density and electrostatic potential for arbitrary temperature [12, 13]. This approach shows that the existence and the width of incompressible strips depends sensitively on temperature, and allows to calculate their position and width for given background charges without additional assumptions.

On the other hand, the fascinating observation of quantized magneto-resistance, namely the quantized Hall effect (QHE) [14], in such a two-dimensional electron system, drew the attention of both experimental and theoretical physicists to this field. The importance of the quantized Hall effect as resistance standard, and its application for modern metrology, relies on the extremely high reproducibility with an accuracy of better than 10^{-8} of certain quantized resistance values [15]. This extreme reproducibility points to an universal origin, which is independent of special material or sample properties. The microscopic picture of the current distribution and the potential profile still remains as a central question, which many authors addressed considering models even contradicting each other. These models include simple Hartree-type approximations [16], as well as complicated density functional approaches [17, 18]. Experimental information about the actual current and potential distribution in a Hall bar under QHE conditions has been obtained by using electro-optic imaging techniques [19], where Knott *et al.* found that, outside the quantum Hall regime (QHR) Hall potential profiles vary linearly between the two edges. In the QHR, the observed Hall potential profile was nonlinear. They concluded that the electron density inhomogeneities become important as the conductivity strongly depends on the local electron density. Recently Hall potential profiles were measured by Ahlswede and coworkers [20–22] with a scanning force microscope [23]. The data were interpreted in terms of "incompressible strips", with constant electron density [10–13] (corresponding to the filling of an integer number of Landau levels), which are expected to develop in an inhomogeneous 2DES as a consequence of its strongly non-linear low-temperature screening properties [24] in a strong perpendicular magnetic field. If the filling factor in the center of the sample was slightly larger than an integer, the Hall potential was found to drop completely across two strips, while being constant elsewhere. With decreasing B, the strips moved towards the sample edges, just as one expects for the incompressible strips in a sample, in which the electron density decreases gradually from a maximum in the center towards the edges. If the center filling factor was slightly below an integer, a gradual potential variation was observed, either linear or non-linear, without clear indication for incompressible strips [21].

In fact, this current carrying incompressible strip picture was discussed earlier by Chang

[25]. It could not be confirmed by self-consistent equilibrium calculations which imposed a *dissipationless* Hall current as a thermodynamic boundary condition on the 2DES in a Hall bar [13, 26]. In a recent theoretical work of Güven and Gerhardts (GG) [27], the interpretation of the experiments by the means of incompressible strips was supported. In that work, they have extended the self-consistent Thomas-Fermi-Poisson approximation (TFPA) [12, 13, 24] for the calculation of electron density profile and electrostatic potential to a non-equilibrium situation with a position-dependent electrochemical potential, determined by the presence of an applied *dissipative* current through the sample. Electrochemical potential and current density were calculated from a local version of Ohm's law, with a local model for the conductivity tensor, determined by the position-dependent electron density. The feed-back of the current distribution on electron density and the measurable potential profile [21] was included by the assumption of local equilibrium in the stationary non-equilibrium situation.

In agreement with the experiment [21], the calculation [27] shows a linear variation of the Hall potential across the sample if there are no incompressible strips, e.g. for sufficiently high temperature or if the magnetic field is so strong, that the local filling factor is everywhere in the sample less than two (spin-degeneracy is assumed and interactions which might lead to the fractional quantized Hall effect are neglected). Also for center filling factors slightly larger than 2 or 4 the calculation confirms the experiment, showing that the potential drops across broad incompressible strips and is constant elsewhere. However, due to the use of the TFPA, GG [27] obtain incompressible strips whenever the center filling factor is larger than 2 [10–13], and due to the strictly local conductivity model these dominate the current and potential distribution, and lead to vanishing longitudinal resistance. Thus, the model assumptions of Ref. [27] lead to serious disagreement with important aspects of the experiment. We should also note that, in this model the localization effects were not included, which are often considered to be essential for an understanding of the QHE.

In the localization picture, the disorder is necessary to understand the origin of wide Hall plateaus [28] accompanied with the zero longitudinal resistance [29]. The Landau levels are broadened due to impurity scattering and the tails of these levels (localized states) can pin the Fermi level, although they do not contribute to the transport, whereas the extended states carry the Hall current [30]. This scheme was related to a gauge argument that can only give integer values of the Hall conductance [31, 32]. There were many efforts to support this bulk picture as an origin of the QHE which also includes numerical calculations by Ando [33] which show that the localized states exist. A plateau behavior of the average Hall conductivity as a function of the filling factor has also been found [34]. However these localization and transport theories proposed for strong magnetic fields, are not so well developed as the corresponding theory for vanishing magnetic field [35]. On the other hand a classical local magneto-transport model was proposed earlier, which *ad hoc* assumed the existence of a density gradient in the sample and,

thereby, in fact could explain the finite widths of the quantum Hall plateaus without assuming localized states [36, 37]. This mechanism plays an important role in the work of GG and also in a part of the present thesis.

Another interesting (composite) two-dimensional charge system to study screening and magneto-transport is the so called bilayer system. The basic idea is to bring two 2DES into a close proximity, in parallel to each other, perpendicular to the growth direction. For such a system it was predicted, that transport in the active layer will drive the passive layer out of equilibrium. Even if the barrier separating the two layers is high and wide enough to prevent tunneling, the interlayer interactions can still be sufficiently strong. This effect is known as the *drag effect* [38]. With the improvement of the experimental techniques an additional electron or hole layer was also accessible to measure magneto-transport quantities of the bilayer systems. Motivated by the *drag effect* experiments [39–44], both the electrostatic and transport properties of such bilayer systems were investigated theoretically [45–50] within the independent electron picture, however, the self-consistent treatment of screening was left unresolved. On the other hand the direct measurements of the compressibility of the 2DES [51] had revealed regimes of negative thermodynamic compressibility of the interacting 2DES and were in qualitative agreement with the existing theoretical predictions [52]. Recently, a magneto-resistance hysteresis has been reported for the two-dimensional carrier systems [53, 54]. For the GaAs hole bilayer system, Tutuc *et al.* observed hysteretic longitudinal resistance at the magnetic field positions where either the majority (higher density) or minority (lower density) layer is at Landau level filling one. They have argued that the hysteresis is due to a layer-charge instability, which creates domains with different layer densities, whereas for the electron bilayer system Pan *et al.* concluded that, the observed hysteresis is due to a spontaneous charge transfer via the ohmic contacts. The hysteresis is a common phenomenon in magnetic materials, and often indicates a non-equilibrium situation associated with a phase transition and presence of domains [55]. For the particular interest of the present thesis, we would like to draw attention to two experiments, that exhibit hysteresis, and are performed at single layer 2DES Corbino [56] and mesa etched Hall bar [57] geometries. For the Corbino geometry the electron transport below the Fermi level was investigated by measuring charge transfer between contacts. It was observed that the potential difference between inner and outer contacts exhibits hysteresis around integer and fractional filling factors while sweeping the magnetic field in two directions. The results were interpreted as a charge transfer due to the magnetic flux change penetrating to the device, inspired by Laughlin's gedanken experiment [31]. The latter experiment also reports hysteretic behavior, of the local electrostatic potential measured by a single electron transistor. The results were interpreted as the fingerprints of dissipationless eddy currents driven by an induced gradient in the electrochemical potential over the incompressible regions. There it was concluded that, when measuring the Hall resistance while sweeping the magnetic field, the 2DES cannot

be considered as being at thermodynamic equilibrium at the plateau regimes, where one expects incompressible regions.

The goal of this thesis is four fold: First, to investigate nonlinear screening effects in 2DESs, and than resolve the essential interrelation between the quantized Hall plateaus by examining the current distribution. Third, to obtain a qualitative picture of the long-range impurity potential fluctuations. Finally to propose a self-consistent scheme, which explains basic features of the magneto-transport hysteresis observed in the experiments.

This work is organized as follows: In chapter 2 we introduce the essential ingredients of the self-consistent screening theory of a Hall bar under quantum Hall conditions. The Thomas-Fermi-Poisson approach is implemented to different Hall bar geometries in chapter 3 in order to investigate the boundary effects to the screening. Chapter 4 is devoted to construct an explicit relation between the Hall plateaus and the presence of incompressible strips. In the fifth chapter we discuss the effects disorder on a statistical base and provide a simple treatment of the long-range fluctuations which resolves the discrepancies pointed out in the previous chapter. There we also propose a set of experiments concerning sample widths and mobilities. In chapter 6 we extend our model to an electron-electron bilayer system where we also investigate the hysteresis-like effect from the point of screening effects, namely by the formation of compressible and incompressible regions and compare our results with the experimental ones. A short concluding chapter summarizes our findings.

Chapter 2

Electrostatic self-consistency and Approximations

Here we introduce our formalism, which will be used to obtain self-consistent solutions of Poisson equation, considering different boundary conditions and approximations to the solutions of the Schrödinger equation. In principle one has to solve Poisson equation for given boundary conditions and charge distributions in order to obtain the total electrostatic potential $V(\mathbf{r})$, then to use this potential in the Schrödinger equation to calculate energy eigen values and states. The eigen states and energies, in turn, determine the charge distribution so that one should solve the Poisson equation with this new charge profile, self-consistently until a full convergence is obtained.

2.1 Electrostatic self-consistency

Following Ref. [27], we consider a 2DES in the plane $z = 0$, with translation invariance in the y direction and an electron density $n_{\rm el}(x)$ confined to the interval $x_l < x < x_r$. The confinement potential $V_{bg}(x)$ is determined by fixed background charges and appropriate boundary conditions at x_l and x_r. The mutual Coulomb interactions between the electrons are treated in a Hartree-type approximation, i.e., are replaced by a potential energy term $V_H(x)$ which is determined via Poisson's equation by the electron density. Exchange and correlation effects are neglected, and spin degeneracy is assumed. Thus, the electrons move in an effective potential

$$V(x) = V_{bg}(x) + V_H(x), \tag{2.1}$$

$$V_H(x) = \frac{2e^2}{\bar{\kappa}} \int_{x_l}^{x_r} dx'\, K(x,x') n_{\rm el}(x'), \tag{2.2}$$

where $-e$ is the charge of an electron, $\bar{\kappa}$ an average background dielectric constant, and the kernel $K(x,x')$ solves Poisson's equation under the given boundary conditions. The calculation

of the kernels, for the models which are considered in this work, are described in Appendix A.

To perform explicit calculations, one needs a prescription to calculate the electron density for given effective potential $V(x)$, which then together with Eqs. (2.1) and (2.2) completes the electrostatic self-consistency.

2.1.1 Hartree approximation

The most complicated prescription we consider is the Hartree approximation, i.e. we insert $V(x)$ into Schrödinger's equation,

$$\left[\frac{1}{2m}\left(\mathbf{p}+\frac{e}{c}\mathbf{A}\right)^2+V(x)\right]\Phi_\lambda(\mathbf{r})=E_\lambda\Phi_\lambda(\mathbf{r}), \tag{2.3}$$

with $\mathbf{A}(\mathbf{r})$ a vector potential describing the magnetic field $\mathbf{B}=(0,0,B)=\nabla\times\mathbf{A}$, and calculate the density from the eigen-energies E_λ and -functions $\Phi_\lambda(\mathbf{r})$,

$$n_{\rm el}(\mathbf{r})=\sum_\lambda|\Phi_\lambda(\mathbf{r})|^2 f(E_\lambda-\mu^*). \tag{2.4}$$

Exploiting the symmetry of this system, we use the Landau gauge, $\mathbf{A}(\mathbf{r})=(0,Bx,0)$, and factorize the wavefunctions, $\Phi_\lambda(\mathbf{r})=L_y^{-1/2}\exp(iky)\phi_{n,X}(x)$, with L_y a normalization length, $X=-l^2k$ a center coordinate, $l=\sqrt{\hbar/m\omega_c}$ the magnetic length, and $\omega_c=eB/(mc)$ the cyclotron frequency. The Schrödinger equation then reduces to

$$\left[-\frac{\hbar^2}{2m}\frac{d^2}{dx^2}+\frac{m}{2}\,\omega_c^2(x-X)^2+V(x)\right]\phi_{n,X}(x)= E_n(X)\phi_{n,X}(x), \tag{2.5}$$

and the electron density becomes

$$n_{\rm el}(x)=\frac{g_s}{2\pi l^2}\sum_n\int dX\, f(E_n(X)-\mu^*)|\phi_{n,X}(x)|^2, \tag{2.6}$$

where $g_s=2$ takes the spin degeneracy into account and the sum over X has been replaced by an integral, $L_y^{-1}\sum_X\Rightarrow(2\pi l^2)^{-1}\int dX$.

2.1.2 Thomas-Fermi Approximation (TFA)

If the potential $V(x)$ varies slowly on the scale of the magnetic length l, its effect on the lowest Landau levels (LLs) can be treated perturbatively, with the lowest order result

$$E_n(X)\approx E_n+V(X),\quad E_n=\hbar\omega_c(n+1/2). \tag{2.7}$$

On the length scale relevant for the variation of $V(x)$, the extent of the wavefunctions may be neglected, $|\phi_{n,X}(x)|^2 \approx \delta(x - X)$. Then the Hartree result for the electron density, Eq. (2.6), reduces to the TFA [12, 13, 24, 27]

$$n_{\rm el}(x) = \int dE\, D(E)\, f(E + V(x) - \mu^*), \tag{2.8}$$

with $D(E)$ the Landau density of states (DOS), $f(E) = 1/[\exp(E/k_BT) + 1]$ the Fermi function, μ^* the electrochemical potential (being constant in the equilibrium state), k_B the Boltzmann constant, and T the temperature. We will use the Landau DOS described by

$$D(E) = \frac{1}{\pi l^2} \sum_{n=0}^{\infty} \delta(E - E_n), \tag{2.9}$$

as default, unless other definitions are given. To evaluate the self-consistent Thomas-Fermi-Poisson approach (TFPA) we follow Ref. [27]. First we fix the sample width $2d$ and the density of positive background charges n_0, and thereby the background potential $V_{bg}(x)$ and the relevant screening parameter $\alpha_{sc} \equiv \pi a_0/d$, with $a_0 = \bar{\kappa}\hbar^2/(2me^2)$ the screening length. Note that the effective Bohr radius is $a_B^* = 2a_0 = 9.79$ nm for GaAs. Next we choose the actual width $2b$ of the density profile at $T = 0$ and $B = 0$, and solve for $|x| \le b$ the linear integral equation [27]

$$V(x) - V_{bg}(x) = \frac{1}{\alpha_{sc}} \int_{-b}^{b} \frac{dx'}{d}\, K(x, x')\, [\mu_0^* - V(x')], \tag{2.10}$$

[with $\mu_0^* = V(-b) = V(b)$] to which the self-consistent TFPA reduces in this limit, since the corresponding density profile $n_{\rm el}(x; B = 0, T = 0) = D_0[\mu_0^* - V(x)]$, with $D_0 = m/(\pi\hbar^2)$ the DOS of the 2DES at $B = 0$. Then we calculate $V(x)$ for $|x| \le d$ from Eq.(2.10), the average density $\bar{n}_{\rm el} = \int_{-d}^{d} dx\, n_{\rm el}(x; B = 0, T = 0)/2d$ with the corresponding Fermi energy $E_F = \bar{n}_{\rm el}/D_0$, and, for later reference, the Fermi energy $E_F^0 = n_{\rm el}(0; B = 0, T = 0)/D_0$ corresponding to the electron density at the center.

In the following we will consider only symmetric density profiles and take b, or equivalently the depletion length $d - b$, as a free parameter, that fixes the density profile and the electrochemical potential μ_0^* at $B = 0$ (where the temperature dependence is weak). In real samples μ_0^* may be determined by an electron exchange between the 2DES and its surrounding, which may be possible at high but not at low temperatures. A restriction that fixes μ_0^* will also determine the value of b.

Next, at a fixed value of the magnetic field we start with a high temperature to calculate the electron density from Eqs. (2.8) and (2.9) self-consistently with Eq. (2.2), using the previously calculated potential $V(x)$ as initial value. Finally we lower T stepwise until the required low temperature is reached, and iterate (using a Newton-Raphson approach) at each temperature until convergence is achieved.

Chapter 3

TFP theory of screening

3.1 Introduction

The purpose of this chapter is a systematic investigation of the nonlinear low-temperature screening of harmonic electrostatic potential modulations in laterally confined and unconfined 2DESs subjected to a quantizing perpendicular magnetic field. We would like to mention that, the essential arguments and results of this chapter have already been published [24,58]. We will demonstrate that in general edge effects do not qualitatively change the screening properties of the 2DES, even if the sample width is not much larger than the period of the imposed potential modulation. There are, however, peculiar differences between confined and unconfined 2DESs in situations, in which the latter have no states near the Fermi energy. To understand this in detail, we first discuss the screening of a potential modulation imposed on a homogeneous 2DES (Sec. 3.2) and then consider, for two different boundary models, edge effects on screening in Hall bar geometries (Sec. 3.3).

We will assume the 2DES to be located in the plane $z = 0$ with a (surface) number density $n_{\rm el}(x)$ and consider only situations with translation invariance in the y direction. The (Hartree) contribution $V_H(x)$ to the potential energy of an electron caused by the total charge density of the 2DES is given in Eq. (2.2) and the electron density in turn is calculated in the TFA [13] from Eq. (2.8).

The total potential energy of an electron $V(x) = V_{\rm ext}(x) + V_H(x)$, differs from $V_H(x)$ by the contribution due to external charges, e.g., a homogeneous positively charged background and a charge distribution creating a periodic modulation potential. The local (but nonlinear) TFA is much simpler than the corresponding quantum mechanical calculation and expected to yield essentially the same results (see chapter 4) if $V(x)$ varies slowly in space, i.e., on a length scale much larger than typical quantum lengths such as the extent of wave functions or the Fermi wavelength.

3.2 Homogeneous 2DES

Here we consider an unbounded 2DES and add a periodic external modulation described by a potential energy $V_{\rm ext}(x) = V_{\rm ext}(x+a)$. The 2DES will respond with a density modulation and a Hartree potential of the same period a. To exploit the periodicity, we expand density and potentials into Fourier series according to

$$V(x) = \sum_q V^q\, e^{iqx}, \quad V^q = \int_{-a/2}^{a/2} \frac{dx}{a}\, e^{-iqx} V(x), \tag{3.1}$$

with $q = 2\pi n/a$ and integer n. To maintain charge neutrality, $n_{\rm el}^0 = \bar{n}_{\rm el}$ is required in any case. With the boundary conditions $V_H(x,z) \to 0$ for $|z| \to \infty$, Poisson's equation yields (see, e.g., Ref. [59])

$$V_H^q(z) = (2\pi e^2/\bar{\kappa}|q|) e^{-|qz|}\, n_{\rm el}^q \tag{3.2}$$

as response to the density fluctuation $n_{\rm el}^q$. Summing over harmonics (for $q \neq 0$), [60] $V_H(x, z=0)$ from Eq. (2.2) is obtained with the kernel presented in App. A (see Eq. (A.8) as

$$K(x,x') = -\ln\left|2\sin\frac{\pi}{a}(x-x')\right| . \tag{3.3}$$

3.2.1 Breakdown of linear screening

Zero magnetic field

In the limit $B = 0, T \to 0$ and with $E_F = \mu^*(B=0,T=0)$, Eq. (2.8) reduces to

$$n_{\rm el}(x) = D_0 \big(E_F - V(x)\big)\, \theta\big(E_F - V(x)\big), \tag{3.4}$$

which is a linear relation between $V(x)$ and $n_{\rm el}(x)$ for $V(x) < E_F$. With Eq. (3.2), for a harmonic potential modulation $V_{\rm ext}(x) = V_{\rm ext}^q \cos qx$ a harmonic density modulation $\delta n_{\rm el}(x) = n_{\rm el}^q \cos qx$ and the self-consistent ("screened") potential $V(x) = V^q \cos qx$ is found with

$$V^q = V_{\rm ext}^q/\epsilon(q), \quad \epsilon(q) = 1 + Q_0/|q|. \tag{3.5}$$

The dielectric function $\epsilon(q)$ can be expressed in terms of the effective Bohr radius $a_{\rm B}^* = \bar{\kappa}\hbar^2/(me^2)$, since $Q_0 = 2\pi e^2 D_0/\bar{\kappa} = 2/a_{\rm B}^*$. [1, 61] With $q = 2\pi/a$, the screening strength is thus determined by the dimensionless parameter

$$\alpha = \pi a_{\rm B}^*/a. \tag{3.6}$$

We will assume $\alpha \ll 1$, i.e., $\epsilon(q) = 1 + 1/\alpha \gg 1$, so that the TFA is valid for $B \gtrsim 1\,$T, i.e. $l \lesssim 30\,$nm. Since in the linear screening regime the minimum value of the electron density is

$n_{\rm el}(0) = D_0(E_F - V^q)$, linear screening breaks down if the modulation strength becomes so large that $V^q \geq E_F$, i.e., for $V^q_{\rm ext} \geq \epsilon(q)\, E_F$. For larger modulation amplitude the redistribution of electrons is hindered: while the electron density at the minimum of $V_{\rm ext}(x)$ still increases, the electron density at the maximum of $V_{\rm ext}(x)$ cannot decrease further. Instead the density minimum becomes broader. This means that the electrons are depleted from strips along the maxima of $V_{\rm ext}(x)$ and the 2DES breaks off into a system of parallel quasi one-dimensional ribbons. Thus, the imposed harmonic modulation potential $V_{\rm ext}(x)$ now leads to an anharmonic density distribution and, therefore, an anharmonic screened potential [62]. Mathematically, Eq. (2.2) with (A.8) and Eq. (3.4) now represents a nonlinear integral equation that must be solved numerically. In Fig. 3.1 we plot the total variance ${\rm Var}[V] = V(0) - V(a/2)$ of the self-consistently calculated ("screened") potential as a function of the amplitude $V^q_{\rm ext} \equiv V_0$ of the imposed modulation potential for several values of the magnetic field. The result for $B = 0$ and $T = 0$ is shown as a thick solid line. In the linear screening regime, ${\rm Var}[V] \equiv 2V^q = 2V_0/\epsilon(q)$. As linear screening breaks down, a kink appears in the line and the variance increases much faster than in the linear regime. With increasing temperature this kink is rounded off, while the ${\rm Var}[V]$-vs-V_0 curve as a whole is not much affected (shown for $k_BT/E_F = 0.04$ by the open circles in Fig. 3.1). Here and in the following the energies are measured in units of the Fermi energy $E_F = \bar{n}_{\rm el}/D_0$ (for GaAs with $\bar{n}_{\rm el} \approx 3 \cdot 10^{11}\,{\rm cm}^{-2}$, $E_F \approx 10\,{\rm meV}$), and the mean electron density $\bar{n}_{\rm el}$, and thus E_F, is kept constant. We will focus in the following on the regime $V_0 \lesssim \epsilon(q) E_F$, where screening is linear in the limit $B = 0$, $T = 0$.

Half filled Landau levels

With the Landau DOS [see Eq. (2.9)] and the definition of a position-dependent chemical potential, $\mu(x) = \mu^* - V(x)$, Eq. (2.8) yields

$$n_{\rm el}(x) = \hbar\omega_c D_0 \sum_n f\big([E_n - \mu(x)]/k_BT\big). \tag{3.7}$$

The argument of the Fermi function may also be written as $E_n(x) - \mu^*$ and may be interpreted as position-dependent Landau energies, $E_n(x) = E_n + V(x)$, which is correct if the Thomas-Fermi approximation holds. It will be useful to define, in addition to the average LL filling factor $\bar{\nu} = 2\pi l^2 \bar{n}_{\rm el}$, a local filling factor $\nu(x) = 2\pi l^2 n_{\rm el}(x)$.

For $k_BT \ll \hbar\omega_c$ and a homogeneous 2DES with partly filled n-th Landau level, $\mu \sim E_n$, $\bar{\nu} = 2n + \nu_n$, $\nu_n \approx 2f(E_n - \mu)$ is the filling factor of the n-th Landau level. The TDOS is [1]

$$D_T(\mu; B) \equiv \frac{\partial \bar{n}_{\rm el}}{\partial \mu} = \frac{\hbar\omega_c}{k_BT}\,\frac{\nu_n}{2}\left(1 - \frac{\nu_n}{2}\right) D_0\,, \tag{3.8}$$

which is peaked around $\mu = E_n$ with a maximum value $\hbar\omega_c D_0/(4k_BT)$ and a width of order k_BT [a crude approximation is $D_T(\mu; B) \approx (\hbar\omega_c D_0/4k_BT)\theta(2k_BT - |E_n - \mu|)$]. Linearizing

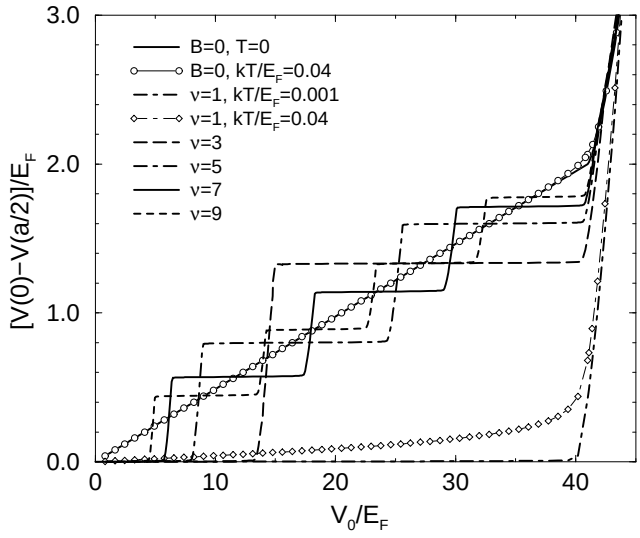

Figure 3.1: Variance of the screened potential versus amplitude of the harmonic potential modulation imposed on a spin-degenerate homogeneous 2DES with a half filled Landau level, for several odd-integer values of the filling factor. Default temperature $k_BT/E_F = 0.001$, $\epsilon(q) = 41$.

Eq. (3.7) with respect to the screened potential $V(x)$, one obtains the Eq. (3.5) with Q_0 replaced by $Q_B = Q_0 D_T(\mu; B)/D_0 \gg Q_0$,

$$\epsilon(q; B) = 1 + \frac{\hbar\omega_c}{k_BT}\,\frac{\nu_n}{2}\left(1 - \frac{\nu_n}{2}\right)\frac{Q_0}{|q|}\,. \tag{3.9}$$

For exactly half filling, $\mu = E_n$, this is a rather good approximation, as can be seen from Fig. 3.1, which shows numerical results for $\bar{\nu} = \nu_0 = 1$ ($n = 0$) at two different temperatures (two lowest curves at $V_0/E_F > 15$). One sees that the screening at finite magnetic field depends much stronger on temperature than at $B = 0$. The linear approximation breaks down, if the amplitude of the screened potential becomes of the order $2k_BT$.

This yields, in the limit of low temperatures and for $\nu_n = 1$, the estimate for the linear screening regime,

$$\frac{V^q_{\rm ext}}{E_F} \lesssim \epsilon(q; B)\frac{2k_BT}{E_F} \approx \frac{\epsilon(q)}{\bar{\nu}}\,, \tag{3.10}$$

with $\epsilon(q) = \epsilon(q; B = 0) = 1 + 1/\alpha$. For a larger modulation the redistribution of electrons within the considered LL is not efficient enough to screen the imposed modulation potential, and similar to the $B = 0$ case, the variance of the screened potential increases much stronger than in the linear regime. In Fig. 3.1 we show low-temperature ($k_BT/E_F = 0.001$) results for odd-integer $\bar{\nu}$ values, calculated numerically from Eqs. (2.2), (A.8), and (3.7). For this temperature,

the linear increase of the screened potential with the applied modulation amplitude V_0 is not resolved on the scale of Fig. 3.1. However the rapid increase of the variance of the screened potential at $V_0/E_F \sim \epsilon(q)/\bar{\nu}$ is clearly seen for the indicated $\bar{\nu}$ values.

For $\bar{\nu} = 1$ the situation is very similar to the $B = 0$ case, apart from the fact that screening in the linear regime is much stronger ("perfect screening", "pinning of lowest LL to Fermi level") due to the higher DOS. For $\bar{\nu} > 1$ new phenomena occur, which we will now discuss.

3.2.2 Emergence of incompressible strips

Odd-integer filling factor $\bar{\nu}$

I start with filling factor $\bar{\nu} = 3$ and investigate the changes of the electron density (Fig. 3.2) and of the total potential (Fig. 3.3) with increasing amplitude V_0 of the imposed modulation $V_{\rm ext}(x) = V_0 \cos qx$, giving explicit results for the six typical V_0 values indicated by open circles in Fig. 3.2.

For $V_0 = 11\, E_F$, close to the breakdown of linear screening (case 1), the density is strongly modulated (see thin line in lower inset of Fig. 3.2), but the modulation appears still cosine-like. The potential is so effectively screened that the second-lowest LL ($n = 1$) is pinned (within a few k_BT) to the Fermi energy [see Fig. 3.3(1)]. For case 2, $V_0 = 13.7\, E_F$, the total potential has developed locally confined maxima and minima, while it remains rather flat in between [Fig. 3.3(2)]. Near these extrema $|E_1(x) - \mu^*|$ becomes so large that the LL $n = 1$ is completely occupied (near $x = a/2$) or empty (near $x = 0$), and incompressible strips with local filling factors $\nu(x) = 4$ and $\nu(x) = 2$ develop near the potential minima and maxima, respectively [see thick solid line in the lower inset of Fig. 3.2, and Fig. 3.3(2)]. Increasing the modulation to $V_0 = 14.5\, E_F$ (case 3) leads to more pronounced local extrema and broader incompressible strips, but does not change the situation qualitatively. The overall change of the density distribution is rather small (see lower inset of Fig. 3.2), indicating poor screening. Indeed the slope of the Var$[V]$-vs-V_0 curve in this regime is $\Delta{\rm Var}/\Delta V_0 \approx 1$, i.e., only slightly smaller than in the absence of any screening, which would yield $\Delta{\rm Var}/\Delta V_0 = 2$. Note that in the incompressible strips the local filling factor (i.e., the density) is constant, while in the pinning regions, i.e., the compressible strips, the screened potential still has a finite slope, proportional to k_BT. [12]

As V_0 increases further to case 4 ($V_0 = 17\, E_F$), the modulation becomes so strong that the maximum of the lowest LL, $E_0(0)$, and the minimum of the lowest unoccupied LL, $E_2(a/2)$, reach the Fermi level μ^* (to within k_BT). Then thermal population of the higher LL ($n = 2$ near $x = a/2$) and depletion of the lower LL ($n = 0$ near $x = 0$) starts and compressible strips emerge in the center of each incompressible strip [see dashed line in the upper inset of Fig. 3.2 and Fig. 3.3(4)]. Further increase of V_0 up to $V_0 = 38.5\, E_F$ (case 5) widens the compressible

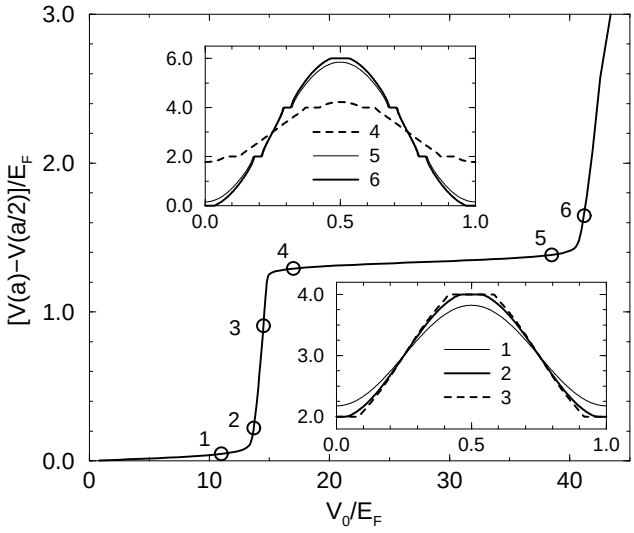

Figure 3.2: Variance of the total potential versus V_0, for average filling factor $\bar{\nu} = 3$. The insets show the local filling factor $\nu(x)$ in one modulation period ($0 \leq x/a \leq 1$) for the six V_0 values indicated by circles. Parameters: $k_BT/E_F = 0.01$, $\epsilon(q) = 41$, $q = 2\pi/a$.

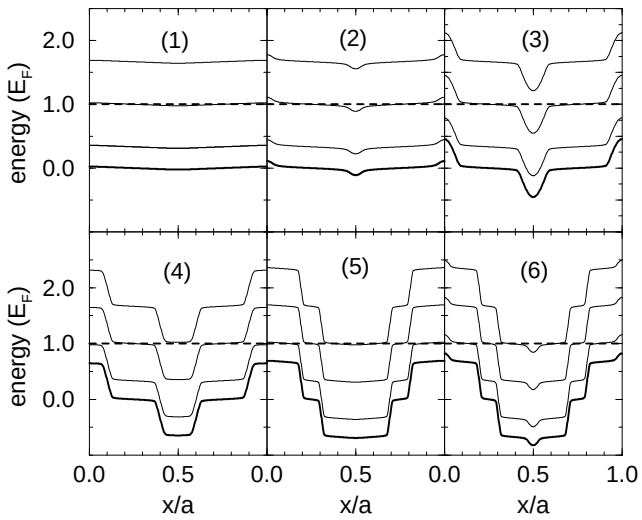

Figure 3.3: Total potential (thick solid lines) and the three lowest of the corresponding Landau levels (thin solid lines) together with the electrochemical potential (thick dashes lines) for the six V_0 values indicated in Fig. 3.2. Parameters as in that figure.

strips and leads to a strong increase of the density modulation due to a redistribution of electrons from the $n = 0$ to the $n = 2$ LL. This results in a strong screening, similar to that in the linear screening regime at weak modulation, and, apart from a weak increase with a slope proportional to k_BT, the variance $\mathrm{Var}[V] = V(0) - V(a/2)$ remains constant at the value $\mathrm{Var}[V] = \mu^* - E_0(0) - [\mu^* - E_2(a/2)] = 2\hbar\omega_c$. This plateau behavior of the Var$[V]$-vs-V_0 curve is obviously an immediate consequence of the pinning of LLs to the Fermi level, i.e., of the nearly perfect screening.

In case 5 a situation is reached in which the lowest ($n = 0$) LL is nearly empty at the potential maximum and the higher ($n = 2$) LL nearly full at the potential minimum. In case 6 ($V_0 = 41.2\, E_F$) the total potential again develops local extrema, similar to the situation depicted in Fig. 3.3(2). But now the incompressible strip created at the potential maximum is due to the depopulation of the lowest LL, i.e., due to vanishing electron density. With further increasing V_0 the depletion regions become wider and the density near the potential minima increases, but screening remains much poorer than in the plateau region.

From Fig. 3.2 it is seen that the global appearance of the density modulation, apart from a fine-structure related to the incompressible strips, is more or less cosine-like. I will use this finding for a rough estimate of the plateau width of the Var$[V]$-vs-V_0 curves. First we conclude from the cosine-like form of the induced density variation that in the high-screening plateau region, along with Eqs. (3.2) and (3.5), the first relation of Eq. (3.10) holds qualitatively and relates the changes δV of the total potential to the changes δV_0 of the externally applied potential by $\delta V \sim \delta V_0/\epsilon(q;B)$. For $Q/|q| \gg 1$, this yields for the change of the variance $\mathrm{Var}[V]$ across the plateau of width ΔV_0

$$\Delta\mathrm{Var}[V] \sim \frac{8k_BT}{\hbar\omega_c\epsilon(q)}\Delta V_0\,, \tag{3.11}$$

i.e., an estimate for the slope of the Var$[V]$-vs-V_0 curve in the plateau region. Since the modulation induces density changes δn_{el} mainly within the compressible regions of high TDOS, we estimate $\delta n_{\mathrm{el}} \sim -D_T(\mu;B)\delta V \sim -(\hbar\omega_c/4k_BT)D_0\delta V$ (which holds for $\nu_n = 1$ and $|\delta V| \lesssim 2k_BT$). In terms of $\delta\nu = 2\pi l_m^2\delta n_{\mathrm{el}}$ this yields $\delta V \sim 2k_BT\delta\nu$, and together with Eq. (3.11) the relation

$$\frac{\Delta V_0}{E_F} \sim \frac{\epsilon(q)}{2\bar\nu}\Delta\mathrm{Var}[\nu] \tag{3.12}$$

between the plateau width ΔV_0 and the change of the filling factor variance $\mathrm{Var}[\nu] = \nu(a/2) - \nu(0)$ (defined at fixed V_0) across the plateau. This criterion applies also to the small-V_0 linear-screening regime, in which $\nu(x)$ varies within the same LL, with $\mathrm{Var}[\nu]$ increasing from 0 to 2, i.e. $\Delta\mathrm{Var}[\nu] = 2$ [see Eq. (3.10)]. The resulting width of the linear-screening regime, $\Delta V_0/E_F \approx \epsilon(q)/\bar\nu$, describes the numerical results of Fig. 3.1 for odd-integer $\bar\nu = 2n+1$ quite well. From the discussion of Figs. 3.2 and 3.3 one expects that, for $n > 0$ the linear regime of

the $\mathrm{Var}[V](V_0)$ curve is terminated by a step of height $2\hbar\omega_c = 4E_F/\bar{\nu}$, which is followed by a plateau. While V_0 sweeps through the plateau, in addition to the LL with index n the two LLs with indices $n-1$ and $n+1$ are locally pinned to the Fermi level and lead to a total change $\Delta\mathrm{Var}[\nu] = 4$ [for $\bar{\nu} = 3$ from $\mathrm{Var}[\nu] = \nu(a/2) - \nu(0) = 2$ on the left side to $\mathrm{Var}[\nu] = 6$ on the right side of the plateau, as seen from the upper inset of Fig. 3.2]. This yields the plateau width $\Delta V_0/E_F \approx 2\epsilon(q)/\bar{\nu}$. If $n-1 = 0$, the plateau will be followed by the breakdown regime. If $n-1 > 0$, the plateau will be followed by a further step of the same height to a plateau of the same width.

To summarize: at very low temperatures and odd-integer filling factors $\bar{\nu} = 2n+1$, the variance $\mathrm{Var}[V]$ of the screened potential as function of the imposed modulation amplitude V_0 shows a linear screening regime for $V_0 \lesssim \epsilon(q)E_F/\bar{\nu}$ which is followed by n successive steps of height $2\hbar\omega_c = 4E_F/\bar{\nu}$ and width $\Delta V_0 \approx 2\epsilon(q)E_F/\bar{\nu}$. The plateau of the n-th step ends at the breakdown of the 2DES into a pattern of isolated 1D systems, which leads to poor screening and is indicated in the $\mathrm{Var}[V](V_0)$ curve by a slope of order unity. At finite temperature, the plateaus assume finite positive slopes, which are estimated from Eq. (3.11) as $\Delta\mathrm{Var}[V]/\Delta V_0 \approx 4\bar{\nu}k_BT/[\epsilon(q)E_F]$. These results, which describe the content of the numerically calculated Figs. 3.1- 3.3 very well, depend, of course, on the high symmetry of the situations considered so far.

Even-integer filling factor $\bar{\nu}$

Another situation of high symmetry is that of an even-integer filling factor $\bar{\nu} = 2n+2$, where n is the index of the highest occupied LL and the Fermi energy $E_F = \hbar\omega_c(n+1)$ lies in the middle between two adjacent LLs. According to Eqs. (3.10) and (3.9), the linear screening regime shrinks to zero, since $\nu_n = 2$. Thus, at very low temperature ($k_BT \ll \hbar\omega_c/2$) a weak modulation $V_{\mathrm{ext}}(x) = V_0 \cos qx$ will not be screened, i.e., the local filling factor will be independent of the modulation, $\nu(x) \equiv \bar{\nu}$, and the total potential will equal the external one, with variance $\mathrm{Var}[V](V_0) = 2V_0$. This situation changes when the modulation potential becomes so large that $|V_0 - \hbar\omega_c/2| \sim k_BT$, i.e., the maximum energy $E_n(0)$ of the highest occupied, and the minimum energy $E_{n+1}(a/2)$ of the lowest unoccupied LL approach the Fermi energy. Then, with increasing V_0 the LL n is depleted near $x = 0$ while the LL $n+1$ is populated near $x = a/2$, forming compressible strips with local filling factors $\nu(x) < \bar{\nu}$ and $\nu(x) > \bar{\nu}$, respectively.

This is demonstrated in the inset of Fig. 3.4, which shows the local filling factor $\nu(x)$ for $k_BT/E_F = 0.001$ and the average filling factor $\bar{\nu} = 2$, i.e., $\hbar\omega_c = E_F$, and for the modulation strengths V_0 indicated by circles in the main figure. For $V_0/E_F = 0.45$ in the non-screening region the deviation $[\nu(x) - \bar{\nu}]$ is practically zero (numerically $< 10^{-6}$), while for $V_0/E_F = 0.6$ it is finite, although small (in the inset enhanced by a factor of 20), with narrow compressible strips. Between $V_0/E_F = 0.5$ and $V_0/E_F \approx 41$ the width of the compressible strips and the

deviation $[\nu(x) - \bar{\nu}]$ increase continuously, while the variance $\mathrm{Var}[V] \approx \hbar\omega_c = E_F$ remains constant. Since screening is due to the redistribution of electrons at the Fermi energy, i.e., to

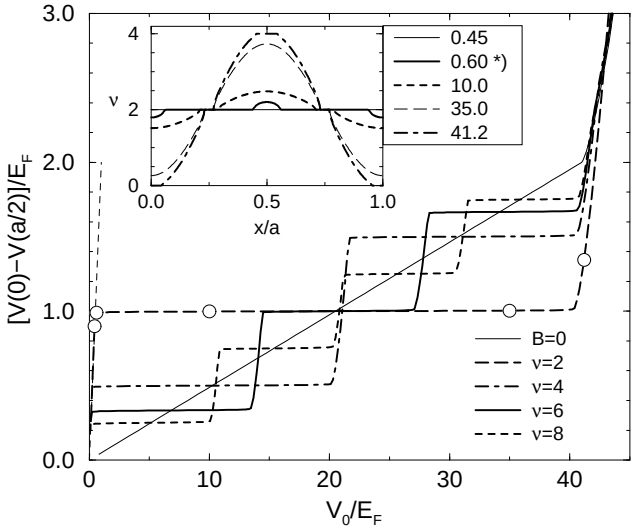

Figure 3.4: As in Fig. 3.1 but for even-integer values of $\bar{\nu}$ ($k_BT/E_F = 0.001$, $\epsilon(q) = 41$). The thin solid line indicates the result for $B = 0$, $T = 0$, the thin dashed line has slope 2. The inset shows the local filling factor $\nu(x)$ in one modulation period for average filling $\bar{\nu} = 2$ and the five values of V_0 indicated by circles in the main figure. *) For $V_0/E_F = 0.60$ the deviation $[\nu(x) - 2]$ is enhanced by a factor 20.

electrons in the compressible strips where the TDOS is large, Eq. (3.12) may again be used to estimate the plateau width. At the beginning of the first plateau the filling factor is constant, $\nu(x) \equiv \bar{\nu}$, i.e., $\mathrm{Var}[\nu] = 0$. At the end of the plateau, the LL n is depleted at the potential maximum, $\nu(0) = \bar{\nu} - 2$, and at the potential minimum the LL $n + 2$ is full, $\nu(a/2) = \bar{\nu} + 2$, i.e., $\mathrm{Var}[\nu] = 4$. Thus, Eq. (3.12) has to be used with $\Delta\mathrm{Var}[\nu] = 4$ and we obtain for the plateau width $\Delta V_0 \sim 2\epsilon(q)E_F/\bar{\nu}$.

This estimate is obviously in good agreement with the numerical calculations presented in Fig. 3.4. For filling factor $\bar{\nu} = 2$, i.e., $n = 0$, the first plateau ends at the transition to the poor-screening breakdown regime, since then the lowest LL $n = 0$ is completely depleted at the potential maxima (thick dash-dotted line in inset of Fig. 3.4). For $\bar{\nu} = 2n + 2$ with $n > 0$ a behavior similar to that discussed in Fig. 3.3 occurs. As V_0 increases slightly beyond the plateau regime, a narrow local maximum of $V(x)$ develops near $x = 0$, accompanied with an incompressible strip of filling $\nu(x) = 2n$ due to the local depletion of the LL n. Simultaneously, a narrow local minimum of $V(x)$ develops near $x = a/2$, accompanied with an incompressible

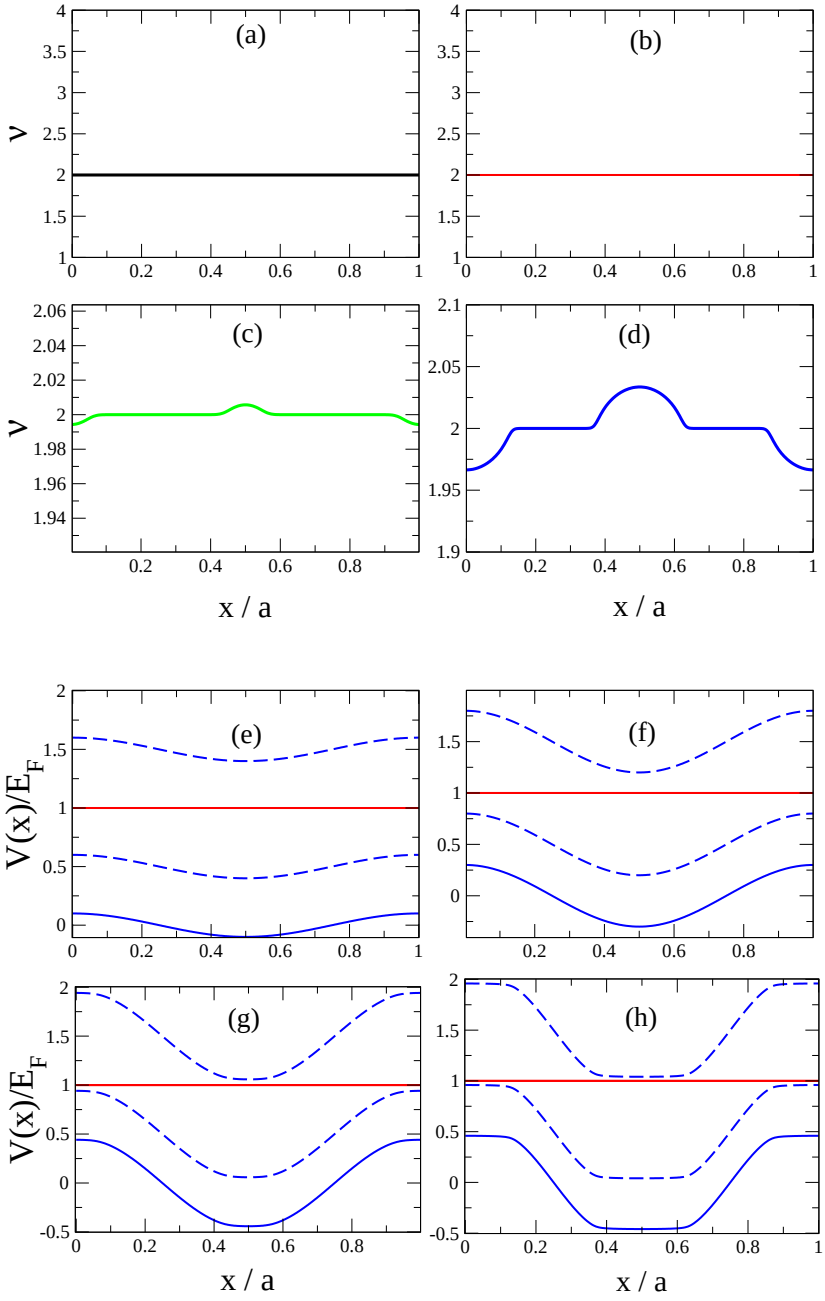

Figure 3.5: The local filling factors [a]-[d] and the total potential (solid lines) together with two lowest Landau levels (dashed lines) and electrochemical potential (thin solid line) [e]-[h]. Calculated for $V_0/E_F = 0.10$ [a,e], 0.45 [b,f], 0.60 [c,g], 1.20 [d,h].

strip of filling $\nu(x) = 2n + 4$ due to the local occupation of the LL $n + 2$. Then, in a narrow V_0 interval these new extrema become more pronounced and the accompanied incompressible strips widen a little. However, the accompanied density change is small, resulting in a poor screening and a rapid increase of the $\mathrm{Var}[V](V_0)$ curve. This interval ends when the new maximum $E_{n-1}(0)$ of the Landau level $n-1$ and the new minimum $E_{n+2}(a/2)$ of the LL $n+2$ come close to the Fermi level (within a few k_BT). Then, with further increasing V_0, new compressible strips open at the locations of the potential extrema, and a plateau region of the $\mathrm{Var}[V](V_0)$ curve with "perfect" screening sets in. One thus again finds a step behavior like in Fig. 3.1 with step height $\Delta\mathrm{Var}[V] = 2\hbar\omega_c = 4E_F/\bar{\nu}$. During the V_0 sweep through the corresponding plateau the LL $n - 1$ will be depleted near $x = 0$ while the LL $n + 2$ is occupied near $x = a/2$. Thus, the plateau width can be estimated from Eq. (3.12) with $\Delta\mathrm{Var}[\nu] = 4$. The last plateau is the one corresponding to the local depletion of the $n = 0$ LL.

In summary, for $\bar{\nu} = 2n + 2$ and very low temperature, the $\mathrm{Var}[V](V_0)$ curve shows a linear increase with slope 2 for $0 \le V_0 \le E_F/\bar{\nu}$, followed by a plateau of height $\hbar\omega_c = 2E_F/\bar{\nu}$ and width $\Delta V_0 \sim 2\epsilon(q)E_F/\bar{\nu}$. This plateau is followed by n steps of height $2\hbar\omega_c$ and approximately the same width ΔV_0. The plateau of the last step is followed by the breakdown regime.

Non-integer filling factor $\bar{\nu}$

In Fig. 3.6 we show $\mathrm{Var}[V](V_0)$ curves for a few non-integer values of the average filling factor $\bar{\nu} = 2n + \nu_n$, with $0 < \nu_n < 2$. Although these results may, at a first glance, look confusing, we will now demonstrate, that they can easily be understood, and even predicted, from a few simple principles.

To estimate the width of the linear screening regime at small V_0 values, we follow the reasoning of Sec. 3.2.1. There we made a linear approximation to the Taylor expansion of $n_{\mathrm{el}}(x)$ with respect to $V(x)$ [see Eq. (3.7)], i.e. $V^q_{\mathrm{ext}} \approx \epsilon(q; B)V^q$. However, note that this approximation does no longer hold for $|V(x)| \sim 2k_BT$, since for $\nu_n \neq 1$ the second order term [$\propto \partial^2 n_{\mathrm{el}}/\partial\mu^2 = (\partial n_{\mathrm{el}}/\partial\mu)(1-\nu_n)/k_BT$] yields already noticeable contributions for smaller $V(x)$. This is taken into account by using the linear approximation only for $|V(x)| \lesssim 2k_BT/(1 + |1 - \nu_n|)$, which essentially implies a upper boundary for the linear screening regime

$$\frac{V_0}{E_F} \lesssim \frac{\epsilon(q)}{\bar{\nu}} \, \frac{\nu_n(2 - \nu_n)}{1 + |1 - \nu_n|} \, . \tag{3.13}$$

For $\nu_n = 1$ this reduces to the estimate (3.10). But in addition, Eq. (3.13) states that for even-integer filling, $\nu_n \to 0$ or $\nu_n \to 2$, the linear screening regime shrinks to zero, and it provides a good description of the widths of the linear screening regimes in the examples shown in Fig. 3.6.

We will now use Eq. (3.12) to obtain estimates of the plateau widths and heights of the $\mathrm{Var}[V]$-vs-V_0 curves, which contain the estimate (3.13) for the linear screening regime as a special case. The estimates are based on the observation that in all cases we have studied

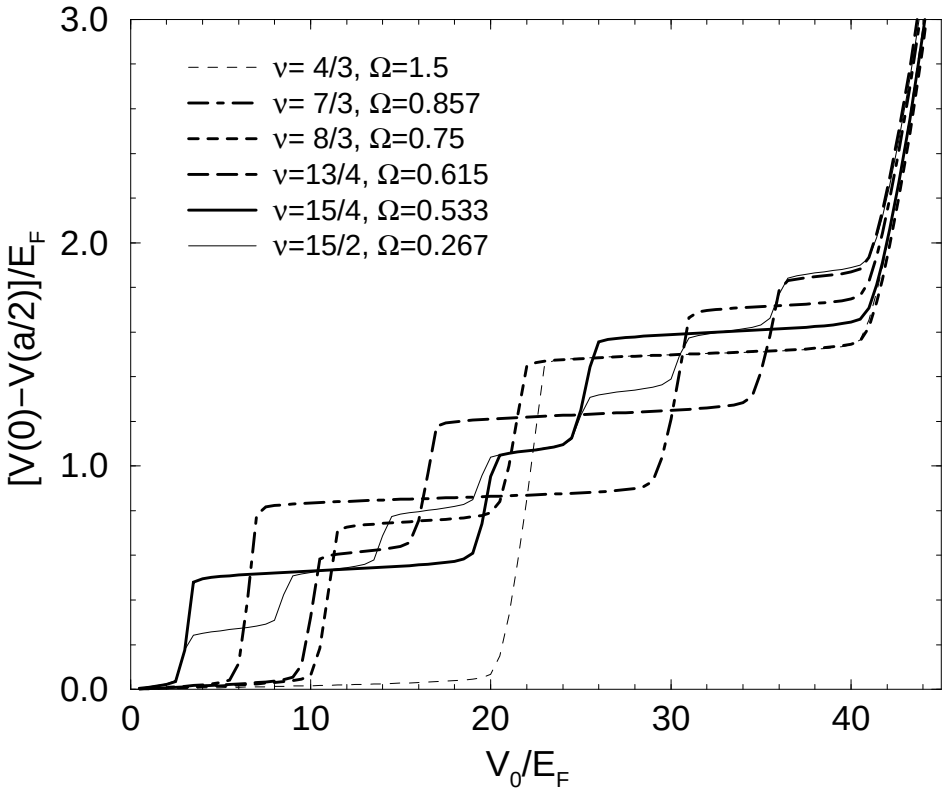

Figure 3.6: As in Fig. 3.1 but for some non-integer values of the (average) filling factor and for higher temperature, $k_BT/E_F = 0.01$ ($\epsilon(q) = 41$).

the density modulation is nearly symmetric about the average density, so that the average of extreme values of the local filling factor is close to the average filling, $\nu(0) + \nu(a/2) \approx 2\bar{\nu}$. Nearly perfect screening occurs, if at both the potential maxima and the minima a single LL is pinned to the Fermi level, so that electrons can easily be redistributed between these LLs and both $\nu(0)$ and $\nu(a/2)$ are different from even integers. If, with increasing V_0, $\nu(0)$ approaches an even integer value, $\nu(0) = 2k$, the LL k is depleted at $x = 0$ and a local maximum of $V(x)$ starts to develop there. Screening remains poor, and $\mathrm{Var}[V](V_0)$ increases rapidly, until the LL $k-1$ reaches the Fermi level at $x = 0$. Then a step of height $\hbar\omega_c$ is completed and the next plateau with perfect screening starts. A similar step begins as $\nu(a/2)$ reaches the value $2k'$. Then the LL $k'-1$ is completely filled at $x = a/2$ and a local potential minimum starts to develop there. Perfect screening begins again, if the LL k' reaches Fermi level at $x = a/2$ and the increase of $\mathrm{Var}[V](V_0)$ by $\hbar\omega_c$ is completed.

We combine now these consideration with the estimate (3.12). For convenience, we introduce the dimensionless variables

$$v = \frac{V}{E_F} \quad v_0 = \frac{V_0}{\epsilon(q)E_F}\,, \quad \Omega = \frac{\hbar\omega_c}{E_F} = \frac{2}{\bar{\nu}}\,, \tag{3.14}$$

and focus on the regime $0 < v_0 < 1$, in which for $T = 0$ and $B = 0$ screening is linear and leads to $\mathrm{Var}[v](v_0) = 2v_0$. To keep the discussion simple, the two possible cases of non-integer $\bar{\nu} = 2n + \nu_n$ are considered separately.

For $0 < \nu_n < 1$**,** the end of the linear screening region, where $v \ll \Omega$, is reached when $\nu(0) = 2n$. Then $\nu(a/2) \approx \bar{\nu} + \nu_n$ and $\mathrm{Var}[\nu] = 2\nu_n$, and across the linear screening regime $\Delta\mathrm{Var}[\nu] = 2\nu_n$ is found. According to Eq. (3.12), linear screening ends at $V_0/E_F \sim \epsilon(q)\nu_n/\bar{\nu}$, in agreement with Eq. (3.13). Neglecting potential variations $\propto k_B T \ll \Omega$, note

$$\mathrm{Var}[v] \approx 0\,, \quad \text{if} \quad 0 < v_0 < 1 - n\Omega\,, \tag{3.15}$$

since $\nu_n = \bar{\nu} - 2n$ and $\Omega = 2/\bar{\nu}$. If $n = 0$, larger V_0 lead to the poor-screening quasi 1D ribbon regime.

For $n > 0$, the next plateau terminates when $\nu(a/2) = 2n+2$. Then $\nu(0) \approx 2n - 2(1-\nu_n)$, i.e., $\mathrm{Var}[\nu] = 2(2-\nu_n)$. Across this plateau one has $\Delta\mathrm{Var}[\nu] = 4(1-\nu_n)$, and with Eq. (3.12) $\Delta V_0 \approx 2\epsilon(q)E_F(1-\nu_n)/\bar{\nu}$. This yields $\Delta v_0 \approx (2n+1)\Omega - 2$ and

$$\mathrm{Var}[v] \approx \Omega\,, \quad \text{if} \quad 1 - n\Omega < v_0 < (n+1)\Omega - 1\,. \tag{3.16}$$

This plateau is followed by another one along which $\nu(0)$ decreases to $2(n-1)$, while $\nu(a/2)$ increases to $\approx 2n+2+2\nu_n$ and thus $\mathrm{Var}[\nu]$ to $4+2\nu_n$. Thus, across that plateau $\Delta\mathrm{Var}[\nu] = 4\nu_n$ and $\Delta v_0 = 2 - 2n\Omega$ is found, which leads to

$$\mathrm{Var}[v] \approx 2\Omega\,, \quad \text{if} \quad (n+1)\Omega - 1 < v_0 < 1 - (n-1)\Omega\,. \tag{3.17}$$

If $n = 1$, this plateau is followed by the poor screening quasi 1D ribbon regime. If $n > 1$, one is in the same situation as at the end of the low-V_0 linear screening regime, and a double step of total width Ω, consisting of one step of height Ω and plateau width $\Delta v_0 = (2n+1)\Omega - 2$ and another one of height Ω and width $\Delta v_0 = 2 - 2n\Omega$, will follow. Thus, one obtains for $0 < k \leq n$

$$\begin{aligned} \mathrm{Var}[v] &\approx (2k-1)\Omega\,, \quad \text{if} \qquad (3.18)\\ &\quad 1-(n+1-k)\Omega < v_0 < (n+k)\Omega - 1\,, \\ \mathrm{Var}[v] &\approx 2k\Omega\,, \quad \text{if} \qquad (3.19)\\ &\quad (n+k)\Omega - 1 < v_0 < 1-(n-k)\Omega\,. \end{aligned}$$

Thus, the linear screening regime is followed by n double steps, which sum up to a total width $\Delta v_0 = 1$, and on the last plateau (before breakdown) one has $\mathrm{Var}[v] = 2(1 - \nu_n/\bar{\nu})$. For $0 < \nu_n < 0.5$, the first plateau of the double step is wider than the second one, as for the dash-dotted line in Fig. 3.6 ($\bar{\nu} = 2.33$), while for $0.5 < \nu_n < 1$ the second plateau of the double step is the wider one, as for the short-dashed line ($\bar{\nu} = 2.67$).

Three limits should be mentioned. For $\nu_n \to 0$ the low-V_0 linear screening regime shrinks to zero and the first plateau of the double step exhausts its full width, so that the second step merges with the first one of the following double step. Thus, at small V_0 a step of height Ω, followed by steps of the double height 2Ω is observed, and all plateaus have the same widths, $\Delta v_0 = \Omega$, as it has been found previously. For $\nu_n = 0.5$ one gets an even number of steps which all have the same heights and widths. For $\nu_n \to 1$ the width of the first plateau of each double step shrinks to zero, so that the low-V_0 linear screening regime is followed by steps of height 2Ω and width $\Delta v_0 = \Omega$, as it was seen before.

For $1 < \nu_n < 2$**,** one has at the end of the linear screening regime $\nu(a/2) = 2n + 2$ and $\nu(0) \approx 2n + 2(\nu_n - 1) > 2n$, with $\mathrm{Var}[\nu] = 2(2 - \nu_n)$. From Eq. (3.12) one obtains

$$\mathrm{Var}[v] \approx 0\,, \quad \text{if} \quad 0 < v_0 < (n+1)\Omega - 1\,, \qquad (3.20)$$

and sees that now the linear screening regime is always followed by a step of height Ω to a plateau of perfect screening. For $n = 0$ (i.e., $1 < \Omega < 2$) this plateau covers the interval $\Omega - 1 < v_0 < 1$ (see e.g., thin dashed line of Fig. 3.6 for $\bar{\nu} = 1.33$). To estimate for $n > 0$ height and width of the following steps and plateaus, respectively, we proceed as before, exploiting that at the end of each plateau either $\nu(0)$ or $\nu(a/2)$ reaches an even integer value, and that

$\nu(0) + \nu(a/2) \approx 2\bar{\nu}$. The result is, for $0 < k \leq n$, a double step of total width Ω,

$$\begin{aligned} \mathrm{Var}[v] &\approx (2k-1)\Omega\,, \quad \text{if} \\ &\quad (n+k)\Omega - 1 < v_0 < 1 - (n+1-k)\Omega\,, \end{aligned} \tag{3.21}$$

$$\begin{aligned} \mathrm{Var}[v] &\approx 2k\Omega\,, \quad \text{if} \\ &\quad 1 - (n+1-k)\Omega < v_0 < (n+k+1)\Omega - 1\,, \end{aligned} \tag{3.22}$$

which is followed by a final single step,

$$\mathrm{Var}[v] \approx (2n+1)\Omega\,, \quad \text{if} \quad (2n+1)\Omega - 1 < v_0 < 1\,, \tag{3.23}$$

of height Ω and plateau width $2-(2n+1)\Omega$. The linear screening regime [width $(n+1)\Omega-1$], the n double steps and this final plateau cover together the interval $0 < v_0 < 1$, as in the case $0 < \nu_n < 1$. The variance of the screened potential in the last plateau is $\mathrm{Var}[v] = 2[1-(\nu_n-1)/\bar{\nu}]$.

For $1 < \nu_n < 1.5$ the first plateau of each double step is wider than the other plateaus, as seen in Fig. 3.6 for the long-dashed line ($\bar{\nu} = 3.25$), which exhibits one double step following the initial single step. For $1.5 < \nu_n < 2$ these first plateaus are the narrower ones, as seen for the thick solid line ($\bar{\nu} = 3.75$). For $\nu_n = 1.5$, the double steps consist of two individual steps of equal heights and plateau widths, as is illustrated by the thin solid line ($\bar{\nu} = 7.5$).

In the limit of odd-integer $\bar{\nu}$, $\nu_n \to 1$, the width of the first single step together with the second plateau width of each double step shrinks to zero, so that only steps with step height 2Ω and plateau width Ω occur. (For $\bar{\nu} = 1$, i.e., $n = 0$, no double step exists and the single step merges with the breakdown regime.) In the even-$\bar{\nu}$ limit, $\nu_n \to 2$, the width of the first plateau of each double step shrinks to zero. Thus, the first step of width Ω and height Ω is followed by n steps of the same plateau width but double step height.

Summarizing the estimates of this Sec. 3.2.2, note that the Eqs. (3.15) – (3.23) define a set of straight lines in the v_0-Ω plane, which separate areas in each of which the variance $\mathrm{Var}[v](v_0)$ equals an integer multiple of Ω at $T = 0$. This is schematically shown in Fig. 3.7. Position and height of the steps of the $\mathrm{Var}[v](v_0)$ curve for a given value of $\bar{\nu}$ can immediately be read off from this figure along the vertical line at $\Omega = 2/\bar{\nu}$. For a comparison a finite temperature calculation is shown in Fig. 3.8, note that the vertical axis is not scaled with $\epsilon(q)$ and the magnetic field axis is linear in $\bar{\nu}(\propto 1/B)$.

3.2.3 Sweeping the magnetic field

We now consider the screening of an external cosine potential $V_{\mathrm{ext}}(x) = V_0 \cos qx$ of fixed amplitude V_0 as function of the magnetic field B, keeping the average electron density at the fixed value of the positive background charge density. Then, with increasing B the average

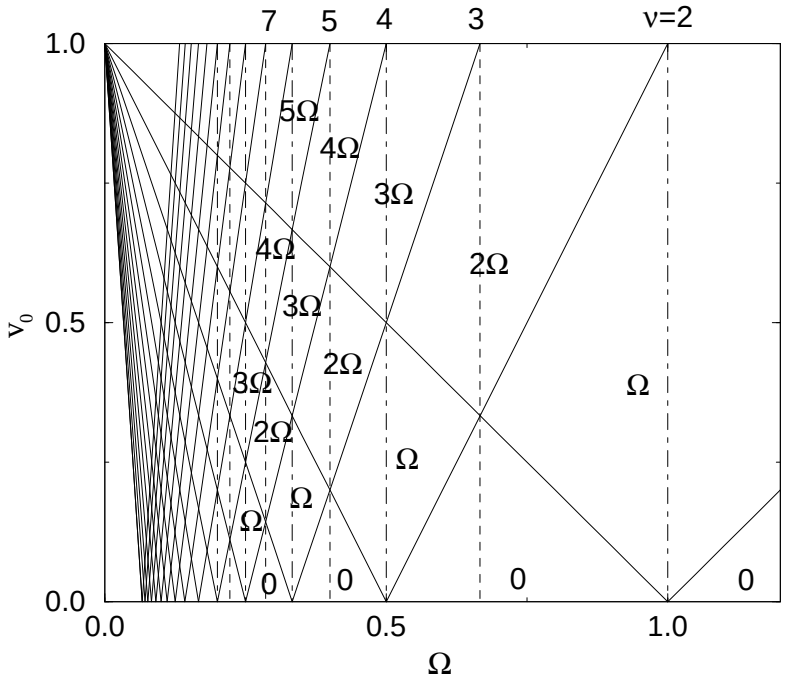

Figure 3.7: Variance of screened potential, $V(x)$, as a function of magnetic field and amplitude of the external potential, at zero temperature. The solid lines indicate $v_0 = k\Omega - 1$ and $v_0 = 1 - k\Omega$ for $v_0 = V_0/[E_F\epsilon(q)]$, $\Omega = \hbar\omega_c/E_F$, and $k = 1, 2, \ldots, 15$. Even (odd) integer values of the average filling factor are indicated by dash-dotted (dashed) vertical lines. Within each area defined by the solid lines the value of $\mathrm{Var}[V]/E_F$ equals an integer multiple of Ω. This value increases by Ω, if a solid line is crossed in upward direction. The region $v_0 > 1$ corresponds to the poor screening regime of parallel, disconnected quasi 1D electron systems.

filling factor $\bar{\nu} = 2E_F/\hbar\omega_c$ decreases. For the unmodulated 2DES ($V_0 = 0$), this leads to the well known saw-tooth behavior of the chemical potential, which at low temperatures is pinned to the LLs, i.e. follows half-integer multiples of the cyclotron energy,

$$\mu^* = \hbar\omega_c(n + 1/2) \quad \text{if} \quad 1/(n+1) < \Omega < 1/n\,. \tag{3.24}$$

In the modulated 2DES ($V_0 > 0$), pinning of LLs to the electrochemical potential causes the total variance of the screened potential to be an integer multiple of the cyclotron energy. Thus, for the variance $\mathrm{Var}[V]$ as function of B one expects a similar saw-tooth behavior as for the μ^*-vs-B curve. Numerical results for several values of V_0 are shown in Fig. 3.9. The uppermost curve for the largest modulation amplitude looks indeed similar to a μ^*-vs-B curve. However,

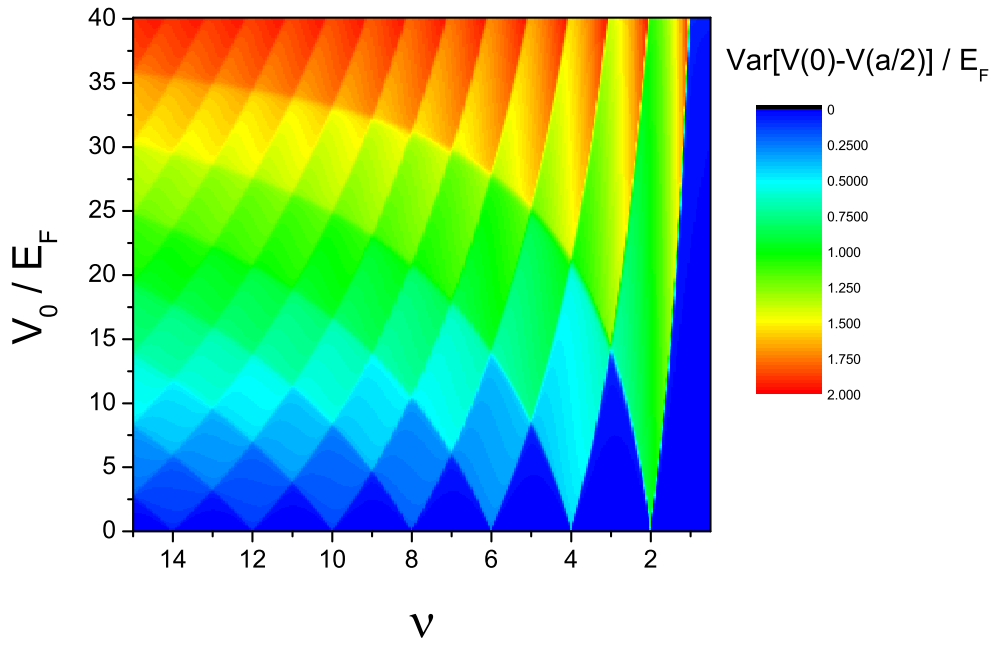

Figure 3.8: Variance of screened potential, $V(x)$ as a function of filling factor and amplitude of the external potential, at $k_BT/E_F = 0.01$. The color scale indicates the heights of the plateaus. The plateau height is finite for even integer and is zero for odd integer filling factors at the limit $V_0/E_F \to 0$.

whereas the latter with decreasing B always jumps to the next higher LL, the $\mathrm{Var}[V]$-vs-B curves can also jump back to the next lower LL, as is more clearly seen for the curves with smaller modulation amplitudes. This seemingly irregular behavior of the $\mathrm{Var}[V](\Omega)$ curves in Fig. 3.9 can easily be understood from Fig. 3.7, where now horizontal lines have to be followed. For fixed $v_0^0 = V_0/[E_F\epsilon(q)]$ and decreasing Ω, the variance $\mathrm{Var}[V]/E_F$ increases by Ω, if the horizontal line $v_0 = v_0^0$ intersects one of the straight lines $v_0 = k\Omega - 1$, and decreases by Ω, if it intersects one of the straight lines $v_0 = 1 - k\Omega$. For large V_0 ($v_0 > 0.6$), the variance jumps with decreasing B monotonically to higher multiples of the cyclotron energy, until B becomes so small, that $\Omega = 1 - v_0^0$. Then, for smaller B also jumps back to lower multiples occur. For small modulation amplitude ($v_0^0 \lesssim 0.1$) one has perfect screening if the average filling factor is not too close to an even integer. Near such values linear screening breaks down and $\mathrm{Var}[V]/E_F$ approaches Ω, provided $2V_0 > \hbar\omega_c$ (otherwise $\mathrm{Var}[V] = 2V_0$). For sufficiently small B, of course the variance will equal higher multiples of the cyclotron energy, so that the correct linear screening limit is obtained in the limit of zero magnetic field.

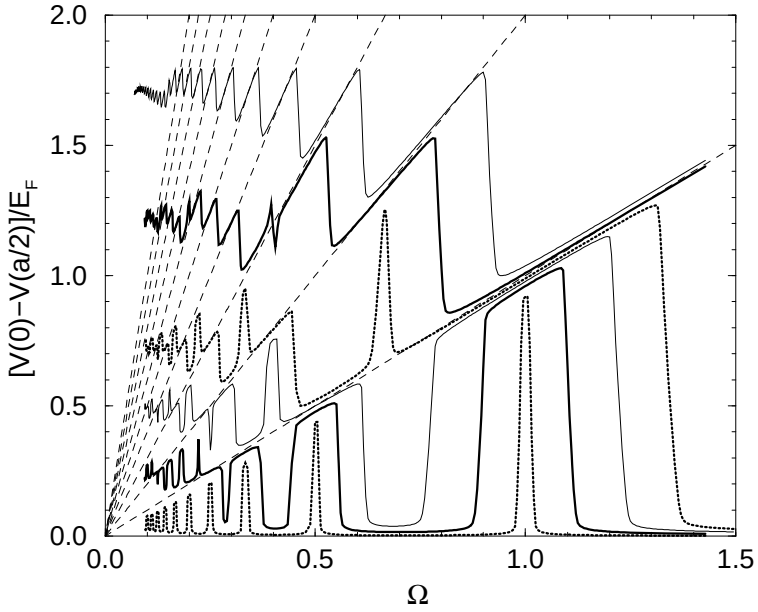

Figure 3.9: Variance of the screened potential versus $\Omega_c = \hbar\omega_c/E_F$ for $V_0/E_F = 1, 5, 10, 15, 25, 35$ (from bottom to top). The straight dashed lines indicate integer multiples of the cyclotron energy. ($k_BT/E_F = 0.01$, $\epsilon(q) = 41$).

Thus, if one adds the smoothening effect of finite temperature, one can understand all properties of the apparently irregular $\mathrm{Var}[V](\Omega)$ traces in Fig. 3.9 in terms of the peculiar but regular v_0-vs-Ω pattern sketched in Fig. 3.7.

3.3 Hall bar geometry

3.3.1 Boundary conditions and kernels

We now consider a 2DES with lateral confinement in the x direction and translation invariance in the y direction, i.e., an idealized Hall bar geometry. To study boundary effects on the screening properties, we will apply an additional periodic external modulation potential in x direction. We will consider two different sets of boundary conditions, which lead to slightly different confinement potentials.

In-plane gates

Following Refs. [10–13] we first assume that all charges reside in the plane $z = 0$, and that the half-planes $z = 0$, $x < -d$ and $z = 0$, $x > d$ are kept at constant electrostatic potential, $V(x, y, z = 0) = 0$ for $|x| > d$ (see App. A.2) [11, 13]. Then the electrostatics can be solved using the theory of complex functions, and the kernel in Eq. (2.2), with $-x_l = x_r = d$, is obtained as [13]

$$K_{\parallel}(x,t) = \ln \left| \frac{\sqrt{(d^2 - x^2)(d^2 - t^2)} + d^2 - tx}{(x - t)d} \right| . \tag{3.25}$$

Positive background charges of the 2D charge density en_0 between the in-plane gates will produce the confinement potential (written as potential energy of an electron)

$$V_{\rm bg}(x) = -E_0 \sqrt{1 - (x/d)^2}\,, \quad E_0 = 2\pi e^2 n_0 d/\bar{\kappa}\,, \tag{3.26}$$

which can be calculated from Eq. (2.2) using the kernel (A.19) and replacing $n_{\rm el}(x')$ by $-n_0$.

Perpendicular gates

Another simple set of boundary conditions is obtained assuming the 2DES to be laterally confined by two equipotential planes located at $x = \pm d$ parallel to the y-z plane, $V(x = \pm d, y, z) = 0$. This is a reasonable model for a free standing mesa-etched Hall bar with free or metalized surfaces at $x = \pm d$, which accommodate a large number of (partially occupied) surface states. The electrostatics with these boundary conditions is well known and is presented in App. A following [60]. In our notation it is expressed by the kernel [see Eq. (A.9] with $z_0 = 0$ and $x_0 = t$]

$$K_{\perp}(x,t) = -\ln \left(\frac{\cos^2 \frac{\pi}{4d}(x + t) + \gamma^2}{\sin^2 \frac{\pi}{4d}(x - t) + \gamma^2} \right) \tag{3.27}$$

for $\gamma \to 0$. Inserting this with $\gamma = \sinh(\pi z/4d)$ into Eq. (2.2), where $-x_l = x_r = d$, yields the electrostatic potential $V_H(x, y, z)$ due to the 2DES at a position separated by the distance $|z|$ from the plane of the 2DES. Correspondingly, one can use this to calculate the confinement potential produced in the plane of the 2DES by a plane, positive background charge at a distance z from the 2DES. Typical confinement potentials are shown in Fig. 3.10. For $\gamma = 0$ the potential minimum is $V_{\rm bg}(0, y, 0)/E_0 = -8G/\pi^2 = -0.74246$, with Catalan's constant [63] $G = 0.915965594$.

The positive background charge density and the sample width define the characteristic energy E_0, Eq. (3.26). Measuring energies in units of E_0, lengths in units of d, and density of states in units of D_0, from Eq. (2.8) one obtains the dimensionless electron density

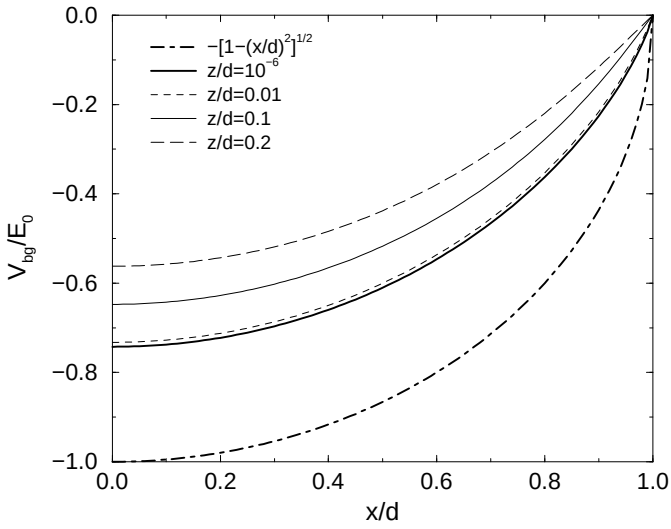

Figure 3.10: Confinement potential $V_{\rm bg}(x, y, z = 0)/E_0$ due to a homogeneous plane of charge density en_0 at distance z. The dash-dotted line is obtained from model (A.19) with $z = 0$, the other lines are for model (A.9).

$\widetilde{n}(x/d) = n_{\rm el}(x)/E_0 D_0$, so that Eq. (2.2) assumes a dimensionless form with the prefactor $1/\alpha_{\rm conf}$, where

$$\alpha_{\rm conf} = \pi a_B^*/2d \tag{3.28}$$

measures the relative strength of the Coulomb interaction, similar to α of Eq. (3.6). We will usually assume $\alpha_{\rm conf} = 0.01$, i.e., for GaAs, a sample width $2d \sim 3\,\mu$m, since this allows us to calculate density profiles with clearly visible incompressible strips on a mesh of relatively few (~ 500) points across the sample. For much larger d, one would need a much finer mesh, i.e., more ambitious numerics, and the incompressible strips would be hardly visible on that scale, although the physics would not change qualitatively.

Figure 3.11 shows some density and potential profiles obtained for the two sets of boundary conditions in the limit of zero temperature and magnetic field, where

$$n_{\rm el}(x)/n_0 = (\pi/\alpha_{\rm conf})\mu(x)\theta\big(\mu(x)\big)/E_0,$$

with $\mu(x) = \mu^* - V(x)$. Apparently the density profiles are very similar, if one assumes the same depletion length, the same sample width, and vanishing spacer between 2DES and background charges (i.e., $z = 0$) in both cases.

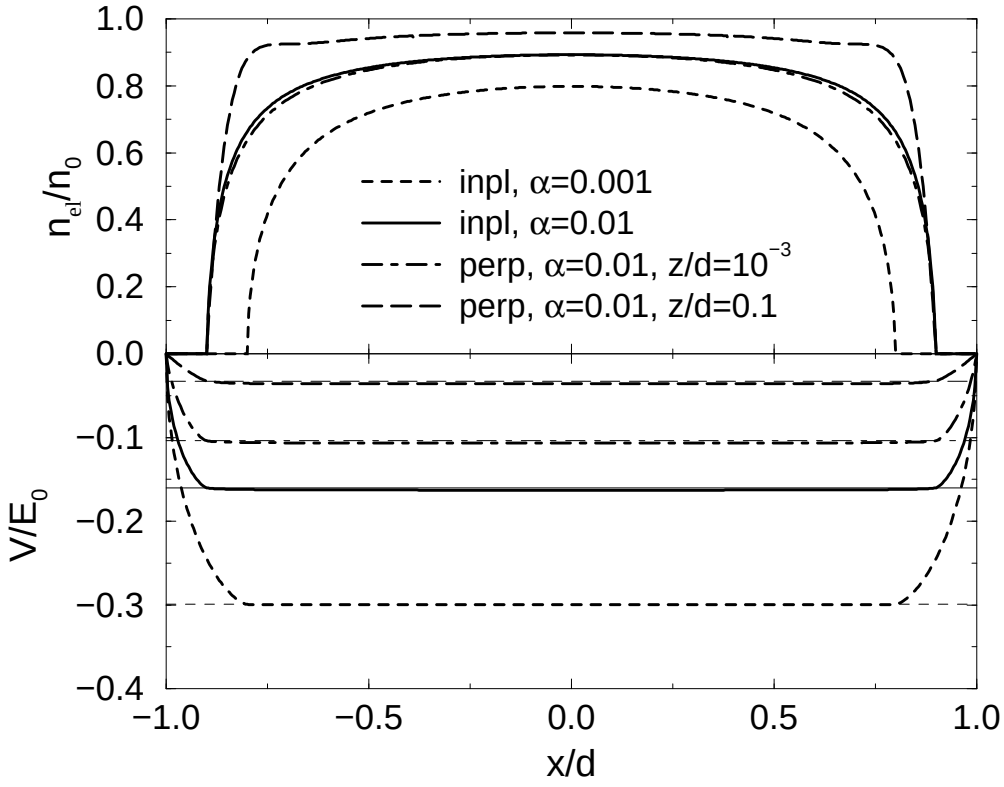

Figure 3.11: Some consistent density profiles (upper panel) and potentials (lower panel) calculated for the in-plane-gates model (A.19) and the perpendicular-gates model (A.9), respectively. The depletion length is chosen as $d/5$ for the short-dashed curves and as $d/10$ else. Thin horizontal lines indicate the corresponding electrochemical potentials. $\alpha = \pi a_B^*/2d$, $T = 0$, $B = 0$.

3.3.2 Unmodulated system in a magnetic field

In the ideal homogeneous 2DES at low temperatures, the chemical potential as a function of the magnetic field exhibits the well known saw-tooth behavior, Eq. (3.24). With decreasing B it follows a Landau energy $(n + 1/2)\hbar\omega_c$ until the filling factor $\nu = 2E_F/\hbar\omega_c$ reaches the value $2(n + 1)$, and then it jumps to the next higher LL. In the confined system, the self-consistently calculated "chemical potential" $\mu(0) = \mu^* - V(0)$ in the center, $x = 0$, shows the same behavior, as is seen in Fig. 3.12c, where $\mu(x = 0; B, T)$ in units of $\mu_0 \equiv \mu(x = 0; 0, 0)$ is plotted as function of $\Omega = \hbar\omega_c/\mu_0$.

However, in contrast to the chemical potential oscillations in a homogeneous 2DES, the corresponding oscillations in the confined system are realized by strong spatial variations of the

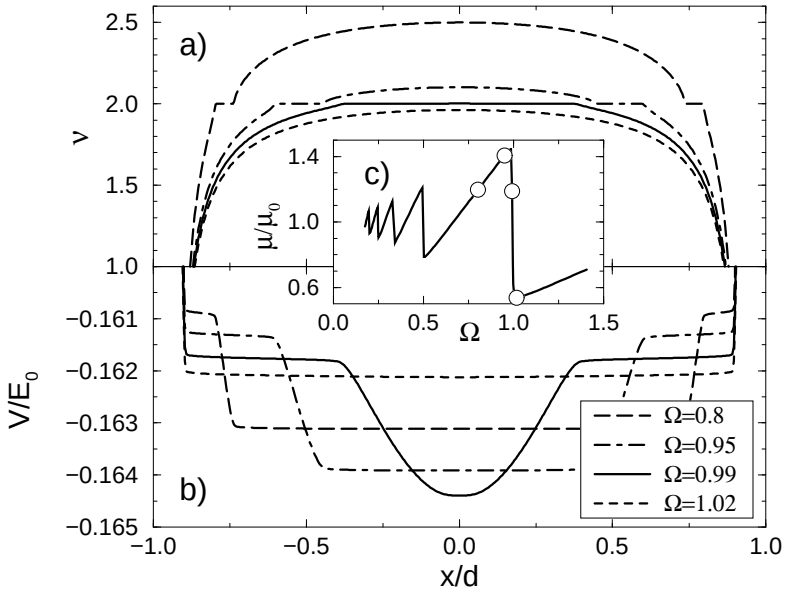

Figure 3.12: a) Filling factor $\nu(x)$ and b) potential $V(x)$ for the values of $\Omega = \hbar\omega_c/\mu_0$ given in the legend and indicated by open circles in c), which shows the "chemical potential" $\mu = \mu^* - V(0)$. Calculated with model (A.19) for parameter values $\pi a_B^*/2d = 0.01$, $\mu_0/E_0 = 0.00284$, $k_BT/E_0 = 2 \times 10^{-5}$.

electrostatic potential in the interior of the sample. This is demonstrated in Fig. 3.12b, which shows the self-consistent total potential in the interior of the sample for the four values of Ω indicated by open circles in Fig. 3.12c. Figure 3.12a shows the corresponding density profiles, normalized as local filling factor, $\nu(x) = 2\pi l^2 n_{\rm el}(x)$. For $\nu(x) \leq \nu(0) \approx 2/\Omega < 2$ the LL $n = 0$ is pinned to the electrochemical potential μ^* nearly everywhere in the 2DES. For $\nu(0) \gtrsim 2$ the LL $n = 1$ must be partially populated in the center of the sample. This forces the potential to develop a local minimum near the center, with a decrease of $V(0)$ by an amount $\sim \hbar\omega_c$, so that a compressible strip starts to develop in the center. With further increasing $\nu(0)$, this central compressible strip becomes broader and the adjacent incompressible strips, together with the related potential steps, move towards the sample edges. Similar drastic changes of the potential distribution are found near all jumps of the chemical potential. Thus, pinning and screening lead already to drastic effects in the confined 2DES even in the absence of any additional potential modulation.

3.3.3 Confined system with modulation

We now add a symmetric external modulation potential to the confinement potential and investigate how this affects the self-consistent potential. We take $V_{\rm ext}(x) = V_0 \cos(2.5\pi x/d)$ which is in accord with the general boundary conditions and exhibits just one full oscillation period in the interior of the sample, so that one can expect similar screening effects as in a homogeneous unbounded system, and possibly some effects of the nearby sample edges. The period of this modulation is $a = 2d/2.5$, so that the choice $\alpha_{\rm conf} = 0.01$ implies $\alpha = 1/40$ [see Eq. (3.6)] and the results can be compared immediately with the previous one for the unbounded 2DES. For this comparison it will be important whether the potential of the unmodulated system has a strong variation in the center region or not, i.e., whether the filling factor $\nu(0)$ in the center is slightly larger than an even integer or not.

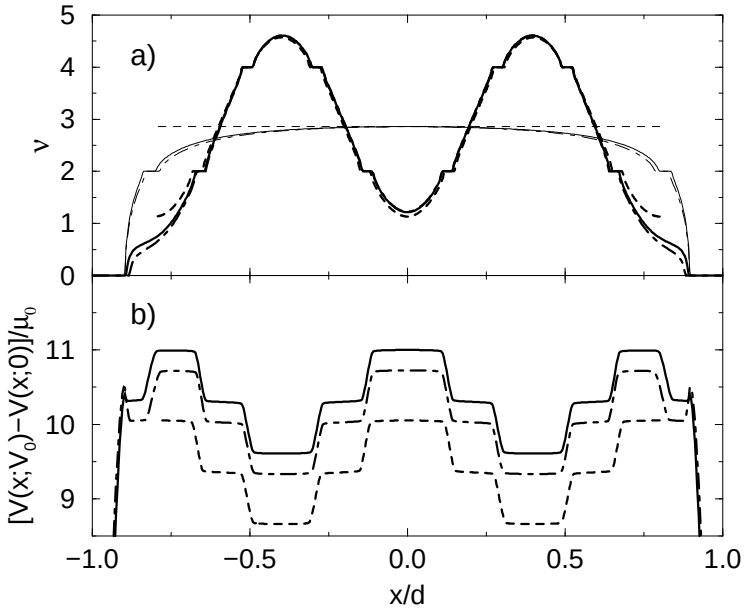

Figure 3.13: a) Filling factor $\nu(x)$ and b) screened potential $\Delta V(x; V_0)$ for the confinement models (A.19) (solid lines) and (A.9) (dash-dotted lines), and for the unconfined 2DES (dashed lines). Thin lines show $\nu(x)$ without modulation, with $\nu(0) = 2.8574$ for all models. The screened potential for the unbounded 2DES is shifted by a constant, and actually oscillates symmetrically around zero. ($\alpha_{\rm conf} = 0.01$, $\mu_0/E_0 = 0.002842$, $\hbar\omega_c/\mu_0 = 0.7$, $V_0/\mu_0 = 24.63$, $k_BT/\mu_0 = 0.007$)

Weak boundary effects on screening

To describe the screening of an external modulation potential, it seems natural to calculate the difference $\Delta V(x;V_0) = V(x;V_0) - V(x;0)$ of the self-consistent potentials with and without the modulation. If $V(x;0)$ is flat in the interior of the sample, one should expect that screening is very similar to that in an unconfined system and that $\Delta V(x;V_0)$ contains essentially the same information as $V(x;V_0)$, apart from an unimportant constant offset. This is indeed true if $\nu(0)$ is not closely above an even integer. As an example, we compare in Fig. 3.13 numerical results for the two confinement models and for the unconfined 2DES. The results for the density of the confined 2DES differ only slightly in the edge regions. In the interior, the filling factors $\nu(x)$ are practically the same and agree well with that of the unconfined 2DES with the same modulation potential. Also the screened potentials are equivalent and differ only by a constant offset, which results from the asymmetry of the density modulation with respect to the unmodulated electron density profile.

Strong confinement effect on screening

Things become more complicated, if already without additional external modulation the potential near the center of the Hall bar varies strongly, as happens for $\nu(0) = 2n + \nu_n$ with $0 < \nu_n \ll 1$. Then, for small modulation amplitude ($V_0 \ll \hbar\omega_c$), the self-consistent potential $V(x;V_0)$ follows $V(x;0)$, with a minimum at $x = 0$, and only the difference $\Delta V(x;V_0)$ reminds of an oscillatory potential with the phase of the external modulation, see solid lines in Fig. 3.14. For stronger modulation ($V_0 \lesssim \hbar\omega_c$), $V(x;V_0)$ develops a local maximum at $x = 0$ and the total variation of $V(x;V_0)$ in the center region $|x| \lesssim d/2$ is of the order of $V_0 < \hbar\omega_c$ see Fig. 3.14a. The variation of $\Delta V(x;V_0)$ is now, however, by an amount of $\hbar\omega_c$ larger. In this small-V_0 regime screening is rather poor and very nonlinear. As V_0 increases further, the variance $\mathrm{Var}[V](V_0) = V(0;V_0) - V(a/2;V_0)$ (note that $a/2 = 0.4\,d$) approaches the plateau value $\hbar\omega_c$, and then behaves as a function of V_0 just as for the unconfined 2DES. The variance of the "screened potential" $\Delta V(x;V_0)$, on the other hand, will be by about $\hbar\omega_c$ larger in the plateau region. To visualize this in Fig. 3.15a we show the variance of the screened potential as function of the amplitude V_0 of the applied modulation for several values of the magnetic field and a fixed low temperature, and in Fig. 3.15b the same dependence for a fixed value of the cyclotron energy and several temperatures. We define this variance as the difference between the maximum (at $x = 0$) and the minimum (near $x = 0.4d$) of the difference $V(x;V_0) - V(x;0)$ of the self-consistent potentials calculated with and without modulation, respectively.

For a fixed value of the magnetic field (i.e., of $\Omega \equiv \hbar\omega_c$), we obtain a stepwise increasing curve, as we expect. Here we introduce $\Omega_2 \equiv 0.2311 \times 10^{-2} E_0$ as a relevant normalization, which corresponds to the cyclotron energy of a bounded system with average filling factor 2. The corresponding (thick solid green) curve in Fig. 3.15a shows two broadened steps around

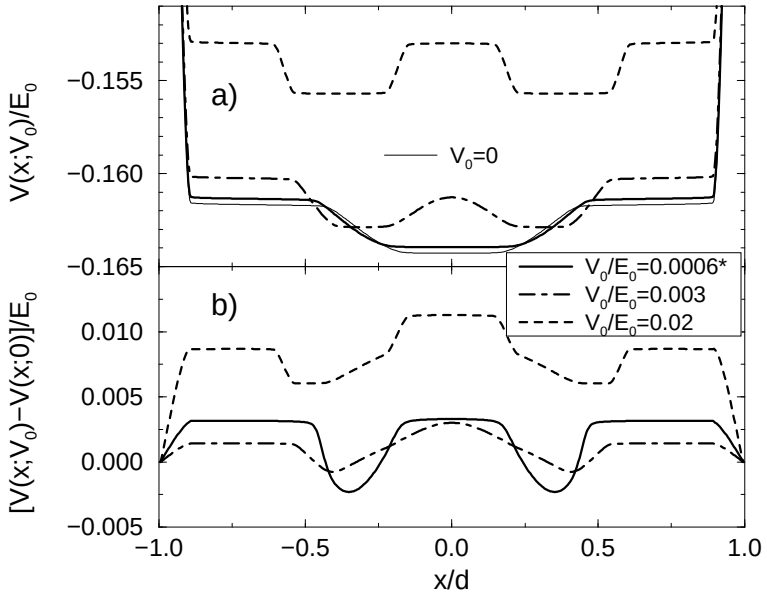

Figure 3.14: a) Self-consistent potential $V(x;V_0)$ and b) screened potential $\Delta V(x;V_0)$, for several V_0. For clarity, b) shows $10 \cdot \Delta V(x;V_0)$ for the weakest modulation $V_0 = 6 \cdot 10^{-4} E_0$. For $V_0 = 0$ [thin solid line in a)] $\nu(0) = 2.03$. ($\alpha_{\rm conf} = 0.01$, $\mu_0/E_0 = 0.002842$, $\hbar\omega_c/\mu_0 = 0.985$, $k_BT/\mu_0 = 0.01$)

$V_0/E_0 = 0.025$ and 0.075. We have already discussed the reason for the step at the lower V_0 value and for the plateaus below and above this step. With further increasing V_0 the filling factor near the density maxima becomes larger than 4 (see Fig. 3.13) while the density in the center is still finite. Then new incompressible strips with local filling $\nu(x) = 4$ develop on both sides of the density maxima, which corresponds to a decrease of the self-consistent potential by the amount Ω to new local minima near $x = \pm 0.4d$. In Fig. 3.15a this leads to the plateau of height 2Ω. As V_0 increases further, the electron density $n_{el}(0)$ in the center vanishes and no further redistribution of electrons from the center region to the region of maximum density is possible. Then the high screening ability of the electron system breaks down and the variance increases with further increasing V_0 much more rapidly (see behavior at $V_0/E_0 > 0.125$). This breakdown happens for $\Omega = \Omega_2$ when the filling factor at the density maxima is somewhat larger than 4 (~ 5).

We can now understand all the curves in Fig. 3.15a. Since, apart from the fine structure near incompressible strips, the global density profile depends only weakly on the magnetic field, for the lowest curve (long-dashed, $\Omega = 3\Omega_2$) typical filling factors $\nu(x)$ are by a factor 3 smaller than for the case $\Omega = \Omega_2$ we have just discussed. Therefore the breakdown situation is reached

when the filling factor near the density maxima is of the order $5/3 < 2$. Thus the breakdown sets in before an incompressible strip and thus a plateau of height $3\Omega_2$ of the variance can develop. For $\Omega = 2\Omega_2$ [short-dashed line, label (i)] the local filling factors $\nu(x)$ are typically about half as large as in the case $\Omega = \Omega_2$. Thus, $\nu(x) < 2$ for weak modulation, and incompressible strips with $\nu(x) = 2$ can occur only near the density maxima for sufficiently strong modulation, and a single plateau of height $2\Omega_2$ occurs below the breakdown regime. A similar situation is met for $\Omega = 1.5\Omega_2$ [label (ii)], but since now $\nu(x)$ is about $2/3$ times that for $\Omega = \Omega_2$, the threshold of the plateau is reached at a considerably weaker modulation. Finally, for $\Omega = 0.75\Omega_2$ we obtain three plateaus in the pre-breakdown regime, corresponding to the successive development of incompressible strips with local filling factor 4 (maxima), 2 (minimum), and 6 (maxima).

We should mention that the behavior of the variance curves is not always that regular. For special values of Ω it may happen that incompressible strips near the center and near the density maxima occur at the same modulation strength. Then steps of height 2Ω occur. We met such a situation for $\Omega = 0.5\Omega_2$ (not shown in Fig. 3.15a), which yields nearly the same trace as $\Omega = \Omega_2$.

For the smaller Ω values, the variance curves oscillate around the dash-dotted line in Fig. 3.15a, which represents the corresponding result $2V_0/[E_0\varepsilon(q)]$ of linear Thomas-Fermi screening [1] for zero T and B, with $\varepsilon(q) = 1 + 1/(a_0 q) = 41$ for $q = 2.5\pi/d$. This linear screening approximation breaks down when the amplitude of the screened potential (i.e. half the variance) becomes equal to the Fermi energy of the unmodulated system [62], which can be estimated from Fig. 3.13 as $\sim 3 \times 10^{-3} E_0$, corresponding to $V_0 \sim 0.12 E_0$. Finally we should mention that the small-variance regime in Fig. 3.15a also corresponds to linear screening, but now with $\varepsilon(q) = 1 + (D_T/D_0)/(a_0 q)$, where D_T is the thermodynamic DOS in a LL, which can be estimated by $D_T/D_0 \sim \hbar\omega_c/(4k_BT)$ [1]. Thus, the slope of the variance curves is by a factor $\sim 4k_BT/\Omega \ll 1$ smaller than that of the dash-dotted line.

As shown in Fig. 3.15b, with increasing temperature the plateaus of the variance-versus-V_0 curves get a finite slope and the steps are smeared out. This is an immediate consequence of the temperature dependence of the incompressible strips. At the highest shown temperature screening becomes again linear and independent of B, but now the temperature is so high that the thermodynamic DOS is noticeably smaller than D_0. A clear indication of steps is seen only for $k_BT/\hbar\omega_c \lesssim 1/25$ [12]. To summarize, if one neglects the relatively narrow V_0 interval between the plateaus, one finds that the variance of the self-consistent potential $V(x; V_0)$ as a function of V_0 shows the same behavior as for the unconfined 2DES. For most magnetic field values, the variance of the "screened potential" $\Delta V(x; V_0)$ also shows the same characteristics. Only if the filling factor $\nu(0)$ in the center of the unmodulated confined 2DES is slightly larger than an even integer, the spatial variation of the self-consistent potential $V(x; 0)$ of the unmodulated system causes the variance of $\Delta V(x; V_0)$ to be about $\hbar\omega_c$ larger than the variance of $V(x; V_0)$. If the

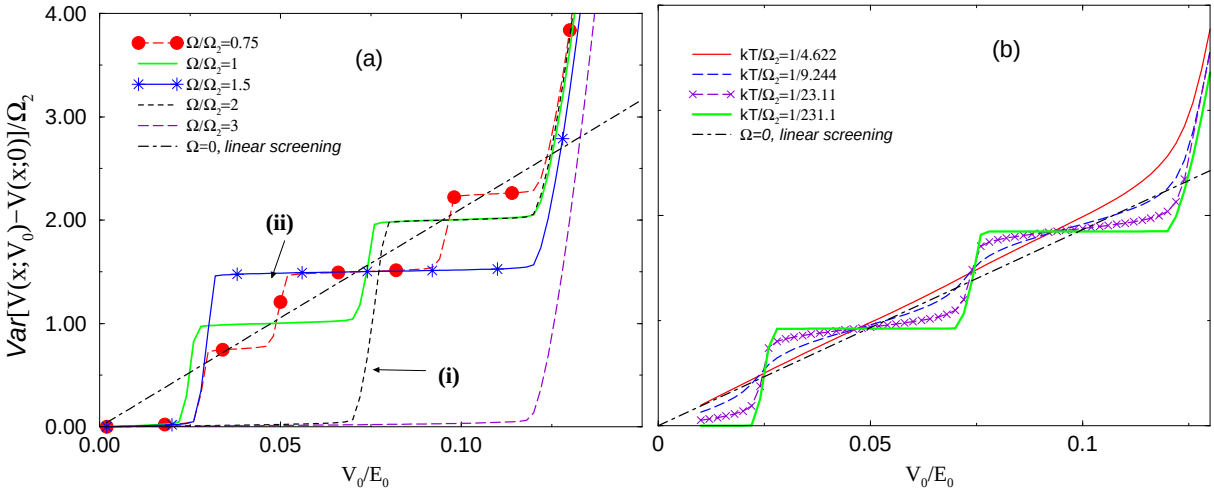

Figure 3.15: (a) Variance of screened potential versus amplitude V_0 of the external potential for various magnetic field values ($\pi a_0/d = 0.01$, $k_BT/E_0 = 2 \cdot 10^{-5}$). The dash-dotted line indicates linear screening for zero B and T, see text. (b) Temperature dependence of the variance for $\Omega/\Omega_2 = 1$

.

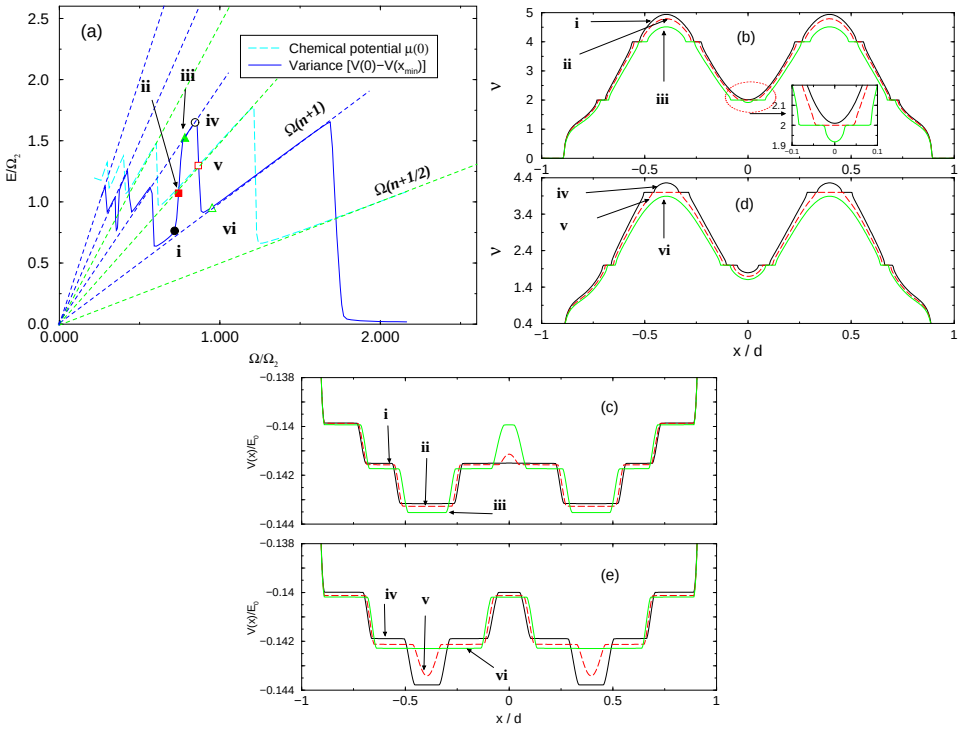

Figure 3.16: (a) Variance of self-consistent potential for modulation amplitude $V_0 = 0.05E_0$ versus Ω; (b),(d) density and (c),(e) potential profiles for selected Ω values marked in (a). $k_BT/E_0 = 2 \cdot 10^{-5}$, $\pi a_0/d = 0.01$.

variance of $\Delta V(x; V_0)$ at fixed V_0 is plotted as a function of $\Omega = \hbar\omega_c/\mu_0$, sawtooth-like traces as in Fig. 3.9 are obtained, however with additional spikes of height Ω at $\Omega \lesssim 1/k$ for integer k. In order to have a better understanding of the strong confinement effect on screening, we investigate the in-plane model in some detail. We define now the variance of the self-consistent potential as $var = V(0) - V(x_{min})$, where $\pm x_{min} \sim \pm 0.4d$ are the positions of the minima of $V(x)$ in the presence of modulation, and $V(0)$ is the local maximum at the center. In Fig. 3.16a we plot var versus Ω, together with $\mu(0)$. As expected, var follows widely integer multiples of Ω, whereas $\mu(0)$ follows half-integer ones. But, whereas $\mu(0)$ jumps with increasing Ω always to the next lower LL, var can also jump to a higher multiple of Ω. To understand this, we show in Fig. 3.16b-3.16e density and potential profiles for the six Ω values marked in Fig. 3.16a.

In case (i) (solid lines in Fig. 3.16b and 3.16c) the center region is compressible with $\nu(0)$ slightly larger than 2 and with the $n = 1$ LL pinned to μ^*, whereas the compressible regions near the density maxima have $\nu(x) > 4$ ($\nu(x_{min}) \approx 5$) and the $n = 2$ LL is pinned to μ^*. This yields $var \approx \Omega$. For slightly larger Ω [(ii), dashed lines in 3.16b and 3.16c], an incompressible strip with filling factor 2 and a local maximum of $V(x)$ at $x = 0$ develops in the center, while the situation near the density maxima is unchanged. This leads to $\Omega < var < 2\Omega$. At still slightly larger Ω [(iii), dotted lines in 3.16b and 3.16c], the region near the density maxima is still qualitatively unchanged, whereas in the center a compressible region with $\nu(x) < 2$ develops, where the $n = 0$ LL is pinned to μ^*, leading to $var \approx 2\Omega$. As Ω increases further [(iv) – (vi)], the situation in the center remains qualitatively the same, whereas the filling factor at the density maxima changes from $\nu(x_{min}) > 4$ to $\nu(x_{min}) < 4$, so that the incompressible strips with $\nu(x) = 4$ merge [(v), dashed lines in 3.16d and 3.16e] and finally disappear, accompanied by the disappearance of the potential step across these strips. Thus, we have again $var \approx \Omega$, until for much larger Ω the maximum filling factor becomes smaller than 2 and var goes back to the very small value corresponding to linear screening in the lowest Landau level.

3.4 Summary

We have investigated the screening of a harmonic external potential by an unconfined two-dimensional electron gas as well as by confined 2DESs in a simplified Hall geometry, in strong perpendicular magnetic fields and at low temperatures. Our numerical results within the self-consistent Thomas-Fermi-Poisson approach show that screening is very nonlinear and dominated by the phenomenon of pinning of Landau levels to the electrochemical potential, which leads to compressible regions with position-dependent electron density, where this pinning takes place, and to incompressible regions of constant density and position-dependent electrostatic potential in between. At fixed magnetic field, the total variation ("variance" $\mathrm{Var}[V]$) of the self-consistently calculated potential energy increases with increasing modulation amplitude V_0 in a

step-like fashion, exhibiting plateaus, where the value of $\mathrm{Var}[V]$ is close to an integer multiple of the cyclotron energy and shows a weak linear increase with V_0, with a slope proportional to the temperature. The corresponding modulation of the electron density is, in contrast to the potential, not strongly affected by the magnetic field B. The occurrence of incompressible strips leads to local modifications, but the overall density profile is roughly the same as for $B = 0$, as has already been emphasized by Chklovskii *et al.* [10]. Exploiting this observation together with the pinning phenomenon and the relations between density modulation and external and screened potential valid in the linear screening regime, we were able to derive simple analytical expressions for step heights and plateau widths of the $\mathrm{Var}[V]$-vs-V_0 curves for arbitrary B and $T = 0$. This simple analytical description of nonlinear screening in an unconfined 2DES is summarized in Fig. 3.7, and allows also an easy understanding of the complicated traces obtained while plotting $\mathrm{Var}[V]$ as a function of B at fixed V_0 (see Fig. 3.9).

Finally we have investigated the corresponding screening properties of a confined 2DES in a simplified Hall geometry, for two different types of boundary conditions, which has led to different confinement potentials, but nearly identical density profiles, apart from slight deviations in the edge regions. Considering the effect of an external modulation potential $V_{\mathrm{ext}}(x) = V_0 \cos(2.5\pi x/a)$ in the interior of the sample (more than about $a/2$ from the edges), we find essentially the same properties as for the unbounded 2DES. Care must however be taken if in the center of the unmodulated system a new Landau level starts to be occupied, since then the self-consistent potential varies strongly in the center region. This is an interesting confinement effect, but it can be easily eliminated from the discussion of screening if the modulation amplitude V_0 is large enough.

Chapter 4

Quantized Hall Plateaus resulting from screening

4.1 Introduction

The purpose of the present chapter is to propose and evaluate a quasi-local transport model that allows to calculate, first, the potential and current distribution in a two-dimensional electron system (2DES) under the conditions of the QHE, and, second, the longitudinal and the Hall resistance, $R_l(B)$ and $R_H(B)$, in the plateau regimes of the QHE and in between. Whereas the resistance values between the QH plateaus will depend on details of the used conductivity model, the exactly quantized plateau values result from the existence of sufficiently wide "incompressible strips" along which the local conductivity vanishes, since occupied and unoccupied states are separated by an energy gap (Landau quantization). Localization assumptions, [29] which played an important role in early approaches to the QHE, are not included in our model. Our model is motivated by a recent experimental investigation of the Hall-potential in a narrow Hall bar, [21] and a critical reexamination of a subsequent model calculation. [27]

Here we aim to improve on the model of GG [27] so that, first, qualitative agreement between the calculated and the measured potential distribution is achieved for all filling factor regimes, and, second, reasonable results for $R_l(B)$ and $R_H(B)$ are obtained. Following the lines suggested by GG [27], we investigate in Sec. 4.2 the conditions for the existence of incompressible strips, using a Hartree approximation. In Sec. 4.3 we reexamine and weaken the strictly local conductivity model, and show that a simple spatial-averaging procedure of the local conductivities can simulate corrections expected from a Hartree calculation for the equilibrium state and from a non-local transport calculation. Transport results based on the self-consistent Born approximation will be presented and discussed in Sec. 4.4. The main results of this chapter has been presented recently at an international meeting [64] and in a regular journal [65] In the present work we will restrict our consideration on the linear response regime, so that heating

effects [66,67], which might destroy incompressible strips in the presence of high currents, [27] can be neglected.

4.2 Existence of incompressible strips

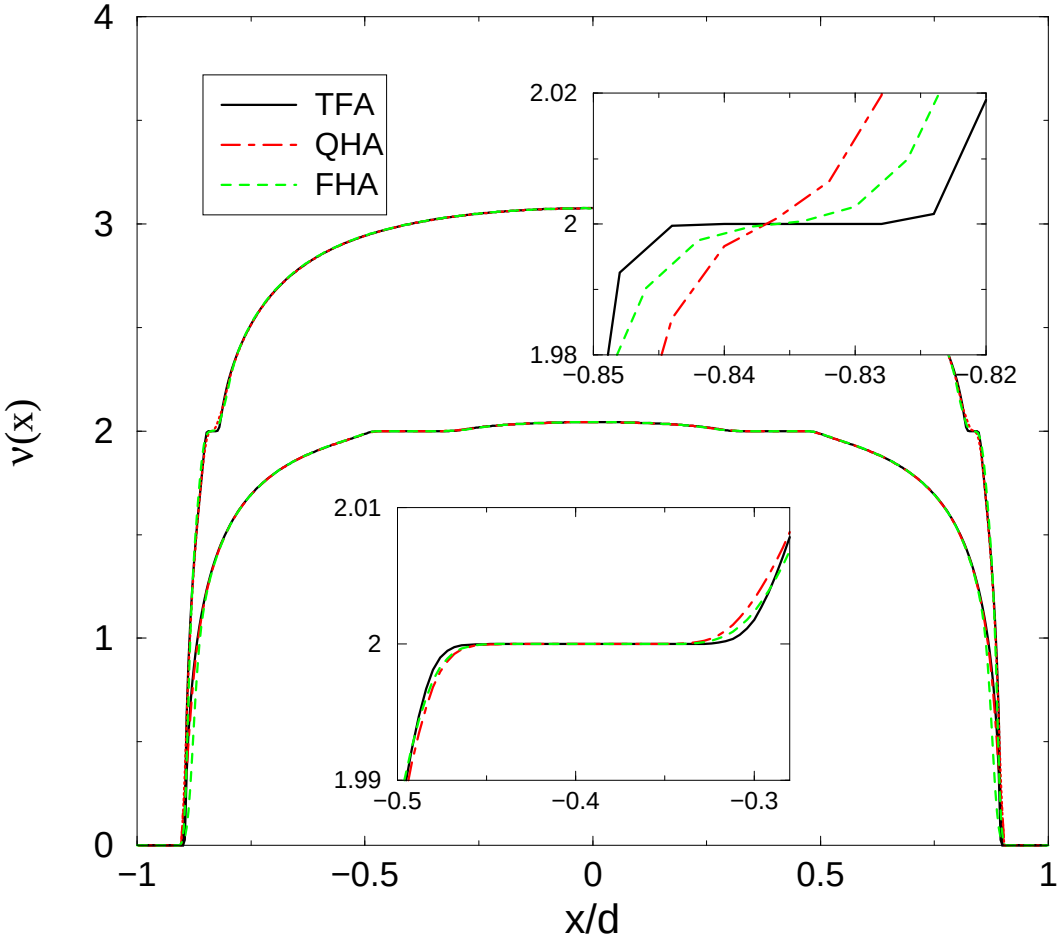

Figure 4.1: Electron density profiles for two values of the magnetic field ($\hbar\omega_c/E_F^0 = 0.94$ and 0.65) and different approximations: Thomas-Fermi (solid lines), Hartree (dashed), and quasi-Hartree (dash-dotted). The insets show the enlarged plateau regions for both cases. $\alpha = 0.01$, $k_BT/E_F^0 = 0.0124$. Kinks in the upper inset indicate mesh points.

The results discussed in this chapter are calculated considering the in-plane Hall bar geometry presented in the appendix A.2. We assume all the charges reside in the $z = 0$ plane, with a symmetric depletion. The solid lines of Fig. 4.1 show results for $d = 1.5\,\mu$m and $n_0 = 4 \cdot 10^{11}\,\mathrm{cm}^{-2}$ (which implies $E_{bg}^0 = 4.38\,\mathrm{eV}$) obtained for 501 equidistant mesh points,

$-d = x_0 < x_n < x_N = d$ ($N = 500$) within the TFPA. The density profile was fixed by choosing $b/d = 0.9$, which yields $\bar{n}_{\rm el} = 2.9 \cdot 10^{11}\,{\rm cm}^{-2}$ and $n_{\rm el}(0; B=0, T=0) = 3.58 \cdot 10^{11}\,{\rm cm}^{-2}$, and thus, with $D_0 = 2.8 \cdot 10^{10}\,{\rm meV}^{-1}{\rm cm}^{-2}$ for GaAs, $E_F = 10.37\,{\rm meV}$ and $E_F^0 = 12.75\,{\rm meV}$. We prefer to use E_F^0 (rather than E_{bg}^0) as an reference energy, since it has the same order of magnitude as the cyclotron energies of interest. For finite B we define an effective center filling factor $\nu_0 = 2\pi l^2 n_{\rm el}(x=0; B=0, T=0) = 2E_F^0/\hbar\omega_c$.

The result obtained for the TFPA (solid lines in Fig. 4.1) shows the expected well developed incompressible strips with constant electron density at local filling factor $\nu(x) = 2$. For the larger B value one obtains wide density plateaus at $0.32 \le |x|/d \le 0.46$, in each of which one finds at 36 x_n values, with high accuracy, $\nu(x_n) = 2$. For the lower B value the incompressible strips are much narrower, however one obtains the high precision values $\nu(x_n) = 2$ still at five neighboring x_n values. Typical results of the TFPA are summarized in Fig. 4.2, which

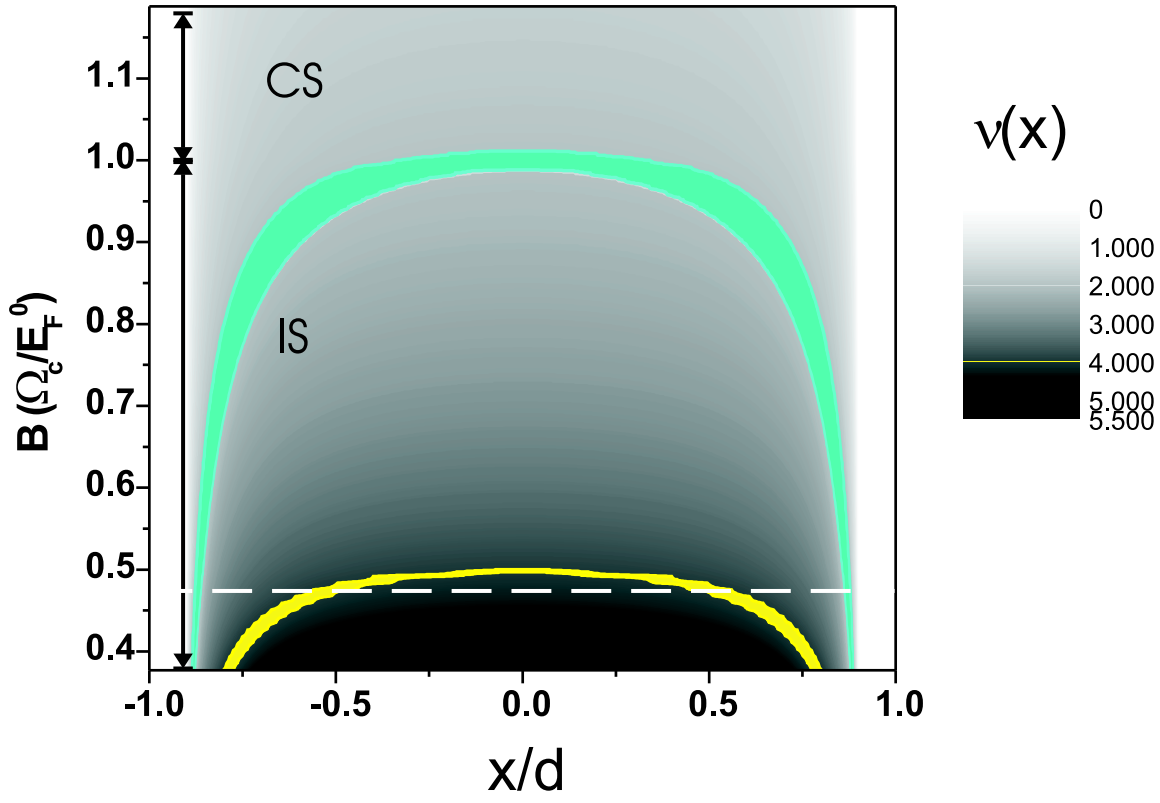

Figure 4.2: Gray scale plot of filling factor versus position x and magnetic field B, calculated within the TFPA. The regions of incompressible strips with $\nu(x) = 2$ and $\nu(x) = 4$ are indicated. For sufficiently large B ($\Omega_c \equiv \hbar\omega_c > E_F^0$) the system is compressible (indicated by "CS"), while for the lower B values included in the figure it always contains incompressible strips ("IS"). The dashed horizontal line refers to Fig. 4.6 below; $\alpha = 0.01$, $k_B T/E_F^0 = 0.0124$.

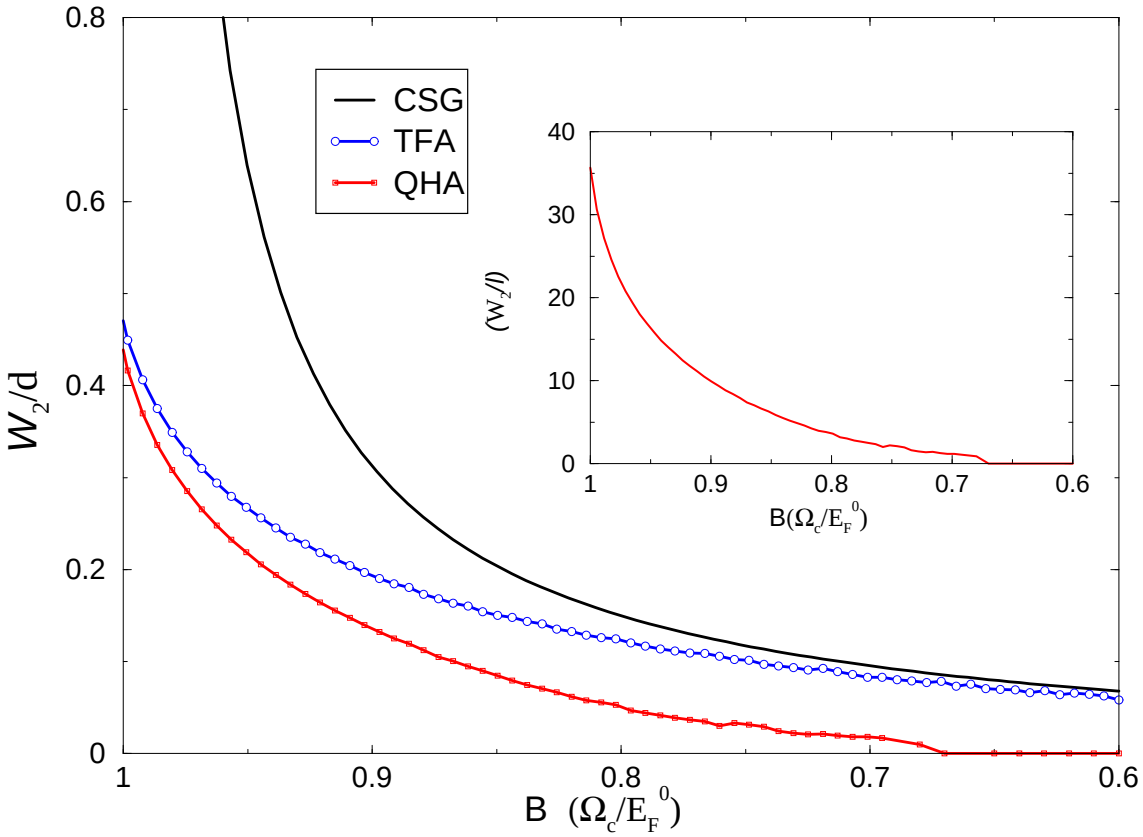

Figure 4.3: Magnetic-field dependence of the width of the $\nu = 2$ incompressible strips, for three different approximations: the analytical result of Ref. [10] (CSG), the TFPA (TFA), and the quasi-Hartree approximation (QHA). Note the inverted B scale. Inset: ratio of the incompressible strip width to the magnetic length in QHA.

shows, as a gray scale plot, the filling factor profile for varying magnetic field, with horizontal lines corresponding to a fixed B value. At sufficiently large B field, the local filling factor $\nu(x)$ is everywhere in the Hall bar less than 2, and the 2DES is completely compressible. At somewhat lower B ($\hbar\omega_c/E_F^0 \approx 1$) the center of the sample becomes incompressible with local filling factor $\nu(x) = 2$, while $\nu(x)$ gradually decreases outside the incompressible center and falls off to zero in the depletion regions at the sample edges. With further decreasing B, the filling factor in the center increases and incompressible strips with $\nu(x) = 2$ move towards the sample edges and become narrower. At sufficiently low B values, incompressible strips with local filling factor $\nu(x) = 4$ occur, first in the center, and then move towards the edges. They then coexist with incompressible strips of $\nu(x) = 2$, which exist near the edges and are narrow, but, within the TFPA, still have a finite width. For low enough temperature, this type of behavior continues at still lower values of B, where further incompressible strips with successively higher

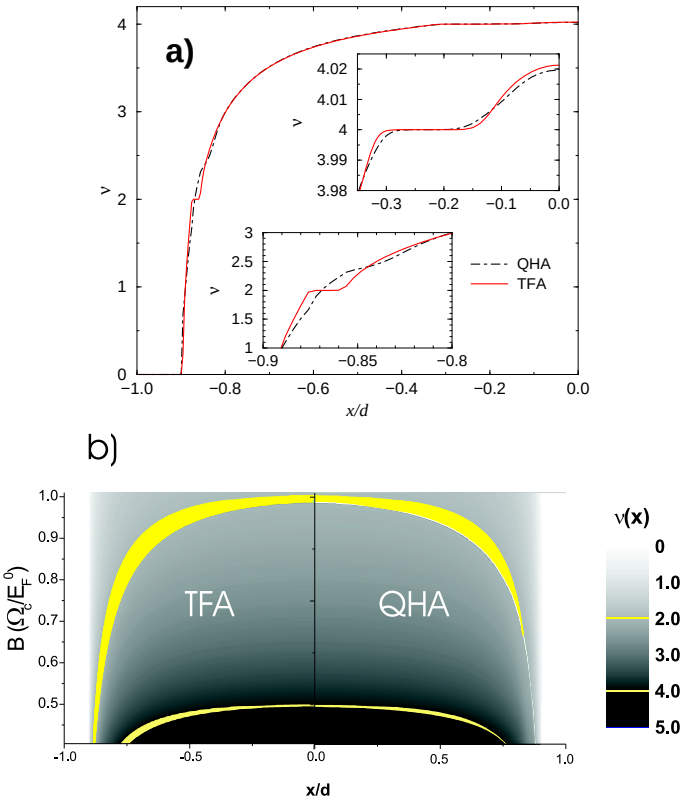

Figure 4.4: (a) Calculated density profiles for the left half of a symmetric Hall bar. While the TFA yields incompressible strips with $\nu(x) = 2$ and $\nu(x) = 4$, only those with $\nu(x) = 4$ survive in the QHA. (b) Local filling factors (gray scale plot) versus position x and cyclotron energy. ISs (light) exist in the TFA for all B with $\Omega_c/E_F^0 < 1$, in the QHA, however, only for $1.0 > \Omega_c/E_F^0 > 0.65$ and $0.5 > \Omega_c/E_F^0 > 0.4$. $d = 3.1\mu$m, average electron density $3 \cdot 10^{11}$cm^{-2}, temperature $k_BT/E_F^0 = 0.02$, $E_F^0 = n_{\rm el}^0(0)\pi\hbar^2/m$, where $n_{\rm el}^0(0) = n_{\rm el}(0)$ at $T = 0$, $B = 0$.

filling factors evolve from the center and move towards the edges, coexisting with the edge-near incompressible strips of lower local filling factors.

4.2.1 "Quasi-Hartree" Approximation

The dashed lines in Fig. 4.1 are calculated in the Hartree approximation. We started again at $B = 0$, $T = 0$ and inserted in each of the following iteration steps the previously calculated potential $V(x)$ into the eigenvalue problem of Eq. (2.5), took each mesh point x_n as center coordinate X and diagonalized the problem in the space spanned by the eight lowest-energy

unperturbed Landau-Hermite functions

$$\phi^0_{n,X}(x) = \frac{\exp(-[x-X]^2/2l^2)}{\sqrt{2^n n!\sqrt{\pi}l}}\, H_n([x-X]/l)\,, \tag{4.1}$$

where $H_n(\xi)$ is the n-th order Hermite polynomial. The resulting energy eigenvalues and -functions were used to calculate the electron density according to Eq. (2.6). The overall appearance of the Hartree results for the density profiles and also the wide plateaus for the higher B value (see lower inset of Fig. 4.1) are in good agreement with those of the TFA. The narrow plateaus, obtained in the TFA for the lower B value, are now however smeared out. As is clearly seen in the upper inset of Fig. 4.1, the Hartree result for the filling factor $\nu(x)$ crosses the value 2 with a finite slope.

The essential qualitative difference between the Hartree approximation and the TFA is the neglect of the extent of the wavefunctions in the latter. So we interpret the smearing-out of narrow incompressible strips in the Hartree approximation as being due to the finite width of the wave functions. To check this idea, we consider a "quasi-Hartree" approximation (QHA) in which, instead of solving the problem of Eq. (2.5), we replace the wavefunctions by the eigenfunctions (4.1) of the unconfined Landau problem and take the energy eigenvalues from Eq. (2.7). The latter would be correct in the sense of a lowest order perturbation approximation with respect to the effective confining potential $V(x)$, if $V(x)$ would be a linear function of position over the extent of the unperturbed wavefunction $\phi^0_{n,X}(x)$. The numerical effort with this QHA is much less than that required for the full Hartree approximation, since no numerical calculation of energy eigenvalues and -functions is necessary. Density profiles calculated within this QHA are also shown in Fig. 4.1 as dash-dotted lines. It is seen that the results are very similar to those of the full Hartree calculation, in particular also the results for the smearing-out of the incompressible strips. Apparently the smearing effect of the QHA is even stronger than that of the full Hartree approximation. This is understandable, since the Hartree wavefunctions are asymmetrically squeezed in space regions of a rapid variation of $V(x)$, and therefore have a smaller spatial extent than the unperturbed Landau wavefunctions.

In Fig. 4.3 we compare the widths of incompressible strips with $\nu(x) = 2$ for several approximations. The line labeled CSG is the analytical half-plane result of Chklovskii *et al.* [10], $\bar{a}_{\nu_{ic}} = 16\sqrt{a_0 d_0/\pi}\sqrt{\nu_{ic}/[\nu_0^2 - \nu_{ic}^2]}$, with $d_0 \sim 150\,\mathrm{nm}$ a depletion length, $\nu_{ic}\,(=2)$ the filling factor of the incompressible strip, and $\nu_0 = 2E_F^0/\hbar\omega_c$ the effective filling factor. [12] This result agrees well with the corresponding self-consistent result of Ref. [12] and for sufficiently low B values (note the inverted B scale in Fig. 4.3) also with our present TFPA result for samples of finite width. For small B values, the width decreases proportional to B, and remains finite throughout the figure.

The result calculated from the QHA is also included in Fig. 4.3. As for the TFPA, the width of the incompressible strips is determined by a simple extrapolation, using three points next to

a plateau to determine a plateau edge. For wide plateaus (large B values), the QHA width is only slightly smaller than that calculated within the TFA. However, with decreasing B the QHA width decreases faster and goes to zero at a relatively large magnetic field ($\hbar\omega_c/E_F^0 \approx 0.7$), far before the incompressible strips with $\nu(x) = 4$ develop in the center of the sample.

These results require a modification of Fig. 4.2. Within the Hartree-type approximation, the width of the incompressible strip with filling factor 2 shrinks more rapidly with decreasing B and vanishes at $\hbar\omega_c/E_F^0 \approx 0.7$. Between this B value and the value $\hbar\omega_c/E_F^0 \approx 0.5$ no incompressible strips exist in the sample. At still lower B values there is a B-interval in which only incompressible strips with local filling factor 4 can exist. In Fig. 4.4a we also compare the density profiles obtained from TFA (solid lines) and QHA (dashed-dotted lines) for an intermediate B value. Although the profiles look similar for both approximations at local filling factor four, they do differ for $\nu(x) = 2$ (see the insets). This qualitative difference reflects the importance of taking in to account the finite extent of the wavefunctions. We show the filling factor profiles calculated within TFA (left panel) and QHA (right panel) in Fig. 4.4 b. We observe the incompressible strip with local filling 2 for all the magnetic field values considered if $\nu(0) > 2$ within TFA whereas persists only for a finite interval within the QHA. This modification required by the QHA is also indicated in Fig. 4.9 below.

In view of the following it may be interesting to note that the essential effects of the Hartree-type approximations can be simulated in a very simple way. If one first performs a calculation within the TFPA and then takes a spatial average, e.g., $\bar{\nu}(x) = (2\lambda)^{-1}\int_{-\lambda}^{\lambda} dx'\nu(x+x')$, of the filling factor profile $\nu(x)$, one will smear-out incompressible strips of a width less than 2λ, while incompressible strips with a width larger than 2λ will survive. With λ of the order of the magnetic length, one will obtain filling factor profiles $\bar{\nu}(x)$ very similar to those obtained in the Hartree approximation.

4.3 Incompressible strips and distribution of dissipative current

4.3.1 The local conductivity model

We now describe the effect of an applied current on the Hall bar system, following again the approach of Ref. [27]. In the presence of a dissipative current I, the electrochemical potential $\mu^*(\mathbf{r})$ will become position dependent, and its gradient $\mathbf{E} = \nabla\mu^*/e$ will drive the current density $\mathbf{j}(\mathbf{r})$. We assume the linear local relation (Ohm's law)

$$\mathbf{j}(x) = \hat{\sigma}(x)\,\mathbf{E}(x), \quad \hat{\sigma}(x) = \hat{\sigma}\big(n_{\rm el}(x)\big), \tag{4.2}$$

with a position-dependent conductivity tensor $\hat{\sigma}(x)$, which has the same form as for a homogeneous sample, however with the homogeneous density replaced by the local electron density $n_{\rm el}(x)$. Due to the translation invariance in the y direction, which is indicated by the notation used in Eq. (4.2), and the equation of continuity, the components j_x and E_y of current density and electric field, respectively, must be constant, [27]

$$j_x(x) \equiv 0, \quad E_y(x) \equiv E_y^0 \,. \tag{4.3}$$

For the other components one finds

$$j_y(x) = \frac{1}{\rho_l(x)} E_y^0 \,, \quad E_x(x) = \frac{\rho_H(x)}{\rho_l(x)} E_y^0 \,, \tag{4.4}$$

in terms of the longitudinal component $\rho_l = \rho_{xx} = \rho_{yy}$ and the Hall component $\rho_H = \rho_{xy} = -\rho_{yx}$ of the resistivity tensor $\hat{\rho} = \hat{\sigma}^{-1}$. For a given applied current $I = \int_{-d}^{d} dx\, j_y(x)$ one obtains for the constant electric field component along the Hall bar

$$E_y^0 = I \left[\int_{-d}^{d} dx \, \frac{1}{\rho_l(x)} \right]^{-1} \,, \tag{4.5}$$

and for the Hall voltage across the sample

$$V_H = \int_{-d}^{d} dx \, E_x(x) = E_y^0 \int_{-d}^{d} dx \, \frac{\rho_H(x)}{\rho_l(x)} \,. \tag{4.6}$$

With the usual normalization of the resistances to a square-shaped conductor, this yields for the Hall and the longitudinal resistance (normalized on a square sample of length $2d$)

$$R_H = \frac{V_H}{I} \,, \quad R_l = \frac{2dE_y^0}{I} \,. \tag{4.7}$$

Here one sees the essence of the local model. Any reasonable model for the conductivity of a high-mobility 2DES at zero temperature will give simple results for the conductivity components at even-integer filling factors (where no elastic scattering is possible):

$$\sigma_l(\nu{=}2k) = \rho_l(\nu{=}2k) = 0 \,, \tag{4.8}$$

$$\sigma_H(\nu{=}2k) = \frac{1}{\rho_H(\nu{=}2k)} = \frac{e^2}{h} \, 2k \,. \tag{4.9}$$

Thus, if an incompressible strip of finite width exists in the sample, the integral in Eq. (4.5) diverges and E_y^0 and, therefore, the longitudinal resistance R_l is zero. At low temperatures, $k_B T \ll \hbar\omega_c$, $\rho_l(\nu{=}2k)$ and, therefore, R_l will be exponentially small and relevant contributions to the integral come only from the incompressible regions.

The integral in Eq. (4.6) has the same type of singularity. If only incompressible strips with the same value $\nu(x) = 2k$ of the local filling factor exist, this singular integral is just the

$2k$-fold of the integral in Eq. (4.5), so that one gets the quantized result $R_H = h/(2ke^2)$. At zero temperature one can evaluate the singular integrals by first introducing a cutoff, e.g. by replacing $\rho_l(x)$ with $\rho_l^\epsilon(x) = \max[\epsilon, \rho_l(x)]$, then calculating the integrals, and finally removing the cutoff ($\epsilon \to 0$). This yields exact quantization of the Hall resistance, and the corresponding calculation at very low temperatures yields exponentially small corrections. If incompressible strips of finite widths with different values of $\nu(x)$ exist, e.g. due to a manipulation of the background potential, other values for the Hall resistance may be possible. But, as it has been shown in the previous section, from the Hartree-type approximations, such a situation will not occur in the simple translation-invariant Hall bar geometry. From these arguments one expects in the resistance-versus-B curves plateau regions of finite widths, where the resistances have the well known quantized values.

These considerations are quite general and do not depend on details of the conductivity model. On the other hand, if one wants to calculate the resistances between the plateau regions, one needs to specify a conductivity model, and the results will depend on details of this model. We will present such detailed results in Sec. 4.4 below.

4.3.2 Limitations of the local model

In Sec. 4.2 we have shown that, within a Hartree-type approximation, incompressible strips of a width smaller than the extent of typical wavefunctions are smeared out. As a consequence, incompressible strips with a given filling factor $2k$ do exist only in a finite interval of magnetic fields. For lower B values, the $\nu(x)$ profile crosses the value $2k = \nu(\tilde{x}_{2k})$ with finite slope at some point $x = \tilde{x}_{2k}$. At zero temperature, the integrals in Eqs.(4.5) and (4.6) become singular since $\rho_l(\tilde{x}_{2k}) = 0$. Whether the singularity is integrable or not depends on the filling-factor-dependence of the longitudinal conductivity, $\sigma_l(\nu)$. For the SCBA model, to be considered below, it is integrable, for the Gaussian model considered by GG it is not. But should one worry about such sophisticated questions depending on details of the conductivity model? We think one should not, for the following reasons.

All quantities that are related by Eq. (4.2), the current density, the conductivity and the gradient of the electrochemical potential, represent local values of physical variables, which are defined by macroscopic statistical arguments. In principle, they have to be calculated as average values over sufficiently small subsystems, which nevertheless should contain many electrons. One can not expect that the local relation (4.2) still holds on a length scale of the order of the mean distance between the constituents of the 2DES, or, equivalently, of the order of the Fermi wavelength λ_F. On such a length scale one should consider a non-local version of Ohm's law instead. This would, however, make things much more complicated, and we will not enter such problems.

In order to simulate qualitatively the expected effects of a non-local treatment, we start as

before with a local model for the conductivity tensor, take the spatial average over a length scale of the order of λ_F, e.g. with $\lambda = \lambda_F/2$ as

$$\hat{\bar{\sigma}}(x) = \frac{1}{2\lambda} \int_{-\lambda}^{\lambda} d\xi \, \hat{\sigma}(x+\xi) \,, \tag{4.10}$$

and use still the local version (4.2) of Ohm's law, but now with the averaged conductivity tensor (4.10). As a consequence, the resistivity components occurring in Sec. 4.3.1 have to be calculated by tensor inversion of $\hat{\bar{\sigma}}(x)$.

This simple simulation of non-local effects has several appealing aspects. First, if $\sigma_l(x)$ vanishes at an isolated position $x = \tilde{x}_{2k}$, the averaged $\bar{\sigma}_l(x) > 0$ will be positive in the neighborhood of $\tilde{x}_{2k}$, and the integrals in Eqs. (4.5) and (4.6) will not be singular. Intervals of vanishing $\bar{\sigma}_l(x)$ will exist only, if one starts before averaging with sufficiently wide incompressible strips (wider than 2λ). Finally, for high-mobility systems, the Hall conductivity is given to a very good approximation by the free-electron value $\sigma_H(x) = (e^2/h)\nu(x)$. Thus, the averaged Hall conductivity $\bar{\sigma}_H(x)$ will be given by the averaged filling factor profile $\bar{\nu}(x)$. As mentioned at the end of Sec. 4.2, this averaged profile will agree qualitatively with the Hartree profile, if we start with the TFPA profile $\nu(x)$ and average over $\lambda \sim l$ (l the magnetic length). Since for the large magnetic fields of interest $l \lesssim \lambda_F$, there is actually no need to perform the time consuming Hartree calculation, if one finally wants to calculate the averaged conductivity tensor (4.10).

To summarize, our approximation scheme that simulates both, the effect of finite width of the wavefunctions in the thermal equilibrium calculation, and non-local effects on the transport, is as follows. We calculate the density profile $\nu(x)$ within the self-consistent TFPA, and with this the conductivity tensor $\hat{\sigma}\big(\nu(x)\big)$. Then we perform the averaging of Eq. (4.10) and follow the calculations described in Sec. 4.3.1. In contrast to Ref. [27] we restrict our calculations here to the linear response regime and do not investigate the feedback of the applied current on the electron density and the electrostatic potential, that is mediated in principle by the position-dependent electrochemical potential $\mu^*(\mathbf{r})$ in the presence of a dissipative current.

4.3.3 Self-consistent Born approximation

In principle one could use the conductivity models of Ref. [27] in order to calculate explicit examples. We prefer, however, to take the transport coefficients from the self-consistent Born approximation (SCBA), [59,68,69] which allows for consistent models of longitudinal and Hall conductivities, and for the consideration of anisotropic scattering by randomly distributed finite-range impurity potentials. We assume that the relevant scatterers are charged donors distributed randomly in a plane parallel to that of the 2DES, with an areal density n_I, and we approximate the impurity potentials by Gaussian potentials

$$v(\mathbf{r}) = \frac{V_0}{\pi R^2} \exp\left(-\frac{r^2}{R^2}\right) \,, \tag{4.11}$$

with a range R of the order of the the spacing between 2DES and doping layer. The details of the Gaussian model are presented in appendix B.

An important aspect of the SCBA is that, similar to the "lowest order cumulant approximation" used in Ref. [27], it allows to treat the transport coefficients and the collision broadening of the LLs in a consistent manner. The relevant SCBA results for the transport coefficients and the collision broadening of a homogeneous 2DES are summarized in the appendix. Consistency with the transport coefficients requires that one replaces in the self-consistent TFPA calculations the δ-functions of the Landau DOS (2.9) by the semi-elliptic spectral functions (B.5). In addition to the range R, the impurity strength V_0 and concentration n_I determine these quantities via the relaxation time τ_0 defined by the energy $\hbar/\tau_0 = n_I V_0^2 m/\hbar^2$. In strong magnetic fields, this energy combines with the cyclotron energy to

$$\Gamma^2 = 4n_I V_0^2/(2\pi l^2) = (2/\pi)\,\hbar\omega_c\,\hbar/\tau_0, \tag{4.12}$$

where Γ is the width of the LLs in the limit of zero-range scattering potentials ($R \to 0$). We find it convenient to characterize the impurity strength by the dimensionless ratio $\gamma = \Gamma/\hbar\omega_c$ at the strong magnetic field $B = 10\,\mathrm{T}$ and define (for GaAs), therefore, the strength parameter

$$\gamma_I = \left[(2n_I V_0^2 m/\pi\hbar^2)/(17.3\,\mathrm{meV})\right]^{1/2}. \tag{4.13}$$

Figure. 4.5 shows the effect of collision broadening on the density profile at strong magnetic fields. The sample parameters are $d = 1.5\,\mu$m, $n_0 = 4 \cdot 10^{11}\mathrm{cm}^{-2}$ and $b/d = 0.952$, resulting in $\bar{n}_{\mathrm{el}} = 3.37 \cdot 10^{11}\mathrm{cm}^{-2}$ and $E_F = 12.02\,$meV, $E_F^0 = 13.51\,$meV. Data are shown for $t = k_B T/E_F^0 = 0.01$, three values of the magnetic field ($\hbar\omega_c/E_F^0 = 0.6,\ 0.8$, and 0.95, corresponding to central filling factors $\nu(0) = 3.33,\ 2.5$, and 2.1, respectively), and for three sets of the impurity parameters R and γ_I. It is seen from Fig. 4.5 and Table 4.1 that, for sufficiently small collision broadening (small γ_I and, eventually, large R), incompressible strips still may exist, that their width decreases, however, with increasing broadening of the LLs. Table 4.1 shows, for several sets of impurity parameters, the relative widths γ_n of the lowest LLs and the zero field mobilities. Data for the second set ($R = 10\,$nm, $\gamma_I = 0.1$) are not included in Fig. 4.5, since they could not be distinguished from the traces for the first, high-mobility set. From the insets of Fig. 4.5 it is evident that incompressible strips can only survive, if the gap between the broadened LLs remains broad enough. A large collision broadening (low-mobility set No. 4) has a similar effect as a spatial averaging (long-dashed lines in Fig. 4.5) and may smear out the incompressible strips.

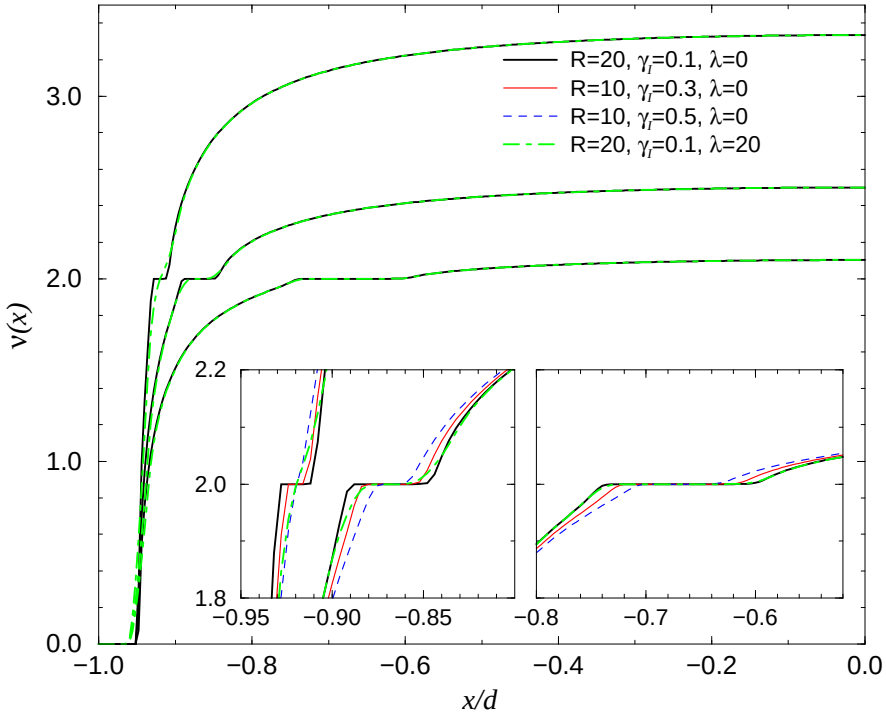

Figure 4.5: Filling factor $\nu(x) \approx h\,\sigma_H(x)/e^2$ versus position in the left half of a symmetric high-mobility ($R = 20$ nm, $\gamma_I = 0.1$) Hall bar of width $d = 1.5\,\mu$m, for three values of the magnetic field, $\hbar\omega_c/E_F^0 = 0.6,\ 0.8$, and 0.95, and without ($\lambda = 0$, solid black lines) and with ($\lambda = 20$ nm, long-dashed green lines) averaging according to Eq. (4.10). The insets show the plateau regions (incompressible strips) enlarged and include in addition two results for larger collision broadening but no averaging ($\lambda = 0$). Other specifications in the text.

4.4 Results and discussion

4.4.1 Effect of spatial averaging

The effect of spatial averaging, introduced to simulate non-local effects on the scale of the Fermi wavelength, is illustrated in Fig. 4.6. It shows, for a magnetic field value corresponding to a central filling factor $\nu(0) = 4.18$, the filling factor profile calculated within the TFPA using the SCBA broadened DOS, together with the conductivity profiles, Fig. 4.6(a). Here we have assumed a short-range potential (leading to the rather low mobility $\mu_{B=0} = 6.4\,\mathrm{m^2/Vs}$), in order to obtain a noticeable deviation of the $\sigma_H(x)$ trace from that for the filling factor $\nu(x)$. Clear incompressible strips with the quantized values for $\sigma_H(x)$ and vanishing $\sigma_l(x)$ are visible where $\nu(x)$ assumes the integer values 4 and 2. The effect of spatial averaging on the conductivities is demonstrated in (b) and (c). The wide (~ 90 nm) plateau defined by $\nu(x) = 4$ shrinks due to

No.	R [nm]	γ_I	γ_0	γ_1	γ_2	$\mu_{B=0}$
1	20	0.1	0.07	0.06	0.05	747.5
2	10	0.1	0.11	0.08	0.07	75.1
3	10	0.3	0.34	0.24	0.21	8.34
4	10	0.5	0.56	0.40	0.35	3.00

Table 4.1: Relative width $\gamma_n = \Gamma_n/\hbar\omega_c$ of the Landau levels $n = 0,\ 1,\ 2$ at $\hbar\omega_c/E_F^0 = 0.6$, and mobility $\mu_{B=0}$ at $B = 0, T = 0$ in units of m^2/Vs, for four sets of model parameters R, γ_I.

the averaging (to ~ 50 nm) but clearly survives, as is shown in Fig. 4.6(b) for $\sigma_l(x)$, and holds similarly for the plateau of $\sigma_H(x)$. On the other hand, the plateau behavior near the narrow (~ 25 nm) strip defined by $\nu(x) = 2$ is completely smeared out, and $\sigma_l(x)$ does no longer vanish in this region, Fig. 4.6(c). This has, of course, drastic consequences for the current distribution, which is dominated by the strips with vanishing $\sigma_l(x)$, i.e., vanishing $\rho_l(x)$, see Eq. (4.4). Without averaging a finite fraction of the total current would flow through the incompressible strips with $\nu(x) = 2$ (on both sides of the sample). With the averaged conductivity tensor, the total current must flow through the incompressible strips with $\nu(x) = 4$ (assuming that there $\sigma_l(x) = 0$ holds exactly).

The mechanism illustrated in Fig. 4.6 is, of course, also effective at other values of the magnetic field. At larger B with $\nu(0) \gtrsim 2$, broad incompressible strips with $\nu(x) = 2$ will exist near the center of the Hall bar, and the spatially averaged conductivities will show clear plateau behavior. With decreasing B, the incompressible strips move from the center towards the sample edges and shrink. If the strip width becomes of the order of 2λ or smaller, the averaging according to Eq. (4.10) will destroy the plateau behavior of the conductivities and $\bar{\sigma}_l(x)$ will no longer vanish near the strips. Then the current density still may have a (finite) maximum near the strips with $\nu(x) = 2$, but a finite amount of current will spread over the bulk of the sample, and the global resistances will no longer have the quantized values $R_H = h/2e^2$ and $R_l = 0$. The above considerations about the current distribution can be easily seen in Fig. 4.7 where we show the current density (upper panel) together with the calculated density profile (gray scale) and resistance curves. For the high magnetic field values $\widetilde{B} = \hbar\omega_c/E_F^0 > 1.05$ there exists no incompressible strip and the current density simply follows the electronic distribution, whereas we observe a finite maximum at the current distribution if $\nu(0) \lesssim 2$. By decreasing the field strength we see that the current is confined to the intervals where we observe incompressible strips, which are wider than the averaging length ($\widetilde{B} = 0.99$). For still lower $\widetilde{B}(= 0.78)$ we see two local maxima of finite height, near $\nu(x) = 2$ as expected.

Figure 4.8 shows typical results for the dependences of the global resistances on magnetic field and averaging length, as calculated from Eq. (4.7). At high magnetic fields, $\hbar\omega_c > E_F^0$, everywhere in the sample $\nu(x) < 2$ holds, and no incompressible strips exist. The filling factor

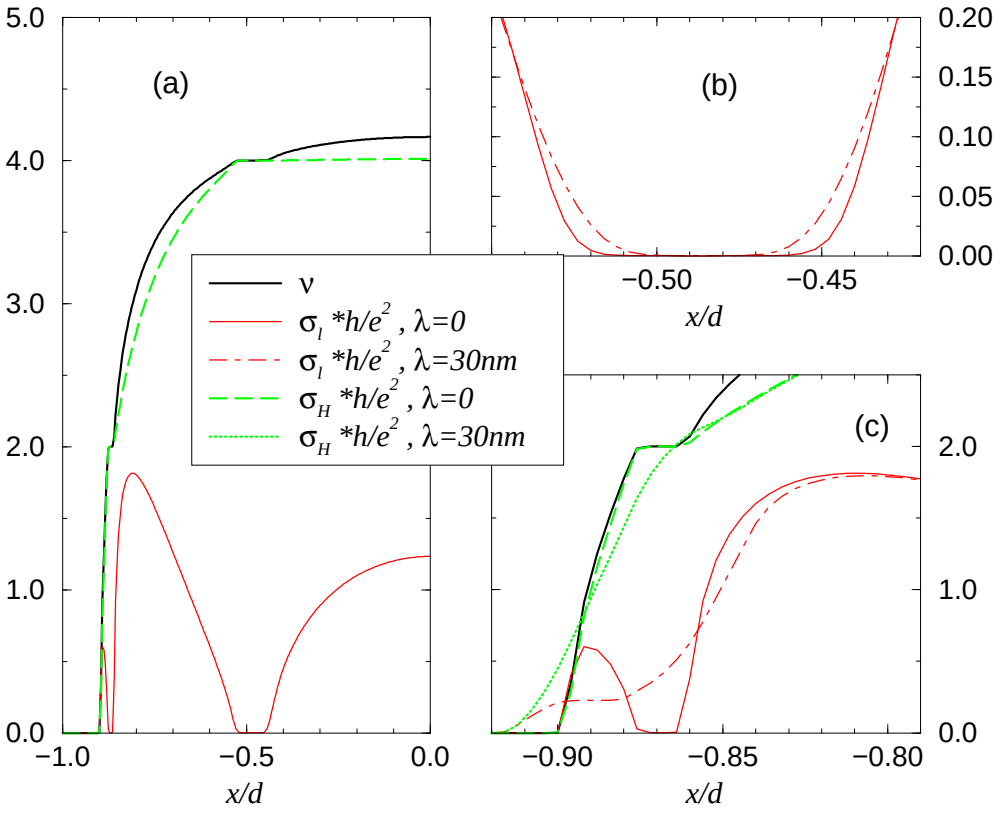

Figure 4.6: (a) Filling factor and conductivity profiles for the left half of a symmetric sample with $d = 1.5\,\mu$m, $n_0 = 4 \cdot 10^{11}$cm^{-2}, $b = 0.9d$, calculated within the SCBA, for $R = 0.1$ nm and $\gamma_I = 0.1$, $\hbar\omega_c/E_F^0 = 0.48$, and $k_BT/E_F^0 = 0.01$. (b) and (c) repeat the data of (a) (solid lines) near the incompressible strips with filling factors $\nu(x) = 4$ and $\nu(x) = 2$, respectively. The dash-dotted lines demonstrate the effect of spatial averaging, according to Eq. (4.10), with $\lambda = 30$ nm.

and consequently the conductivities and the current density vary slowly across the sample. Thus, the spatial averaging has little effect and, within the accuracy of the figure, the results with and without averaging agree. For slightly lower magnetic fields, $\hbar\omega_c \lesssim E_F^0$, broad incompressible strips exist near the center of the sample and, for all the considered averaging lengths λ, strips of finite width with $\sigma_l(x) = 0$ and $\sigma_H(x) = 2e^2/h$ survive. As a consequence, the resistances are quantized, independently on the width of these strips.

For still lower B values the situation becomes more complicated. Within the TFPA, incompressible strips exist for all these B values. Without spatial averaging, $\sigma_l(x)$ vanishes on these strips and, as a consequence, $R_l = 0$, and, for $\hbar\omega_c/E_F^0 > 0.5$, $R_H = h/2e^2$, as shown by the traces for $\lambda = 0$. For $\hbar\omega_c/E_F^0 < 0.5$ there are two types of incompressible strips, with $\sigma_H(x) = 2e^2/h$ or $4e^2/h$, and, without averaging, both contribute according to their widths

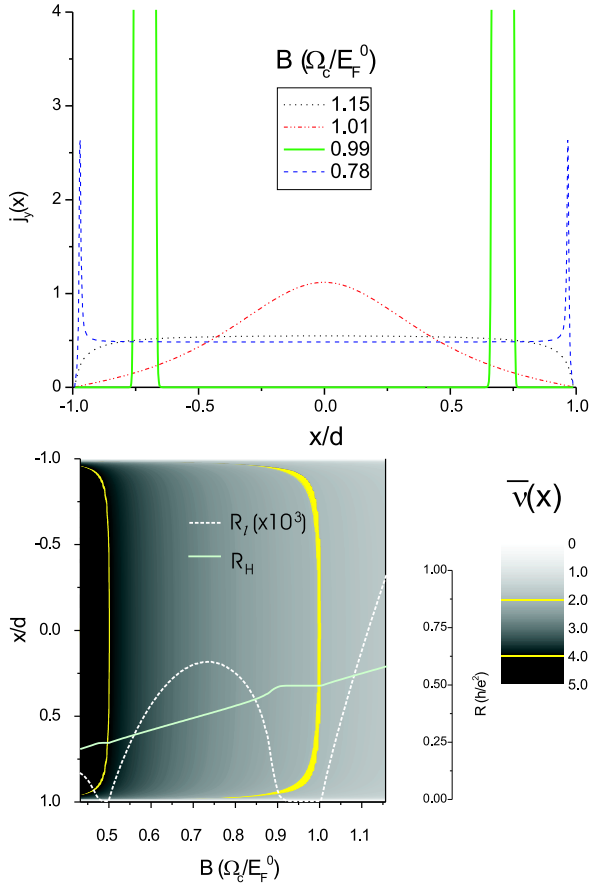

Figure 4.7: (upper panel) Current distribution for selected B values. Only for $\Omega_c/E_F^0 = 0.99$ (solid line) the current is confined to the incompressible strips, which survived the averaging. $\lambda = 40$nm. (lower panel) Gray scale plot of the averaged $\bar{\nu}(x) \approx (h/e^2)\,\bar{\sigma}_H(x)$ versus B and x, together with Hall (solid) and longitudinal (broken light line) resistance; $d = 7.5\mu$m, $\lambda = 20$nm, $k_BT/E_F^0 = 0.02$. Impurity potential parameters are given in table 4.1 for sample No.1.

to R_H, while still $R_l = 0$. The fluctuations in the R_H curve for $\lambda = 0$ result from the TFPA calculation on a finite mesh ($N = 500$), which yields discontinuous changes of the widths of the incompressible strips with changing B. This unsatisfactory picture, obtained for $\lambda = 0$, results from the model calculation of Ref. [27].

The introduction of the spatial averaging improves this situation dramatically and leads to qualitatively correct results. With decreasing B the incompressible strips with $\nu(x) = 2$ become narrower. As the width becomes smaller than 2λ, $\bar{\sigma}_l(x)$ no longer vanishes, the integrals in Eqs. (4.5) and (4.6) and thus R_l become finite. This happens at higher B values if λ is larger, and the resistances near the low-magnetic-field edge of the quantum Hall plateau depend strongly on λ. While $\bar{\sigma}_l(x)$ may have a sharp minimum near the strips with $\nu(x) = 2$ if the width of these

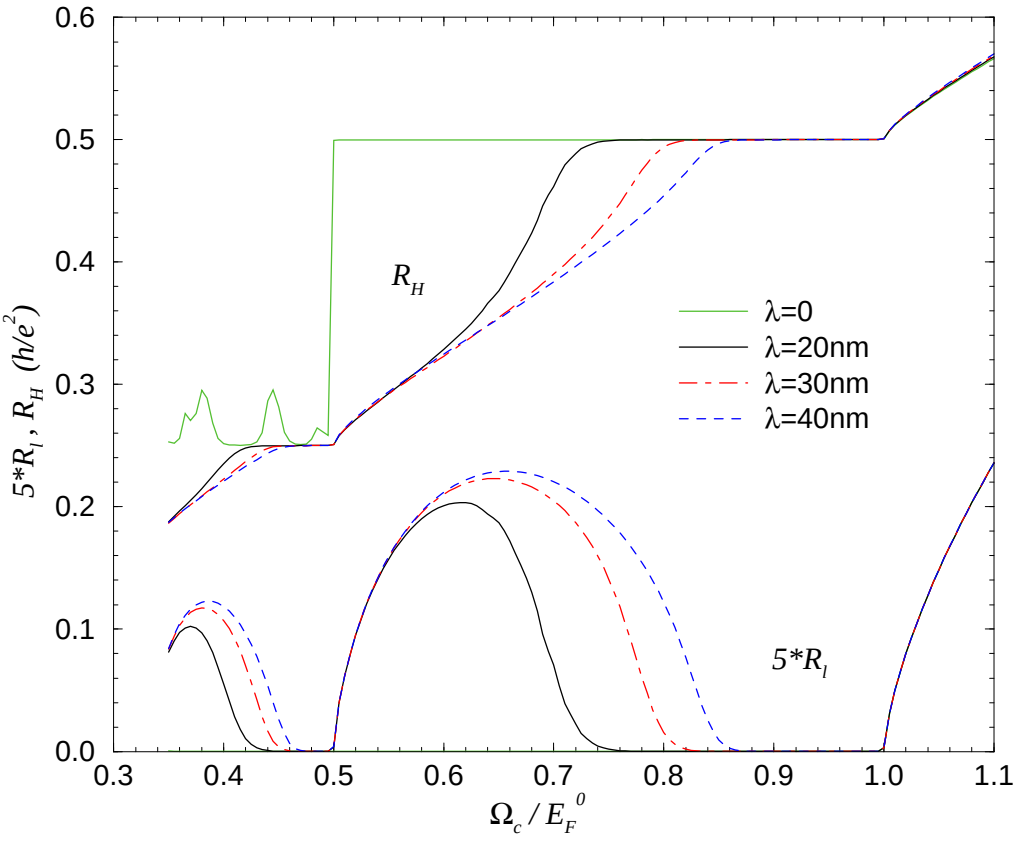

Figure 4.8: Calculated Hall and longitudinal resistances versus scaled magnetic field $\hbar\omega_c/E_F^0$, for different values of the averaging length λ. The sample parameters are $d = 1.5\,\mu$m, $n_0 = 4 \cdot 10^{11}$cm^{-2}, $b = 0.952d$, $R = 10\,$nm and $\gamma_I = 0.1$, and $k_BT/E_F^0 = 0.01$.

strips is only slightly smaller than 2λ, this minimum, and also the corresponding maximum of the current density, will smoothen out as the width of the strips becomes much smaller than 2λ. Then the total resistances will become nearly independent of λ, as is seen in Fig. 4.8 for $0.5 < \hbar\omega_c/E_F^0 \lesssim 0.6$. For $\hbar\omega_c/E_F^0 \lesssim 0.5$, $\bar{\sigma}_l(x)$ vanishes only within the incompressible strips with $\nu(x) = 4$, but not in strips with $\nu(x) = 2$. As a consequence, one obtains again the exactly quantized results for R_H and R_l.

To visualize the intimate connection between the existence of incompressible strips of finite width [now with constant $\bar{\sigma}_H(x) \approx e^2\bar{\nu}(x)/h$], we show in Fig. 4.9 and Fig. 4.7 a gray scale plot of the spatially averaged filling factor profile for a relevant interval of magnetic fields, together with the resulting resistances.

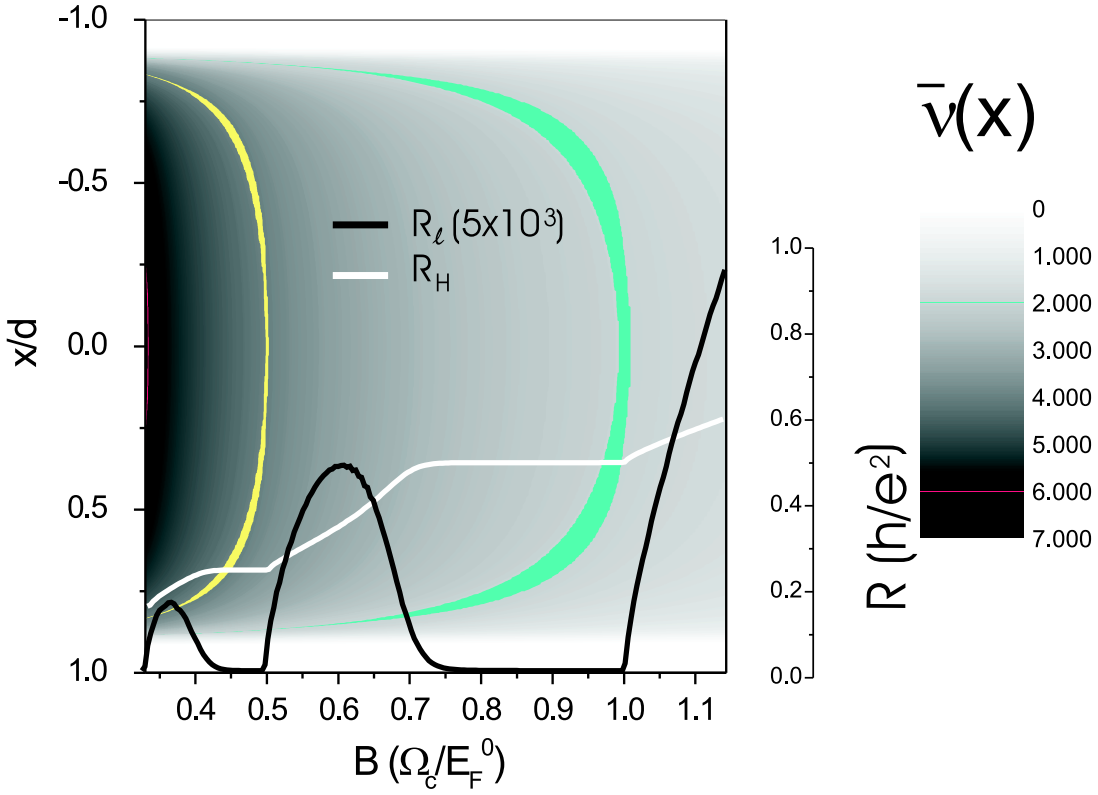

Figure 4.9: Calculated Hall resistance (light solid line) and (scaled) longitudinal resistance (black solid line) versus magnetic field, measured in units of $\hbar\omega_c/E_F^0$ at temperature $k_BT/E_F^0 = 0.0124$. Impurity potential parameters are given in table 4.1 for sample No.1. The underlying gray scale plot shows the averaged ($\lambda = 20$nm) filling factor profile, as in Fig. 4.2. The crescent-like areas indicate the regions of incompressible strips with local filling factors 2 (right) and 4 (left).

4.4.2 Effect of temperature and collision broadening

The spatial averaging procedure is essential to obtain quantum Hall (QH) plateaus of finite width for the $R_l(B)$ and the $R_H(B)$ curves and to obtain the correct quantized values for $R_H(B)$ on the plateaus corresponding to filling factors larger than two. The width of the calculated QH plateaus does, however, not only depend on the averaging length λ, but also on the temperature and on the broadening of the LLs due to the impurity scattering, since both affect the width of the incompressible strips. The effect of collision broadening on the width of incompressible strips has been indicated in Fig. 4.5. The temperature effect has been investigated in Ref. [12], where it was shown that, in the absence of collision broadening, i.e., on the basis of the bare Landau DOS (2.9), the incompressible strips have a finite width at zero temperature. At finite, increasing temperatures, the width shrinks (while the value of the filling factor remains exactly

constant within the remaining strip) until at a sufficiently high temperature ($k_BT \lesssim \hbar\omega_c/25$ in Ref. [12]) the width collapses to zero. A similar result is expected in the presence of collision broadening. In particular one should expect that, within the self-consistent TFPA based on the SCBA DOS, the existence of an energy gap between two adjacent broadened LLs will always lead to an incompressible strip, provided the temperature is low enough. The necessary temperature will be the lower, the narrower the gap is. But we will not discuss these questions in further details.

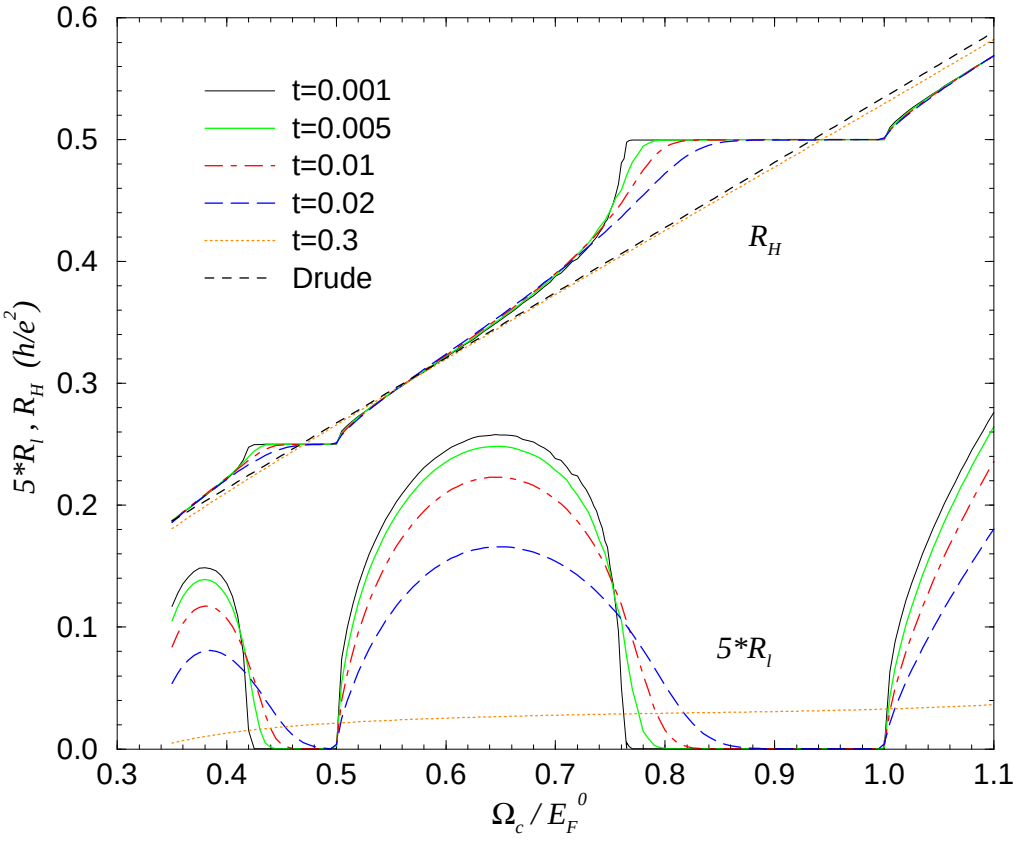

Figure 4.10: Hall and longitudinal resistances versus magnetic field, calculated for different temperatures, $t = k_BT/E_F^0$. Sample parameters: $d = 1.5\,\mu$m, $n_0 = 4 \cdot 10^{11}\text{cm}^{-2}$, $b = 0.952d$, $R = 10\,$nm and $\gamma_I = 0.1$, $\lambda = 30\,$nm.

The temperature effect on the calculated resistance curves is shown in Fig. 4.10. As expected, the width of the QH plateaus increases monotonically with decreasing temperature, but apparently it has a finite limit for $T \to 0$. We have also included the high-temperature result for $k_BT/E_F^0 = 0.3$ (since $E_F^0 = 13.5\,$meV, this means $T \approx 47\,$K). At the low-B side of the figure $k_BT \sim \hbar\omega_c$, and the derivative of the Fermi function overlaps about two LLs. Since we consider only the lowest Landau levels ($n = 0,\ 1,\ 2$), our calculation is not correct in this limit. Nevertheless it is interesting to compare this result with the Drude result, which should be valid

if the Shubnikov–de Haas oscillations are smeared out at higher temperatures.

In the Drude approximation one has $\rho_H(x) = \omega_c\tau_{tr}\,\rho_l(x)$, with $\rho_l(x) = 1/\sigma_0(x)$, where $\sigma_0(x) = e^2\tau_{tr}n_{\rm el}(x)/m$ is independent of the magnetic field. Inserting this into Eq. (4.5), one obtains

$$\frac{I}{E_y^0} = \frac{e^2\tau_{tr}}{m}\,2d\,\bar{n}_{\rm el} = \frac{e^2}{h}\,\frac{2E_F}{\hbar/\tau_{tr}}\,. \tag{4.14}$$

In Eq. (4.6) the integrand is taken to be $\omega_c\tau_{tr}$, but only for $|x| < b$, where $n_{\rm el}(x)$ is not exponentially small, and $V_H/E_y^0 = 2b\,\omega_c\tau_{tr}$ is obtained. With Eq. (4.7) one obtains the Drude result

$$R_H^D = \frac{h}{e^2}\,\frac{b}{2d}\,\frac{E_F^0}{E_F}\,\frac{\hbar\omega_c}{E_F^0}\,, \quad R_l^D = \frac{h}{e^2}\,\frac{\hbar/\tau_{tr}}{2E_F}\,. \tag{4.15}$$

The energies E_F and E_F^0 are calculated numerically from the density profile at $B = 0, T = 0$, as is described above, and τ_{tr} is calculated as described in the appendix, with $k_F = \sqrt{2\pi\bar{n}_{\rm el}}$. The Hall resistance calculated from the Drude result is plotted as dashed straight line in Fig. 4.10.

Finally, Fig. 4.11 shows the effect of the Landau level broadening on the QH plateaus at a fixed, relatively low temperature. The corresponding widths of the lowest LLs, in units of the cyclotron energy $\hbar\omega_c$, are given in Table 4.2 for the lowest and the largest B value shown in the figure. For the largest damping, the LLs start to overlap for $\hbar\omega_c/E_F^0 \lesssim 0.4$. so that the $\nu = 4$ QH plateau is not well developed. Note that the SCBA results summarized in the appendix are only valid at higher B values, where the LLs do not overlap.

The two high-mobility situations considered in Fig. 4.11 differ only by the range R of the Gaussian impurity potentials. The larger range leads to slightly smaller level broadening, but to much lower longitudinal resistance (i.e., to much higher mobility at $B = 0$).

R	γ_I	γ_0^l	γ_1^l	γ_2^l	γ_0^h	γ_1^h	γ_2^h	$\mu_{B=0}$
20	0.1	0.117	0.085	0.073	0.043	0.037	0.033	747.5
10	0.1	0.161	0.123	0.105	0.071	0.051	0.044	75.1
10	0.3	0.482	0.369	0.316	0.213	0.152	0.131	8.34
10	0.4	0.643	0.492	0.421	0.284	0.203	0.175	4.69

Table 4.2: Relative widths of the lowest Landau levels, $\gamma_n^l = \Gamma_n/\hbar\omega_c$ for $\hbar\omega_c/E_F^0 = 0.35$, and $\gamma_n^h = \Gamma_n/\hbar\omega_c$ for $\hbar\omega_c/E_F^0 = 1.10$, for the impurity parameters used in Fig. 4.11. First column: range in nm, last column: zero field mobility in m^2/Vs.

4.4.3 Hall potential profile

The motivation of Ref. [27] and our present work came from the experimental investigation [21] of the electrostatic potential distribution across a Hall bar under QH conditions, caused by an

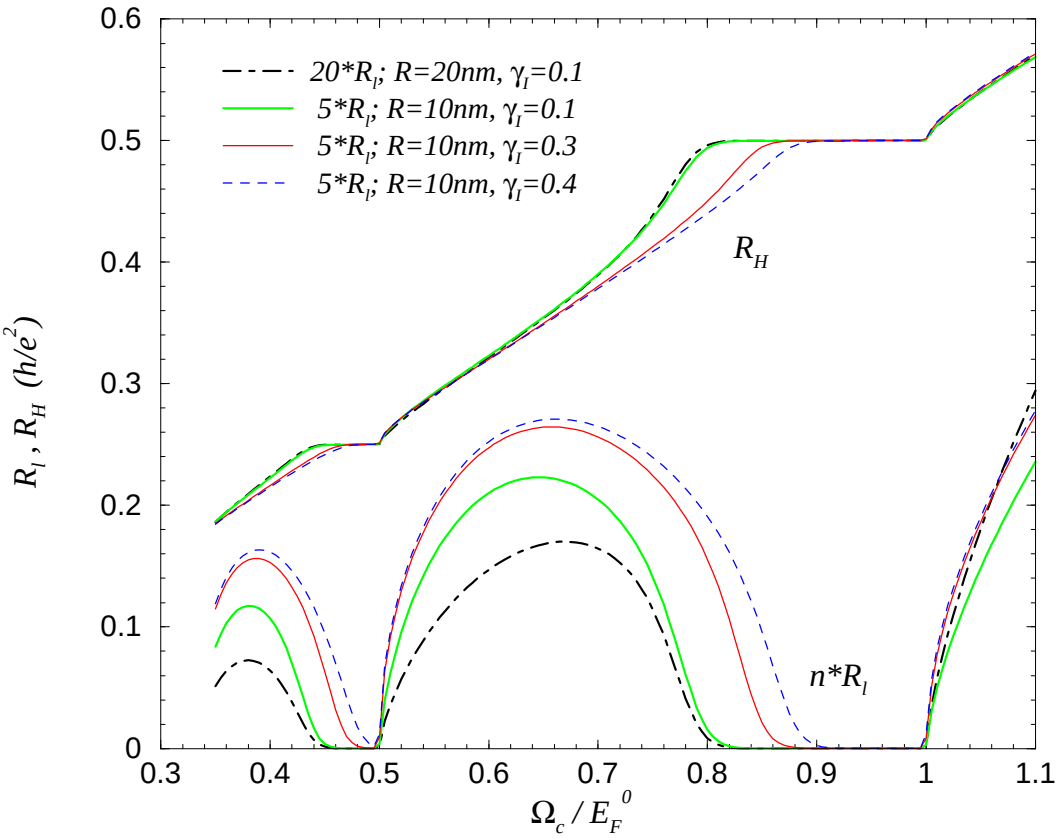

Figure 4.11: Hall and longitudinal resistances versus magnetic field, calculated for different values of the collision broadening. Sample parameters: $d = 1.5\,\mu$m, $n_0 = 4 \cdot 10^{11}\text{cm}^{-2}$, $b = 0.952d$, $\lambda = 30\,$nm, $k_BT/E_F^0 = 0.01$ (i.e., $T = 1.57\,$K).

applied current. We should note that in the mentioned experiments spin splitting is resolved and potential is measured whereas we assume spin degeneracy and consider the potential energy. Ahlswede and coworkers [21, 22] observed three types of potential distribution, depending on the filling factor regime. Type I was a more or less linear variation across the sample and is observed if the filling factor in the center is smaller and relatively close to (but not too close to) an integer n, i.e., $n \gtrsim \nu(0) \gtrsim n - 1/2$. If the center filling is slightly larger than an integer, $n < \nu(0) \lesssim n + 1/2$, type III is observed, characterized by a constant potential in the central region and a rapid variation across (narrow) strips, which move with decreasing B towards the sample edges and have been interpreted as incompressible strips [21]. Finally, type II shows a rapid, non-linear variation of the potential in the center region and is observed if the center filling factor is very close to an integer.

In Ref. [27] it was shown that, in an local equilibrium picture, the changes of the electrostatic potential, caused by an applied current, follows closely the current-induced variation of the electro-chemical potential μ^*, so that the resulting density changes are small. In the present

work we do not consider the feed-back of the spatial variation of μ^* on electrostatic potential and density profiles (linear response). But we expect from the results of Ref. [27], that, in the linear response regime, μ^* should show the same position dependence as the electrostatic potential would do, if the feed-back were calculated.

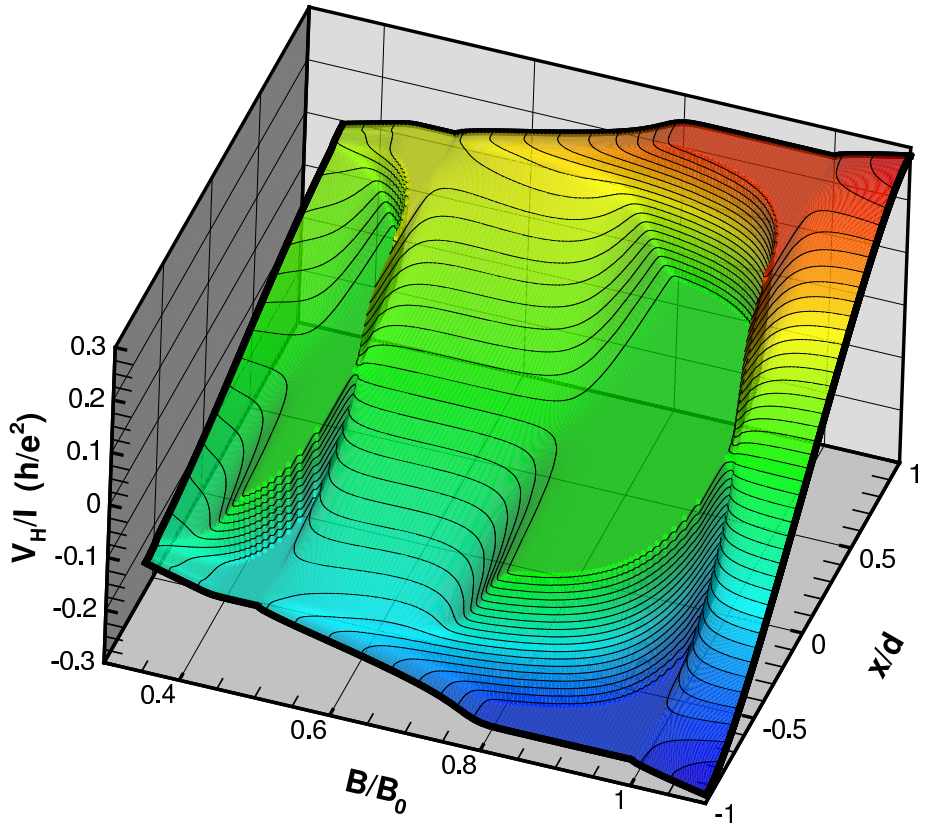

Figure 4.12: Hall potential profile $V_H(x) = \int_0^x dx' E_x(x')$ across the sample, for varying $B/B_0 \equiv \hbar\omega_c/E_F^0$ and constant applied current I. Normalization: $[V_H(d) - V_H(-d)]/I = R_H$; sample parameters: $d = 1.5\,\mu$m, $n_0 = 4{\cdot}10^{11}$cm^{-2}, $b = 0.952d$, $\lambda = 30$ nm, $k_BT/E_F^0 = 0.01$.

To calculate the Hall profile across the sample, we integrate $E_x(x)$, Eq. (4.4), from the center $x = 0$ to the actual x value. Typical results as functions of position x and magnetic field B are shown in Fig. 4.12. The normalization is chosen so that $V_H(B, x = d)/I = -V_H(B, x = -d)/I = R_H/2$. One sees clearly that the plateaus of the quantized Hall effect ($0.8 \lesssim \hbar\omega_c/E_F^0 \lesssim 1$ and $0.45 \lesssim \hbar\omega_c/E_F^0 \lesssim 0.5$) coincide with potential variation of type III, caused by current density confinement to the incompressible strips. Moving from a plateau region to smaller B values, the incompressible strips shrink and finally vanish, and the current density spreads more and more out into the bulk. This leads to the type I behavior

($0.52 \lesssim \hbar\omega_c/E_F^0 \lesssim 0.7$ and $\hbar\omega_c/E_F^0 \lesssim 0.4$). Immediately above the integer values of the center filling factor (in our approximation assuming spin degeneracy near $\nu(0) = 2$ and 4), we find the rapid variation of the type II. This is in very nice agreement with the experiment. Without the spatial averaging of the conductivity tensor, one would have missed the type I regions for $\hbar\omega_c/E_F^0 < 1$, as has been observed in Ref. [27]. A typical result is shown in Fig. 4.13 calculated for the parameters given in Fig. 4.7, where we show the "normalized" Hall potentials for selected values of the magnetic field. We start our discussion of the Hall potential distribution with the $\nu(0) < 2$ regime. The current density profile essentially follows the density profile (see also Fig. 4.7a where $\widetilde{B} = 1.15$) similar to the Drude case, we see a linear potential profile which is denoted as "type I". Whenever the center filling factor becomes very close to an even integer, $\rho_l(0)$ becomes very small, and the current density exhibits a peak at the center, and the potential profile has a strong nonlinear appearance known as type II. In the magnetic field intervals where one observes well developed incompressible strips, the Hall potential drops only across these incompressible strips as seen in Fig. 4.13 ("type III").

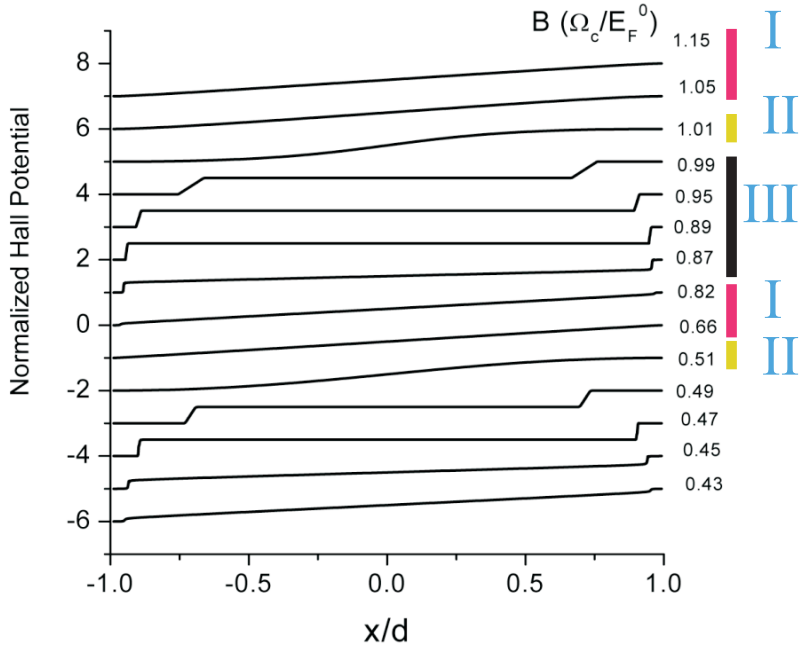

Figure 4.13: Plot of the scaled Hall potential $\Phi(x)/\Phi(d)$, $\Phi(x) = \int_{-d}^{x} d\xi\, \bar{\sigma}_H(\xi)/\bar{\sigma}_l(\xi)$ for selected values of B. A stepwise variation is seen for B in a plateau of the QHE, a linear variation if B is far from a plateau, and a nonlinear variation in the center for B near a plateau edge.

4.5 Summary

The virtue of our approach is, that it allows to calculate resistance traces with exactly quantized quantum Hall plateaus of finite width, and with reasonable values of the resistances between these plateaus. While these intermediate resistance values depend on the details of our conductivity model, the quantized plateau values do not. The reason for this high accuracy and model-independence of the plateau values is the fact, that the latter are determined by the integrals in Eqs. (4.5) and (4.6) becoming singular across incompressible strips.

To obtain realistic widths of the QH plateaus, we had to consider a mechanism that prohibits singular current flow along isolated lines of integer filling factors. We have argued that small-scale non-local transport effects act into this direction, and that consideration of the finite extent of wavefunctions will prohibit arbitrarily narrow ISs at low magnetic fields, in contrast to the prediction of the Thomas-Fermi approximation. We were able to simulate such non-local effects by a simple spatial averaging procedure, with reasonable results for Hall and longitudinal resistance as functions of the magnetic field. Also the resulting potential profile, and therefore the current distribution across the sample, is in nice agreement with recent investigations [21]. We consider this as a strong support for the relevance of our approach, notably because earlier approaches, which neglected dissipation, cannot explain the experiments, as has been discussed in Ref. [27].

For QH plateaus corresponding to filling factors $\nu \geq 4$, our results are qualitatively different form the conventional edge channel picture. The latter explains, for instance, the quantized conductance value $G = 4\,e^2/h$ as the sum of the contributions of two spin-degenerate, quasi-one-dimensional current channels near each of the opposite sample edges, thus tracing back the quantized Hall effect to the phenomenon of 1D conductance quantization (in a situation where no backscattering occurs). [70] That is, the edge states, created by the LLs with quantum numbers $n = 0$ and $n = 1$, contribute both to the current in the plateau regime of the QHE. Our results, on the contrary, indicate that the total current flows along the incompressible strip with local filling factor $\nu(x) = 4$ (where both LLs $n = 0$ and $n = 1$ are occupied), whereas near local filling factor $\nu(x) = 2$ no incompressible strip and no contribution to the current exists.

Comparing the obtained resistance curves with experimental ones, one notices that the high-field edge of a calculated plateau occurs at a magnetic field, at which an incompressible strip (with an even integer value of the effective filling factor $\nu_0 = 2E_F^0/\hbar\omega_c$) first occurs in the center of the sample. In experiments these ν_0 values usually are found somewhere near the centers of the plateaus. There are good arguments to be discussed in the next chapter that this discrepancy is because of neglecting long-range potential fluctuations due to the randomly distributed ionized donors. We have simulated the "short-range" part of the Coulomb potentials of the remote donors by Gaussian potentials, but we have neglected their overlapping long-range parts, which lead to long-range potential fluctuations. We have evaluated the short-range

disorder within the SCBA to calculate conductivities and LL broadening. We have found that with increasing disorder scattering the level broadening increases and, as a result, the widths of the QH plateaus shrinks. On the other hand, one knows from technical applications of the QH effect, that rather impure samples have usually especially wide and stable QH plateaus. This points to the role of long-range potential fluctuations, which become more important with increasing impurity concentration.

As a rough simulation of such long-range fluctuations, we have added oscillatory terms to the confinement potential and then repeated our calculations, which will be the subject of the next chapter. We indeed find that such modulations can widen and stabilize the QH plateaus, and eventually even shift them to higher magnetic fields, depending on the amplitude, the range, and possible other details of the perturbation. This becomes understandable, if one considers the effect of such fluctuations on the existence and the position of incompressible strips. However, we do not want to discuss such considerations further, since we believe that the quasi-one-dimensional model is not appropriate for a reliable discussion of statistical fluctuations of a 2D donor distribution. Effects of long-range disorder in an unconfined 2DES on the longitudinal resistance between QH plateaus have already been discussed a decade ago [71]. This discussion seems however not applicable to the rather narrow samples of the present interest, since, first, the confinement affects the self-consistently calculated potential and thus the density distribution, [24] and, second, the early assumptions about current-carrying and insulating regions are not compatible with our results and the experimental findings [21].

Chapter 5

Disorder

5.1 Donor distribution

The explanation of the integral quantized Hall effect, which is usually discussed within the single particle picture, relies on the fact that the system is disordered. In this model the disorder plays several roles, such as Landau level broadening, finite longitudinal conductivity (σ_l), spatial localization etc. The disorder can be created by inhomogeneous distribution of ions which essentially generates the confining potential. In early days of the QHE, disorder was introduced to obtain finite conductivity along the Hall bar for an unbounded system. In the absence of disorder, the LL's are Dirac delta-functions and the longitudinal conductivity vanishes. For a homogeneous 2DES, by the inclusion of disorder due to scattering, LL's become broadened and the longitudinal conductance becomes finite. Long range potential fluctuations generated by the disorder result in the so called *classical localization*, i.e. the guiding center of the cyclotron orbit moves along closed equipotentials. On the other hand within the Landauer-Büttiker approach (known as the edge channel picture) [72] one also needs localization assumptions in order to obtain QH plateaus of finite width (see for a review e.g. Datta's book [73]). In the previous chapter we have obtained the QH plateaus resulting from screening and the effect of the disorder was included in our calculations via conductivity tensor elements, but the source of the disorder was not investigated. In this thesis, three different geometries (cf. Chap. 3) were investigated within the translation invariance model. In the first geometry, an external potential preserving the periodic boundary conditions was assumed, but the source was not discussed. In the in-plane and mesa-etched geometries, the confinement potential was introduced by homogeneously distributed donors, where for the first geometry the 2DES and donors were assumed to be on the same plane, but for mesa-etched geometry the confinement potential was calculated considering a finite distance in between donors and 2DES.

In the following section we will first discuss the donor distribution for an unit cell without considering the translation invariance in y direction, instead we will assume invariance un-

der translations by lattice constant. Then the overall disorder potential profiles generated by *Coulombic* and *Gaussian* donors will be compared. In the last part of this chapter, the effect of the long-range fluctuations of the confining potential will be discussed, considering two different mobilities and sample widths.

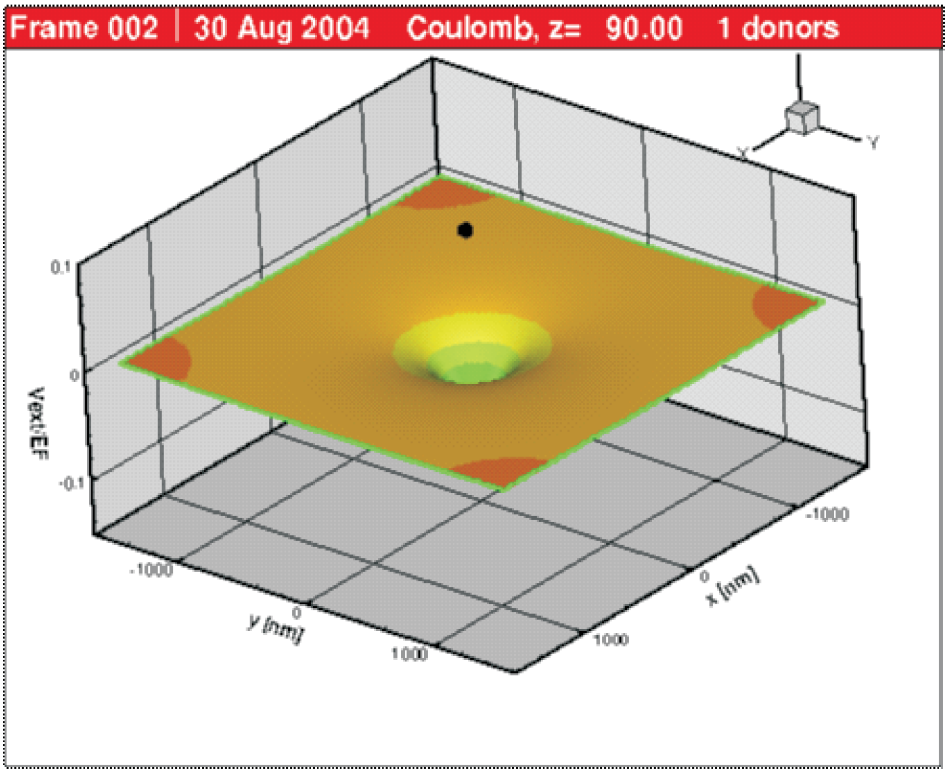

Figure 5.1: A single donor (black spot) located at the center of a $3\mu m \times 3\mu m$ unit cell 90nm above the electron gas ($z = 0$). The long-range behavior of the potential exhibits itself by the dark regions at the corners of the unit cell. Shown potential is screened by the dielectric media that lies between electron and donor layers.

5.2 Effective potential of ionized donors

5.2.1 Effect of spacer thickness

We start this section with a text book result: The electrostatic potential at $\mathbf{r}$, created by a single, positively charged particle placed at $\mathbf{r_j}$ is given by

$$V(\mathbf{r}) = \frac{\mathbf{1}}{\bar{\kappa}} \frac{\mathbf{e^2}}{|\mathbf{r} - \mathbf{r_j}|}. \tag{5.1}$$

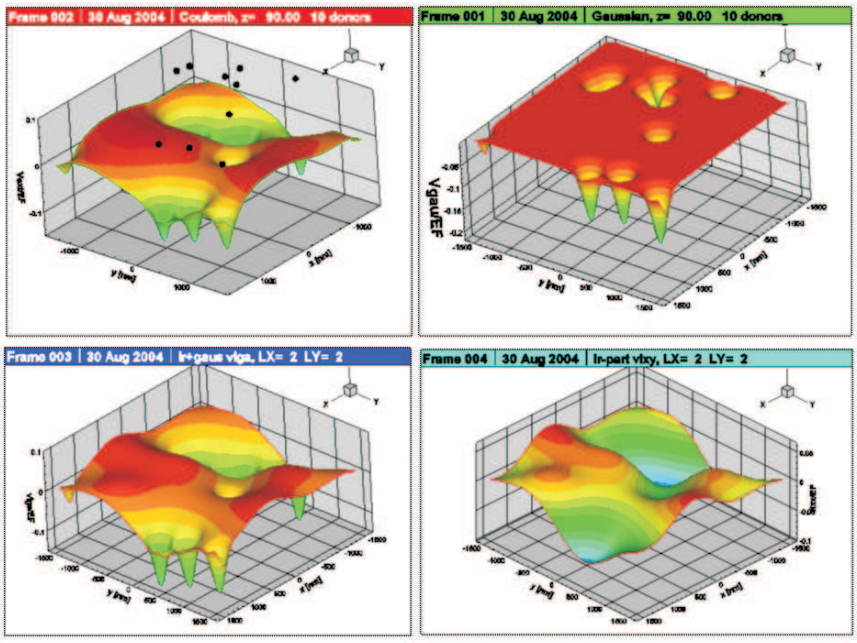

Figure 5.2: External potential generated 90nm below a plane containing ten [a] Coulombic [b] Gaussian donors. The range of the Gaussian potential is determined by the spacer thickness. [c] The LRP of the Coulomb potential profile, where only lowest two Fourier components are back-transformed to configuration space. [d] Gaussian potential profile plus the LRP of the Coulomb potential used in order to compare the potential landscape.

Such a potential is depicted in figure 5.1 for a unit cell of a square lattice with a relevant average dielectric constant $\bar{\kappa}$. The potential axis is scaled with the Fermi energy for 2DES of density $n_{el} \approx 3 \cdot 10^{11}\text{cm}^{-2}$ in GaAs ($\bar{\kappa} = 12.4$), $E_F \approx 10$ meV. An alternative scaling can be made by using the Rydberg energy (~ 5.9meV for GaAs), which is essentially at the same order of magnitude of the Fermi energy for a typical Hall sample. As the donor is at a finite distance from the plane where the electrostatic potential is calculated, no singularity is observed in the potential distribution. We should note that the electrostatic potential created by the donor(s) is screened by the dielectric material (with dielectric constant $\bar{\kappa}$) which is placed between the donor layer and the plane where we calculate the potential. The potential profile shows long-range parts, which are enhanced and lead to long-range fluctuations due to overlapping if several donors are considered within the unit cell (see. Fig. 5.2). The upper panel of Fig. 5.2 shows ten randomly distributed donors (black dots) in a plane and the electrostatic potential generated 90nm below this plane. Relatively long-range fluctuations due to the overlapping of the tails of the single donor potentials for the Coulombic donors can be observed. The right upper panel shows the

potential created by ten Gaussian potentials (see Eq. (4.11), with range $R = |z|/\sqrt{2}$) located at the projections of the donor positions onto the plane of the 2DES. The Gaussian donors are obtained by considering only the center part of the Coulombic donors and the long range part of the individual scatterers is neglected. It is clearly seen that, as the Gaussian potential is relatively short-ranged, there is essentially no overlapping of the single donor potentials, so that most of the $z = 0$ plane experiences a homogeneous potential. Although the impurity potential was approximated by Gaussian potentials in the previous chapter, it is clear that this assumption is not sufficient to recover the long-range-part (LRP) of the disorder potential. In order to overcome this difference the following procedure is applied: We perform a two-dimensional Fourier transformation of the Coulombic potential and make a back transformation keeping only the first two momentum components in each direction (right-bottom panel of Fig. 5.2), so that only the LRP of the potential is left. Then we add the LRP of the Coulomb potential to the potential created by the Gaussian donors. This is shown in left-lower panel of Fig. 5.2. The resulting potential, from the landscape point of view, looks very similar to the potential profile created by the Coulombic donors. We take this as a motivation to simulate the short-range parts of the donor potentials by Gaussians, and calculate from these Landau level broadening and conductivities as described in the previous chapter, and to simulate the long-range parts by long-range fluctuations added to the confining potential, as we describe in the following sections.

Next we discuss the effect of the spacer thickness on the impurity potential experienced in the plane of 2DES. It is well known from experimental and theoretical investigations that, if the distance between the electrons and donors is large, the mobility is relatively high and this high mobility is usually related with long-range fluctuations of the disorder potential. In Fig. 5.3 the external potential created by 120 donors, placed 90nm above the 2DES, is shown. The resulting potential shows considerable short-range fluctuations, with a variation amplitude $\sim E_F/2$ (without screening by the 2DES). If the distance between 2DES and the donors is increased to 120nm while keeping the donor distribution fixed, it is seen that the potential profile becomes smoother and the LRP of the fluctuations is pronounced, although the amplitude of the potential variation remains at the same order of magnitude. Increasing the spacer thickness further to 200nm, it is observed that the short-range fluctuations are almost lost and a slowly varying potential landscape is left. These results agree with the experimental observations of high mobility samples and are easy to understand from the z dependence of the Fourier expansion of the Coulomb potential,

$$\begin{aligned} V^{\vec{q}}(z) = & \int d\vec{r} e^{-i\vec{q}\cdot\vec{r}} \sum_j^N \frac{e^2/\bar{\kappa}}{\sqrt{(\vec{r}-\vec{r_j})^2+z^2}} \\ & = \frac{2\pi e^2}{\bar{\kappa} q} e^{-|qz|} N S(\vec{q}), \end{aligned} \tag{5.2}$$

where $S(\vec{q})$ contains all the information about the in-plane donor distribution and N is the total

number of the ionized donors. We observe that if the spacer thickness is increased, the amplitude of the potential decreases rapidly. We also see that the short-range potential fluctuations, which correspond to higher order Fourier components, are suppressed more efficiently. Before proceeding to the screening properties, it is useful to note that for low mobility samples the range of the potential fluctuations generated by the donors is at the order of a few hundred nanometers and the amplitude of the variation is around fifty percent of the Fermi energy. For high mobility samples on the other hand, the range of the fluctuations is at the order of a few micrometers and the amplitude of the variation is only twenty percent of the Fermi energy. Although these quantitative estimations are only valid for our specific number of donors and their distribution, in general they hold qualitatively. Thereby, we will consider the highly fluctuating confinement potential to be low mobility and the opposite to be high mobility, which then enables us to estimate mobility qualitatively by measuring the fluctuation (in fact modulation) amplitude.

5.2.2 Linear screening of the disorder potential

Here we discuss electronic screening of the external potential created by the donors discussed above. The Coulombic donors are distributed randomly on the $z = 120$nm plane and a two-dimensional Fourier transformation is performed to obtain the potential screened by the 2DES (see also Eq .(3.5) and related text) at zero temperature and magnetic field. In the left panel of Fig. 5.4 the external potential (reduced by the background dielectric material) generated by such donors is depicted. As it was discussed before, the amplitude of the variation is at the order of half of the Fermi energy and the range of the fluctuations is around $200 - 300$nm, which will be considered as low mobility later. The electronically screened potential is shown in the right panel of Fig. 5.4; the result is quite interesting as the LRP of the external potential is well screened but the short-range fluctuations is still distinguishable, although the amplitude of the variation is now around one percent of the Fermi energy. This can be well understood if one considers the dielectric function (Eq. 3.5), as q becomes smaller (i.e. for the LRP), $\epsilon(q)$ becomes larger resulting in a small amplitude within the linear screening regime. So one can conclude that the screening is more effective for the small$-q$ Fourier components, which corresponds to LRP of the external potential. Here we should emphasize the clear distinction between the effect of the spacer on the external potential and the screening by the 2DES, i.e. via $\epsilon(q)$. The former depends on the Fourier transform of the Coulomb potential and the important effect is the different decay of the different Fourier components (see Eq. 5.2), so that the short-range part of the disorder potential is well dampened, whereas the latter depends on the relevant DOS of the 2DES and the screening is more effective for the LRP. As a final remark, we would like to draw reader's attention to the short-range part of the "electronically" screened disorder potential shown in Fig. 5.4. We summarize our findings as follows: The spacer thickness reduces the

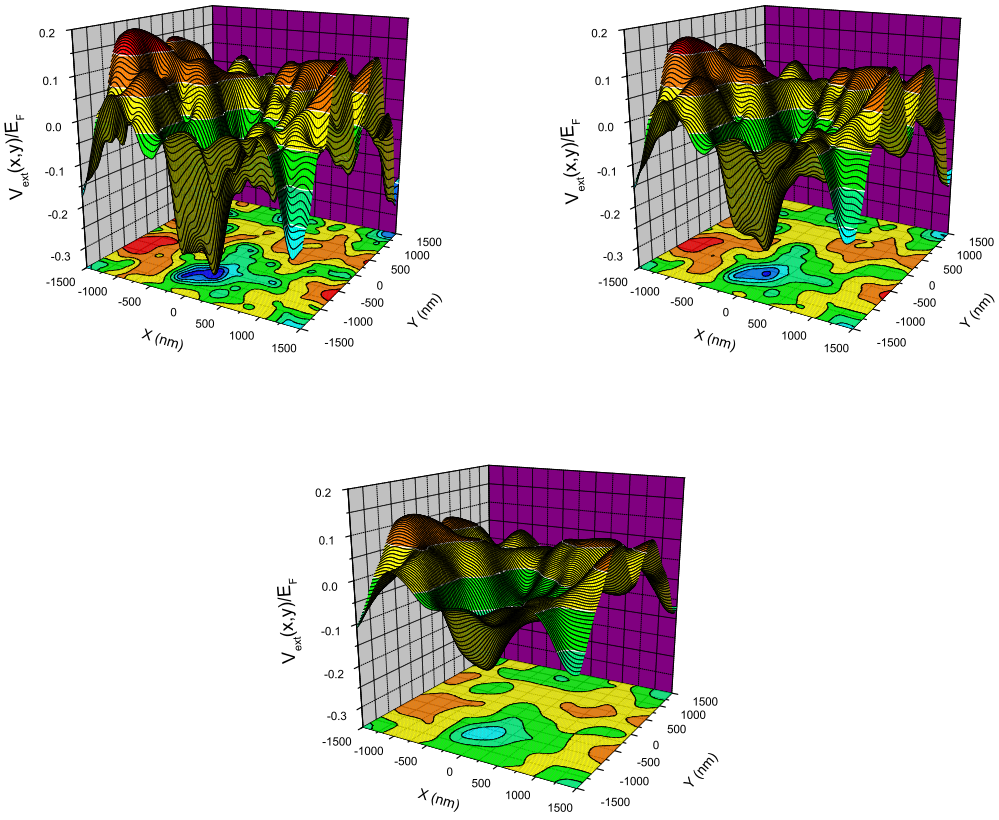

Figure 5.3: Electrostatic potential profile generated by the random distribution of 120 ions at $z = 90$nm (upper panel left), $z = 120$nm (upper panel right) and $z = 200$nm (lower panel). Similar to Fig. 5.2 damping is only due to the dielectric material in between 2DES and the donor layer.

amplitude of short-range fluctuations strongly, hence increases the mobility, whereas the long-range fluctuations are less affected. On the other hand 2DES screening affects strongly the long-range fluctuations, much less the short-range fluctuations, therefore it is reasonable to treat short-range and long-range fluctuations differently. The short-range part was included to our calculations via the SCBA in the previous chapter. In the next section we will discuss the long-range parts of the potential fluctuations by investigating the screening of the 2DES, which is magnetic field dependent.

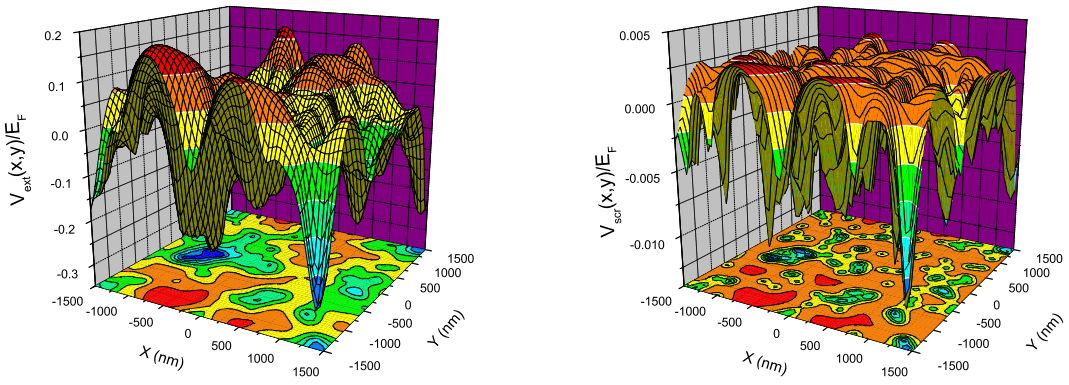

Figure 5.4: The external potential generated by random distribution of 90 ions, residing 120nm above the 2DES (left panel). Damping is only due to dielectric spacer. Screened potential by the 2DES at $T = 0$ and $B = 0$ for the given external potential, within the linear screening regime (right panel).

5.3 The effect of long-range fluctuations

In chapter 4 it was assumed that the impurities can be presented by Gaussian potentials (see also appendix B). The Landau level broadening and the transport coefficients were calculated analytically in a consistent manner within the SCBA. Thus, the short-range part of the disorder potential was included in our calculations implicitly, through the conductivity tensor and the collision broadening of the LL's, while LRP of the external potential was neglected. It was shown [74] that the SCBA is not sufficient to describe impurity scattering if the individual impurity potentials overlap. On the other hand in Fig. 5.2 we have seen that the LRP of the impurity potential exhibits different profiles for Coulombic and Gaussian ions. We simulate the long-range fluctuations generated by the inhomogeneous donor distribution by adding a harmonic modulation potential

$$V_{mod}(x) = V_0 \cos(2\pi m_p x/d) \quad , \quad 2m_p = \text{integer} + \frac{1}{2} \tag{5.3}$$

to the confining potential, where m_p is the modulation period that preserves the boundary conditions, i.e $V(-d) = V(d) = 0$. The electron densities, electrostatic potentials and the resistance curves are obtained by the scheme presented in chapter 4 for an in-plane Hall bar structure. The period and the amplitude of the modulation are selected according to our observations of Sec. 5.2. Before discussing the effect of this modulating potential on the Hall plateau widths, we recall that the effect of the disorder was discussed in Sec. 4.3.3 in the frame of collision broadening of the LLs. In Sec. 4.5, we concluded that the ISs shrink by increasing the disorder

strength and the widths of the plateaus become narrower. This observation is in contrast with the experimental results. To proceed, we first investigate the effect of the modulation potential on the density profiles. Results of self-consistent calculations are shown in Fig. 5.5. The color plot represents the density profiles (similar to Fig. 4.2) for narrow (upper half) and wide samples (lower half), with (right panel) and without (left panel) modulation, at fixed electron densities in each sample width. The modulation range is chosen to be $2\mu m$ in agreement with our previous observations in Sec. 5.2, so that the modulation period is $m_p = 1/4$ for the narrow sample and $m_p = 5/4$ for the wide sample. For the wide sample it is immediately seen that the center of the sample becomes incompressible at a higher B value for the modulated system compared to unmodulated ones, whereas for the narrow sample this shifting is less pronounced. This, of course, has an impact on the resistance curves as it was shown in chapter 4 that, the quantization of the Hall plateaus originates from the existence of the incompressible strips. The second remarkable qualitative difference at the density profiles between the narrow and the wide sample is the curvature profile and will be discussed in the next section. In Fig. 5.6 we show the Hall resistance curves calculated for the wide sample with several modulation amplitudes. The increase of the V_0 essentially means that the system becomes more disordered, which can be considered as a lowering the mobility of the sample ($V_0/E_F > 0.1$). It can be observed that the Hall plateau becomes wider with increasing the amplitude of the modulation potential, which is in a good qualitative agreement with the experimental findings. So that the QH plateaus of the low-mobility samples are wider, compared to the high-mobility ones.

Another well known feature of the Hall resistance is that, the high-temperature curve crosses the Hall plateau usually close to the center. Here we define the magnetic field value at which the high-temperature Hall resistance curve crosses the low-temperature one as B^{cr}. In Fig. 4.10 it is seen that, for the *clean* (unmodulated) sample the Drude and the high-temperature curves cross the low-temperature Hall resistance close to the high-magnetic field edge of the plateau ($\widetilde{B}^{cr} \sim 0.94$). In Fig. 5.6, the Hall plateau becomes wider, at the high-magnetic field edge since the modulation potential creates ISs at a higher B. Note that the Drude result only depends on the average electron density, for a fixed sample width, depletion length and magnetic field, and is not affected by the modulation. Thus B^{cr} is not changed, but as the plateau becomes wider the Drude result and the low-temperature Hall resistance now coincide closer to the center of the plateau, which becomes also consistent with the experiments.

As a summary, we have obtained a qualitative agreement with the experiments by a simple treatment of the LRP of the potential fluctuations. Of course, one needs a detailed investigation of the disorder potential in order to obtain a quantitative understanding of the mobility and the screening of the impurity potential.

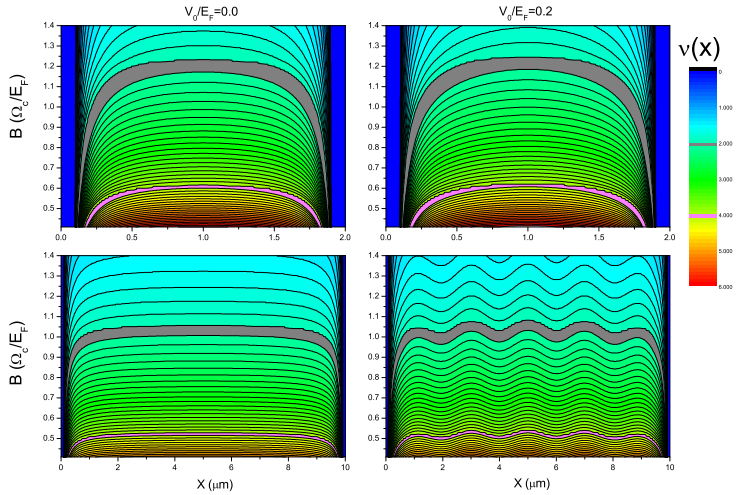

Figure 5.5: Local filling factors (color scale plot) versus position and cyclotron energy ($\Omega_c \equiv \hbar\omega_c$) for a clean (left panel) and a disordered (right panel) sample calculated at a relatively low temperature ($k_BT/E_F = 0.02$) considering a narrow (upper panel, with $2d = 2\mu m$) and a wide (lower panel, with $2d = 10\mu$m) electron channel. The depletion length is fixed as 100nm. Gray region indicates the ISs with $\nu(x) = 2$ and pink region indicates $\nu(x) = 4$. The average electron densities are $2.88 \cdot 10^{11}\text{cm}^{-2}$ and $3.69 \cdot 10^{11}\text{cm}^{-2}$, for the narrow and wide samples, respectively. The disordered samples are modulated slightly ($V_0/E_F = 0.2$). The range of the modulation potential is set to be $2\mu m$.

5.4 Sample width dependencies of the high-temperature line

In this section we implement our theory to four different samples and make qualitative predictions on the high-temperature crossings of the Hall plateaus. Here we consider two sample widths, a narrow $2\mu m$ and a wide $10\mu m$ sample, with fixed depletion lengths. In Fig. 5.7 we show a schematic drawing of the sample geometries for the mentioned widths, together with electron density profiles for zero magnetic field at zero temperature. The prominent difference between these two density profiles is their curvature at the bulk. For the wide sample the bulk density profile is nearly flat, whereas for the narrow sample a bending profile is observed. From our numerical calculations it is seen that the center electron density of the wide sample is very close to the average density, i.e $n_{el}(5\mu m) = 1.04 \times \bar{n}_{el} = n_{el}^{max}$ and, whereas, for the narrow sample the density deviates at the center from its average density by $\%16$. These sample width dependent curvature profiles have an impact on the Hall resistance curves, as these affect the existence of the ISs. In figure 5.8 the Hall resistances are plotted against the magnetic field,

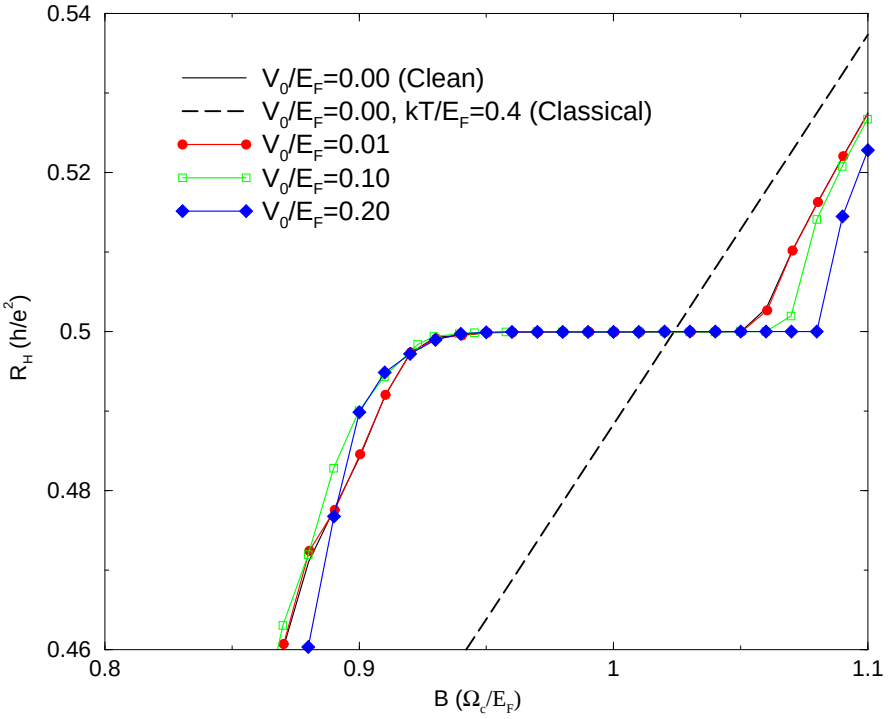

Figure 5.6: The Hall resistances for various modulation strengths at $k_BT/E_F = 0.02$, together with the high-temperature limit, where the average electron density is set to, $\bar{n}_{el} = 3.69 \cdot 10^{11}\text{cm}^{-2}$ corresponding to $E_F = 13.20$ meV. Averaging is performed over 50nm and depletion length is fixed to 100nm.

calculated for the narrow and wide clean samples at low and high temperatures. It is observed that the resistances obtained at high temperature cross the low temperature ones in a different manner. For the wide sample the crossing occurs at the high-field edge ($\Omega_c/E_F^0 \sim 0.98$), whereas for the narrow sample they coincide closer to the low-field edge ($\Omega_c/E_F^0 \sim 0.94$). This difference can be explained by reexamining the Drude result of the Hall resistance (Eq. 4.15) given in chapter 4. The crossing value B^{cr} is obtained by equating R_H to the quantized value,

$$R_H^D = \frac{b}{d}\frac{E_F^0}{E_F}\frac{\hbar\omega_c^{cr}}{E_F^0} = 1 \tag{5.4}$$

then, with the given parameters, the crossing occurs at high-field edge of the Hall plateau for the wide sample and closer to the low-field edge for the narrow sample for a fixed depletion length.

Finally, Fig. 5.9 shows the effect of the modulation on the QH plateaus at low and high temperatures. As it was discussed, the perturbation has no effect on the Drude result and the modulation widens the QH plateaus, hence R_H^D crosses the plateaus closer to the center. For the narrow sample B^{cr} is insensitive to the mobility and for the wide sample it approaches to the

center from right edge. We summarize our findings as follows: If we consider high mobility (clean) samples, B^{cr} is at the high-field edge, for the wide sample and is at the low-field edge for narrow sample. By introducing disorder to the system the QH plateaus become wider, so that the crossing occurs relatively closer to the center for wide sample and is similar to the clean one for the narrow sample.

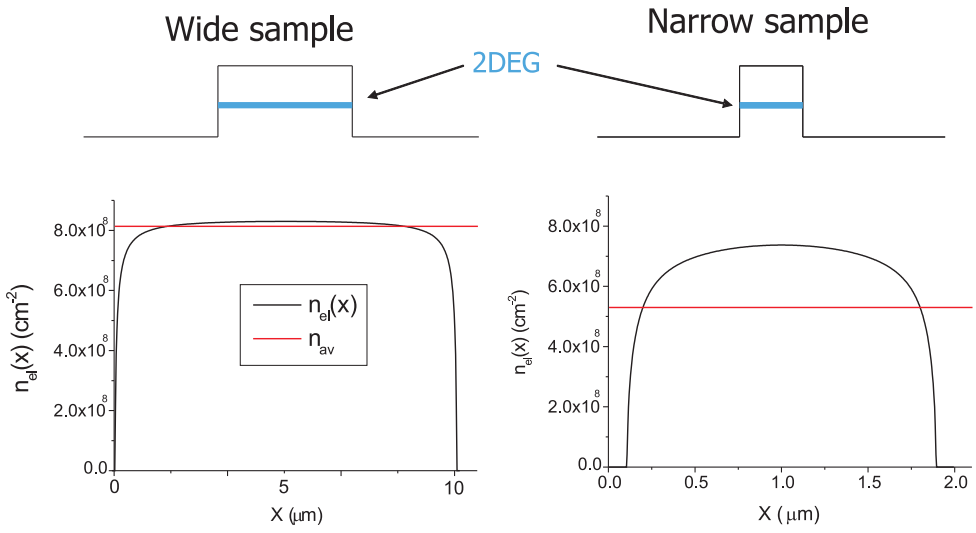

Figure 5.7: An illustration of the samples depending on the widths and the electron densities obtained at zero field and temperature. The no electron region (depletion length=$d - b$) is set to be 100nm, with average donor density $n_0 = 4 \cdot 10^{11}\text{cm}^{-2}$, resulting in the average electron densities $n_{el} = 2.88 \cdot 10^{11}\text{cm}^{-2}$ for the narrow sample and $n_{el} = 3.69 \cdot 10^{11}\text{cm}^{-2}$ for the wide sample.

5.5 Summary

In this chapter we have investigated the impurity potential generated by an inhomogeneous distribution of the remote donors. We compared the overall potential profiles created by *Coulombic* donors to the *Gaussian* ones. We concluded that, due to overlapping of the single donor potentials, the Coulombic ions generate long-range fluctuations, however, the Gaussian donors do not. By adding two lowest Fourier components of the Coulombic potential to the Gaussian one, we regenerated these fluctuations. Based on this observation we added a perturbing harmonic modulation potential to the confining potential of the translation invariant model, so that the discrepancies in plateau widths and crossing points addressed in Sec. 4.5 were resolved. Moreover, treating the modulation amplitude as a measure of the disorder, we compared the Hall plateau widths of the high and low mobility samples. We observed that the plateaus be-

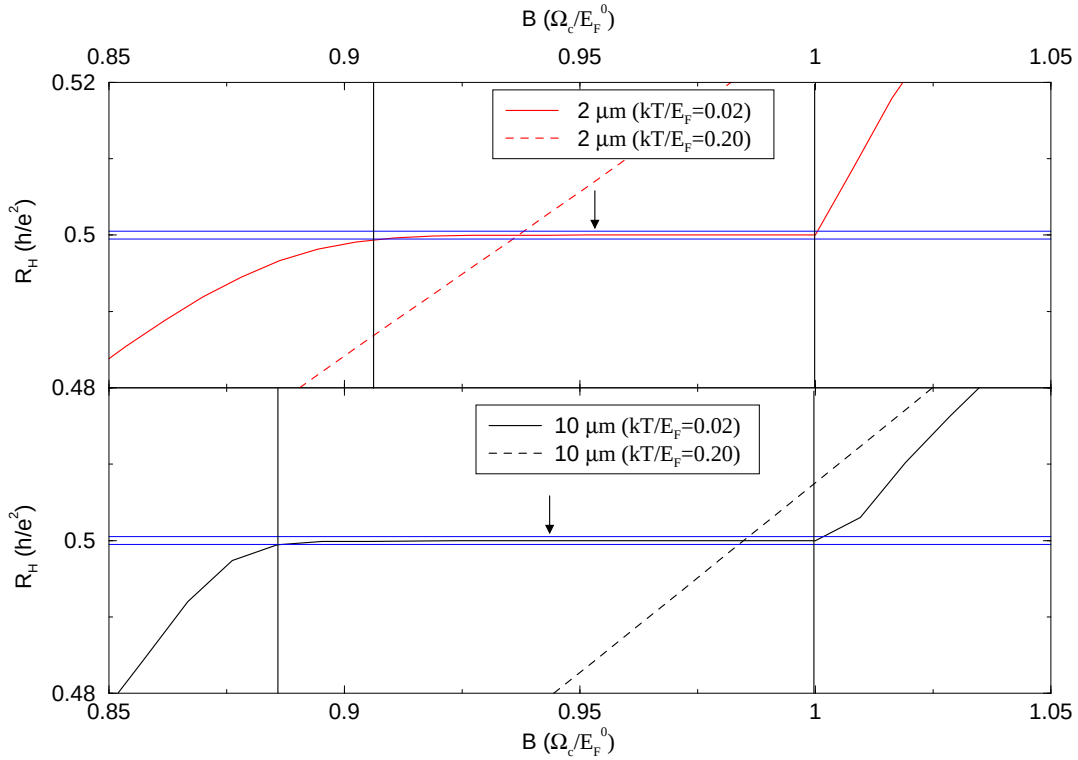

Figure 5.8: The Hall resistances for clean samples at low ($k_BT/E_F = 0.02$,solid lines) and high ($k_BT/E_F = 0.2$, dashed lines) temperatures, for $2d = 2\mu$m (upper panel) and $2d = 10\mu$m (lower panel), with $\lambda = 50$nm. The horizontal lines ($h/2e^2 \pm 0.005$) are used to define the plateau width. The 2DES is in the plateau regime in the interval bounded by vertical lines and the arrows indicate the center of the plateau. Other parameters are given in the figure caption 5.7

come wider with increasing modulation strength, i.e. by decreasing the mobility of the sample. Here we also examined the crossing of the Drude resistance with the low-temperature Hall resistance considering two sample widths and two mobilities. We predict that for a high mobility ($\mu > 2.0 \times 10^6 cm^2/Vs$) wide ($d = 5\mu m$) sample the crossing occurs at the high-magnetic-field edge of the Hall plateau, whereas it happens close to the center for a low mobility ($\mu < 0.5 \times 10^6 cm^2/Vs$). For the $2\mu m$ high mobility (clean) sample the crossing is seen on the lower-magnetic-field edge of the plateau, independently of the mobility. The above predictions can easily be tested by standard quantum Hall experiments.

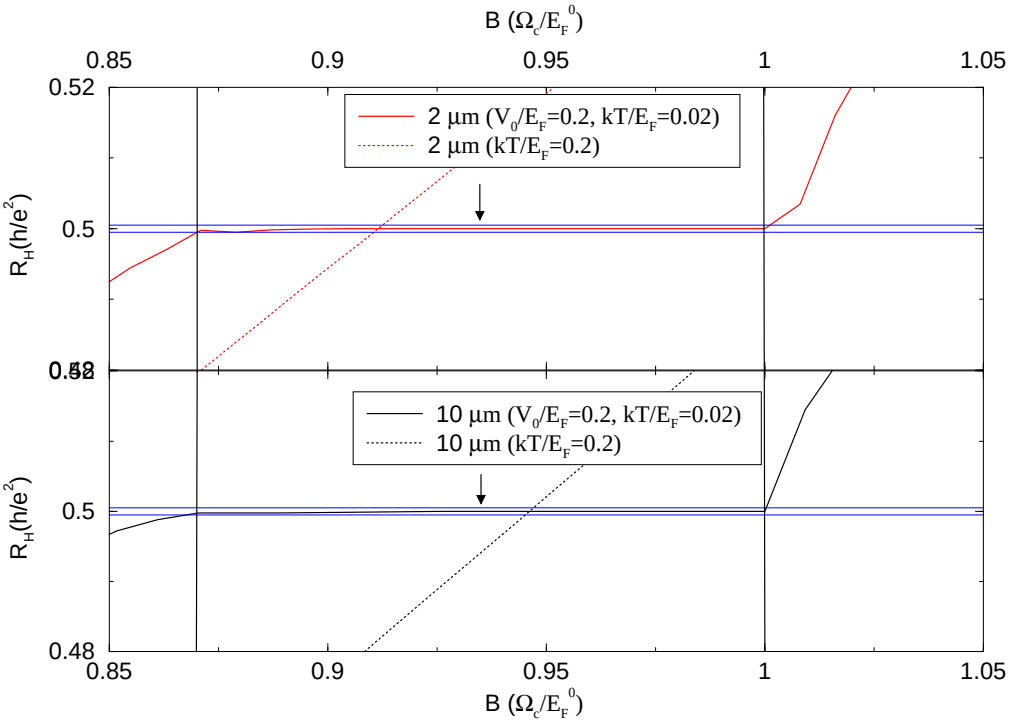

Figure 5.9: The Hall resistances for modulated ($V_0/E_F = 0.2$) samples at low ($k_BT/E_F = 0.02$) and high ($k_BT/E_F = 0.2$) temperatures, for two sample widths, with $\lambda = 50$nm. The vertical and the horizontal lines are the same as Fig.5.8 as well as the arrows. Other parameters are given in the figure caption 5.7

Chapter 6

Screening properties of electron-electron bilayers: Measurement and Calculations

6.1 Introduction

In this chapter we apply the scheme presented in the previous chapters to an electron-electron bilayer system. For this model system, we can investigate both self-consistent screening and magneto-transport properties within the linear response regime under QH conditions. We show that the existence of the incompressible regions in one of the layers, affects the other layer density profile strongly by creating potential fluctuations. We observe that these potential fluctuations modify the magneto-transport quantities. Here we also present some of the experimental findings [75] that exhibit hysteresis at the magneto-resistance curves, for mismatched densities, where one of the layers is in the QH plateau regime. Motivated by the long relaxation time [57] to thermodynamic equilibrium within the plateau regime, we simulate two magnetic sweep directions by introducing two effective screened potential profiles and compare our numerical results with the experimental ones considered in Sec. 6.5.

The organization of this chapter is as follows: first the bilayer geometry and fixed external potentials acting on the electron layers are introduced. Then we discuss the electron density and electrostatic potential profiles of the system, which are obtained within the self-consistent Thomas-Fermi-Poisson approach introduced in chapter 2. Second, we systematically investigate the dependence of both the electrostatic and transport properties on the density mismatch. Here, we use the scheme presented in chapter 4 to calculate the Hall and the longitudinal resistances. We examine the effects of the incompressible strips from the point of external potential fluctuations based on the arguments given in chapter 5. There we observed that a perturbing external potential may shift, widen and/or stabilize the QH plateaus. In Sec.6.5 we shortly discuss the sample and the experimental setup, and also show the measured resistance curves. Finally a model is proposed in Sec. 6.6 to explore the basic mechanism underlying the magneto-transport

hysteresis.

6.2 The Model

In a typical electron bilayer sample, a silicon doped thick $(AlGa)As$ layer is grown on top of a $GaAs$ substrate. This is followed by the bottom $GaAs$ quantum well, separated from the top 2DES by an un-doped $AlGaAs$ spacer. On top of the upper 2DES again a silicon doped $(AlGa)As$ layer is grown, which is capped by a $GaAs$ layer. So that two 2DES are placed in a close proximity, which are confined by remote donors and the sample is capped by top and/or bottom gates that controls the electron density of each layer. In related experiments both gates are used to tune the electron densities from top and bottom layers, whereas the gate potential profile depends on the sample geometry and the applied gate bias. The electrons are symmetrically (with respect to the growth direction) confined by $AlGaAs$ layers each of which contains a plain with Si doping ($\delta-$ doping), and are separated by a spacer of thickness ($h \sim 10-30nm$). For such a separation thickness the bilayer system is then known to be electronically decoupled and in non-equilibrium, i.e. can be represented by two different electrochemical potentials. Electron tunneling between the layers is not possible.

In Fig. 6.1 a schematic drawing of a mesa etched bilayer system is shown, which consists of two 2DESs (minus signs), two donor layers (plus signs) and a top gate (gray area). We model the bilayer system such that the bottom 2DES lies on the $z = 0$ plane with a number density $n^B_{\rm el}(x)$ in the interval $-d < x < d$, where $2d$ is the width of the sample and the top layer is in the plane $z = h$, with the electron density $n^T_{\rm el}(x)$. Relevant to the considered experiments, we assume that the donors (or equivalently the background charges) are symmetrically separated from the electron layers placed at $z = -c$ and $z = c+h$, for bottom and top layers respectively, having a constant surface density $n^T_0 = n^B_0 = n_0$. Here we also assume translation invariance in the y direction. The electron density of the top 2DES is governed by the top gate, located at $z = c + h + f = z_g$ and the electron channels are formed in the interval $|x| \leq b$. As it was introduced in chapter 2 one obtains the total electrostatic potential of an electron on the line (x, z) due to a line-charge at (x_0, z_0) from Eqs.(2.1)-(2.2) with the kernel (see Sec.3.3.1 and also Eq.A.9),

$$K(x, x_0, z, z_0) = -\ln\left(\frac{\cos^2\frac{\pi}{4d}(x + x_0) + \gamma^2}{\sin^2\frac{\pi}{4d}(x - x_0) + \gamma^2}\right) \tag{6.1}$$

where the $z-$ dependence is given by $\gamma = \sinh(\pi|z - z_0|/4d)$. The confining (background) potential is obtained by inserting a constant number density (n_0) of the background charges into Eq. (2.2). It is assumed that the gate can be described by an induced charge distribution $n_g(x)$,

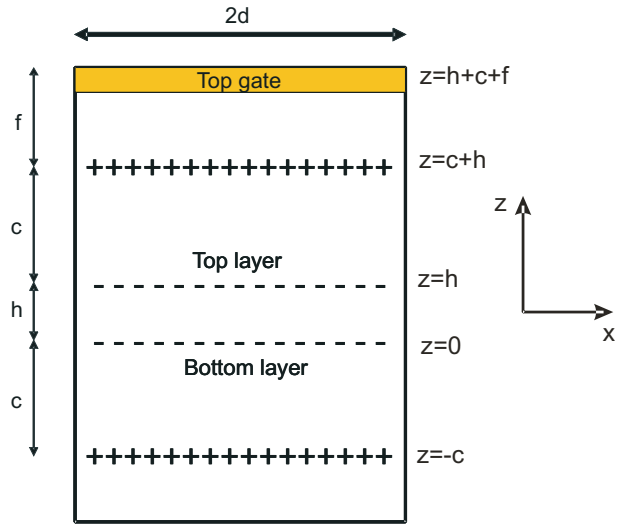

Figure 6.1: The cross-section of the bilayer geometry. Sample is capped by a gate from top in order to change the electron density of the top-layer. Top (bottom) 2DES lies below (above) the top (bottom) layer donors at a distance, c. Electron layers are separated from each other by a dielectric spacer having thickness, h.

residing on the plane z_g. Then, from Eq.(2.2) the gate potential can be written as

$$V_g(x,z) = \frac{2e^2}{\bar{\kappa}} \int_{-d}^{d} dx_0 K(x, x_0, z, z_g) n_{\rm g}(x_0). \tag{6.2}$$

In order to obtain a flat (gate) potential profile at the bulk we choose the induced charge distribution as

$$n_g(x) = n_g^0 \cosh(\frac{5}{8\pi}(x/d)), \tag{6.3}$$

where n_g^0 determines the strength of the gate potential. In Fig. 6.2 the distribution of the positive charges and the potential profile is shown. One can add more electrons to the top layer by setting $V_0 = n_g^0/n_0$ to a positive value and keeping the depletion length $d-b$ fixed. With such treatment of the gate, the average electron densities are changed while the depletion length is kept constant. Similarly the Hartree potential is calculated from Eq.(2.2) for the top layer as

$$V_H^T(x,z) = \frac{2e^2}{\bar{\kappa}} \int_{-d}^{d} dx_0 K(x, x_0, z, z_0 = h) n_{\rm el}^T(x_0)$$

and for the bottom layer

$$V_H^B(x,z) = \frac{2e^2}{\bar{\kappa}} \int_{-d}^{d} dx_0 K(x, x_0, z, z_0 = 0) n_{\rm el}^B(x_0).$$

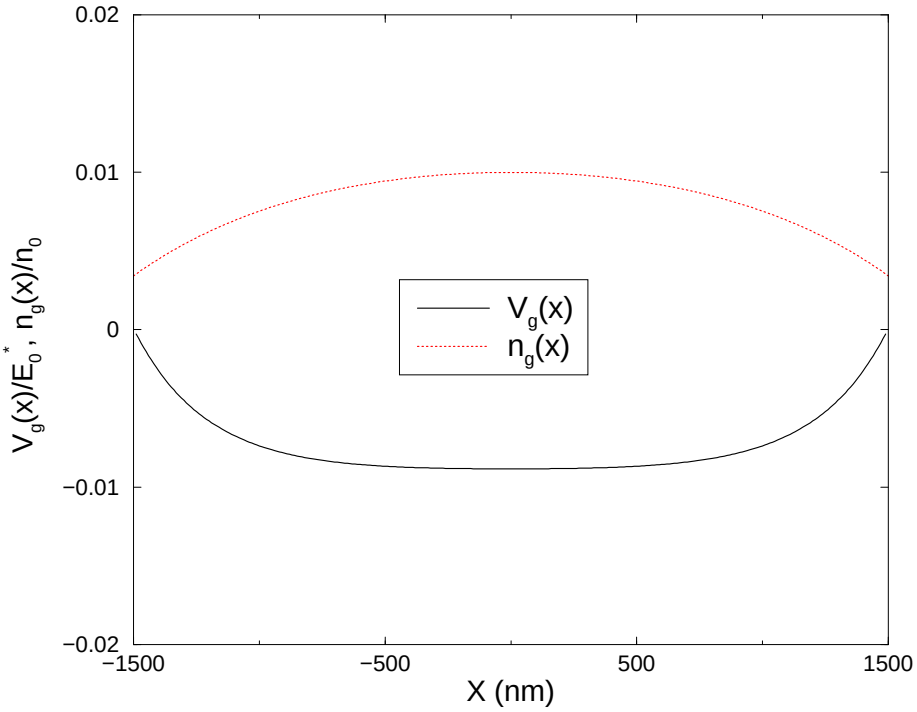

Figure 6.2: The gate potential profile (solid-line) at $z = h$, together with the generating positive charge distribution (dotted-line) against position. The additional charges residing on the gate lead to a stronger confining potential in the top layer, resulting in a higher average density. The donor density is $n_0 = 4 \cdot 10^{11} cm^{-2}$ and the gate potential strength is taken to be $V_0/E_0^* = 0.01$, where E_0^* is the pinch-off energy defined in Eq. 3.26. For other parameters see the related text.

Then Eq.(2.1) can be rewritten as

$$V(x,z) = -V_{bg}^{T}(x,z) - V_{bg}^{B}(x,z) - V_g(x,z) + V_H^{T}(x,z) + V_H^{B}(x,z). \tag{6.4}$$

In the next step the electron densities are calculated within the TFA (Eq. 2.8) similar to the single layer situation as

$$n_{el}^{T,B}(x) = \int dE D(E) f([E + V(x, z_{T,B}) - \mu_{T,B}^*]/k_B T) \tag{6.5}$$

where $\mu_{T,B}^*$ is the chemical potential and $z_{T,B}$ the position of top and bottom layer, respectively. In our numerical calculations, we start with zero temperature and magnetic field and initially obtain the confining potential created by its own donors for each layer. Then, we obtain the electron densities and the Hartree potentials of both layers as described in Sec. 2.1.2 just as in the case of a single layer. Knowing the electron distribution of the top (bottom) layer via Eqs.(2.8) and (2.2) we calculate the potential acting on the bottom (top) layer similar to the

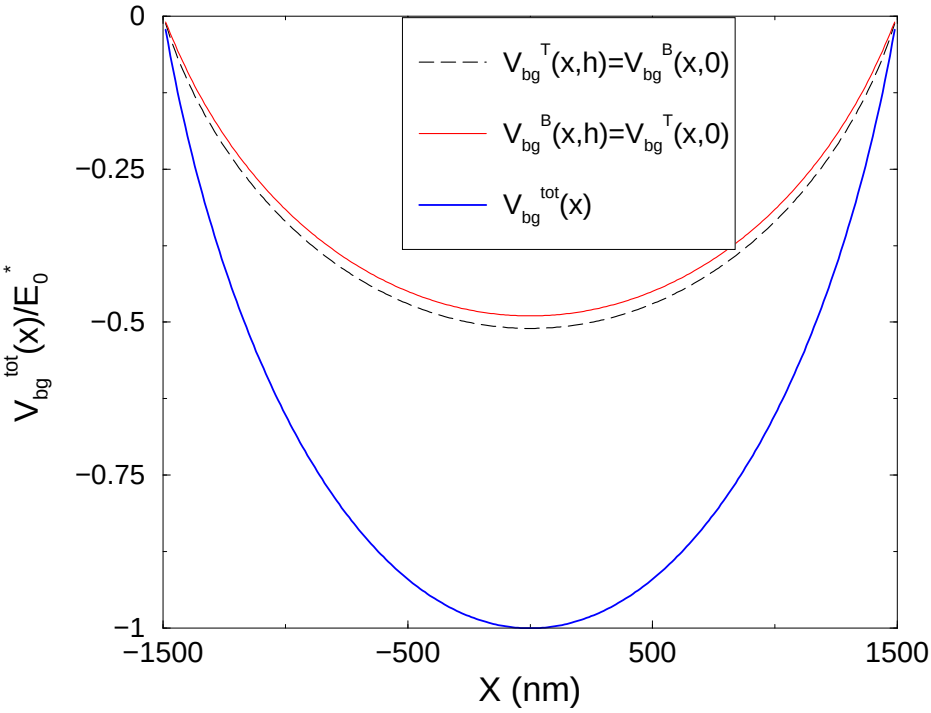

Figure 6.3: Total background potential created by the top and bottom layer donors (thick solid-line). The potential contributions to the bottom 2DES $(z = 0)$ come from top donor layer ($V_{bg}^{T}(x, 0)$, thin solid line) and from bottom donor layer ($V_{bg}^{B}(x, 0)$, dashed line). Numerical calculations are performed for GaAs heterostructure with the parameters $h = 15nm$ and $c = 60nm$. The numbers of donors are fixed to $4 \times 10^{11} cm^{-2}$ per layer, for a sample width $2d = 3000nm$, corresponding to an average pinch-off energy ($E_0^* \sim 2300$ meV).

single layer case. So that the total electrostatic potential of an electron at the top layer is

$$\begin{aligned} V^T(x) = \quad & V_{ext}(x, z = h) + V_H^B(x, z = h) \\ & + V_H^T(x, z = h), \end{aligned} \tag{6.6}$$

where the total fixed external potential acting on the layers is $V_{ext}(x, z) = V_{bg}^{tot}(x, z) + V_g(x, z)$ and we denote the total background potential by $V_{bg}^{tot}(x, z) = V_{bg}^{T}(x, z) + V_{bg}^{B}(x, z)$ (see Fig.6.3). Note that the first two terms in Eq. (6.6), are considered to be external and the last term is the intra-layer Hartree potential. Similarly for the bottom layer the total electrostatic potential is

$$\begin{aligned} V^B(x) = \quad & V_{ext}(x, z = 0) + V_H^T(x, z = 0) \\ & + V_H^B(x, z = 0). \end{aligned} \tag{6.7}$$

In each iteration step an accurate numerical convergency is achieved for a single layer, then the Hartree potential is added to the other layers external potential. Intra-layer self-consistencies

are obtained by Newton-Raphson iteration and inter-layer self-consistency is obtained by direct iteration. One can then use this solution as an initial value and obtain the density and screened potential for finite magnetic field and temperature. We scale energies by the average Fermi energy E_F^* $(= (E_F^T + E_F^B)/2)$, e.g. $\hbar\omega_c/E_F^* = \Omega_c/E_F^*$, and the lengths by the screening length a_0. The electron density and the electrostatic potential can be calculated self-consistently by the above scheme within the TFA.

6.3 Screening results

In this section we present our results calculated within the self-consistent scheme, starting by discussing the zero temperature, zero magnetic field limit and then compare the obtained density profiles with the finite temperature and field profiles. The aim of this investigation is to clarify the effect of the quantizing perpendicular magnetic field, which introduces local charge imbalances due to formation of the incompressible strips. We have already seen that the electron density distribution is highly sensitive to the applied external magnetic and electric fields. Therefore even very small changes in these external parameters affect the density and potential profiles drastically.

It is shown in chapter 3 that the formation of the compressible and incompressible strips results in an inhomogeneous density distribution that deviates from the zero field profile. This deviation creates a local charge imbalance generating a potential fluctuation. Here we start our analysis by discussing the effect of the local charge deviation from its equilibrium distribution at $T = 0\,, B = 0$. Figure 6.4 depicts the electron densities calculated within the SCTFPA for vanishing and finite magnetic field and temperature, where we used 300 mesh points to span a single layer. The typical parameters used in the calculations are: $d = 1500nm$, $c = 60nm$, $h = 15nm$, $f = 90nm$, $n_0 = 4 \times 10^{11} cm^{-2}$ and $\bar{n}_{el}^T = \bar{n}_{el}^B = 3.30 \times 10^{11} cm^{-2}$, for $V_0/E_0 = 0$. A positive (with respect to the electrons) potential bias is applied to the top gate (for details check Eq.(6.3) and related text) so that more electrons are populated to the top layer resulting in a density mismatch. The curves for finite field and temperature show a considerable deviation from the curves for zero field and temperature in the intervals $(800nm < |x| < 1000nm)$, where one observes incompressible strips at the top layer. In the inset we concentrate on this interval. In Fig. 6.4 we compare the $T = 0, B = 0$ density curves to the $T \neq 0, B \neq 0$ ones. In the interval $-900 < x \lesssim -600$ there are less electrons at the top layer due to the formation of an incompressible strip. This yields a less repulsive inter-layer Coulomb interaction. So that more electrons are populated locally at the bottom layer. Similar arguments hold for the left-hand side of the incompressible strip $(-1200 \lesssim x < -900)$ but now the potential becomes more repulsive thus more electrons are depleted from the bottom layer locally.

At very strong magnetic fields $(\nu(0) < 2)$ only the lowest Landau level is partially occupied,

which yields a high DOS, thus the density profiles of $B = 0$ and $B > 0$ should look very similar. However, for lower B there is a difference due to the quantizing magnetic field, that creates a dipolar (incompressible) strip at the top layer, which has an influence on the bottom layer via the strong Coulomb interaction. Therefore, it is essential to examine the formation of the incompressible strips at strong magnetic fields. This is done by manipulating the interlayer electron distances applying a finite gate bias. The gate controls the existence and positions of the incompressible strips indirectly, so that one can examine the screening effects of the incompressible strips considering the electron density distributions. In the later sections, potential fluctuations created by these local charge imbalances, i.e. the incompressible strips, will be connected to the magneto-transport quantities, where we explicitly show the impact of the incompressible strips on the Hall resistances.

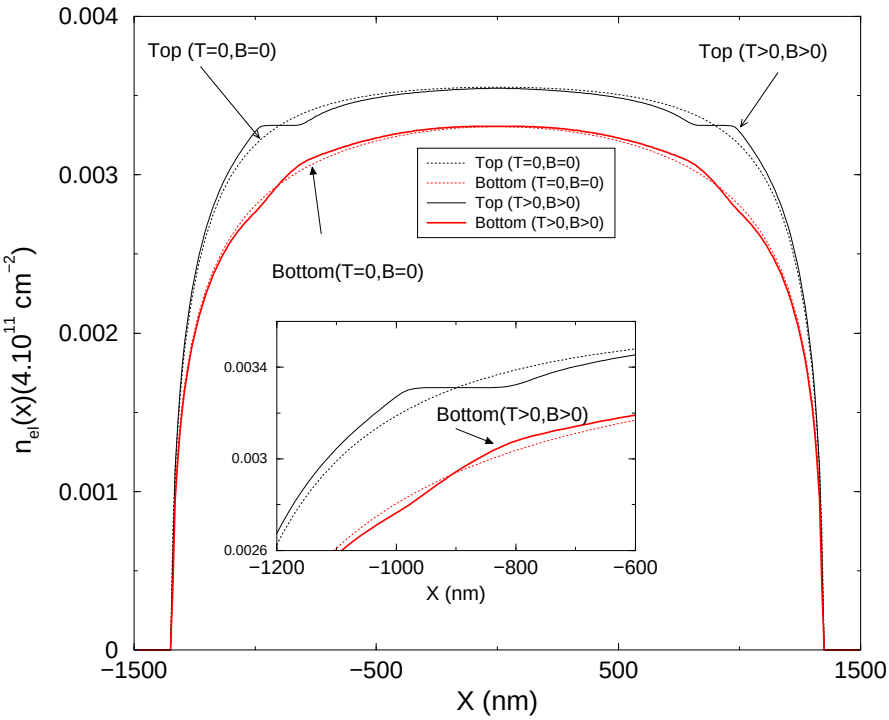

Figure 6.4: Electron densities for a finite magnetic field (such that, $\bar{\nu}_{av}^{tot} = 2$) and at default temperature ($kT/E_F^* \sim 0.01$), for top (indicated by arrows) and bottom (thin solid-line) layers. Also for vanishing field and temperature (dotted lines). The depletion length is set to be $150nm$ and the density mismatch is governed by applying a finite gate potential $V_0/E_0^* = 0.03$, resulting in $\bar{n}_{el}^T = 3.50\times10^{11}cm^{-2}$ and $\bar{n}_{el}^B = 3.27\times10^{11}cm^{-2}$. The inset shows the region where an incompressible strip exists at the top layer.

6.3.1 Density mismatch

It is well known that the mutual Coulomb interaction is a strong long-range interaction, thus a change in the charge distribution, compared to the equilibrium distribution (at $T = 0\,, B = 0$), produces a considerable effect on the observable quantities even at large length scales. In the previous section it is shown that such a local charge imbalance is created due to formation of the incompressible strips. Here we investigate the density distributions of the layers by applying a positive gate voltage, hence populating the top 2DES. The average total filling factor, $\bar{\nu}_{av}^{tot} = (\nu^T + \nu^B)/2$, is kept constant and the evolution of the incompressible strip at the bottom layer, and its effect to the top layer, is examined. Figure 6.5 presents position dependent filling factors for such a positively charged gate, resulting in different density mismatches by applying a gate bias voltage V_0. For a slight mismatch one does not observe a prominent change, except more electrons are populated to the top layer at the center, thus the bulk of the bottom layer becomes flatter. This feature is more pronounced at a higher gate bias and, in turn, the bottom layer is forced to be incompressible at the bulk, leading the effective external potential to be more confining for the top layer. The outer edge regions of incompressible strips residing at the top layer suppress the electrons beneath, at the bottom layer. Increasing the density mismatch in favor of the top layer, it is observed that more electrons start to accumulate at the bulk of the top layer and small density fluctuations can be seen at the bottom layer. We close our short discussion by noting that, even a small amount of density mismatch can lead to a drastic change in the density profiles. Moreover this change is enhanced by the existence of the incompressible strip, which results from the non linear screening in the presence of external magnetic field. This high sensitivity to the external electric field is clearly seen, if the potential profiles are considered and exhibits interesting features at the resistance curves. Here we shall emphasize, that a wide incompressible strip formed at the bulk of one of the layers does not necessarily imply that this layer becomes completely transparent to its donors, since the electrons residing in the incompressible strip create an electric field which can still partially cancel the electric field generated by its donors.

6.3.2 Potential fluctuations

In this section we examine the effects of the incompressible strips in one layer on the external potential profile of the other layer by comparing what we call "interacting" and "non-interacting" systems. In both cases we start with the self-consistent calculation of the density and potential profiles at $T = 0, B = 0$. Then we focus on one layer, bottom or top, which we call the "active" layer while the other layer is called the "passive" one. Now we keep the $T = 0, B = 0$ density and Hartree potential profile of the passive layer fixed and calculate in the corresponding, $B-$ independent external potential of the active layer its density and poten-

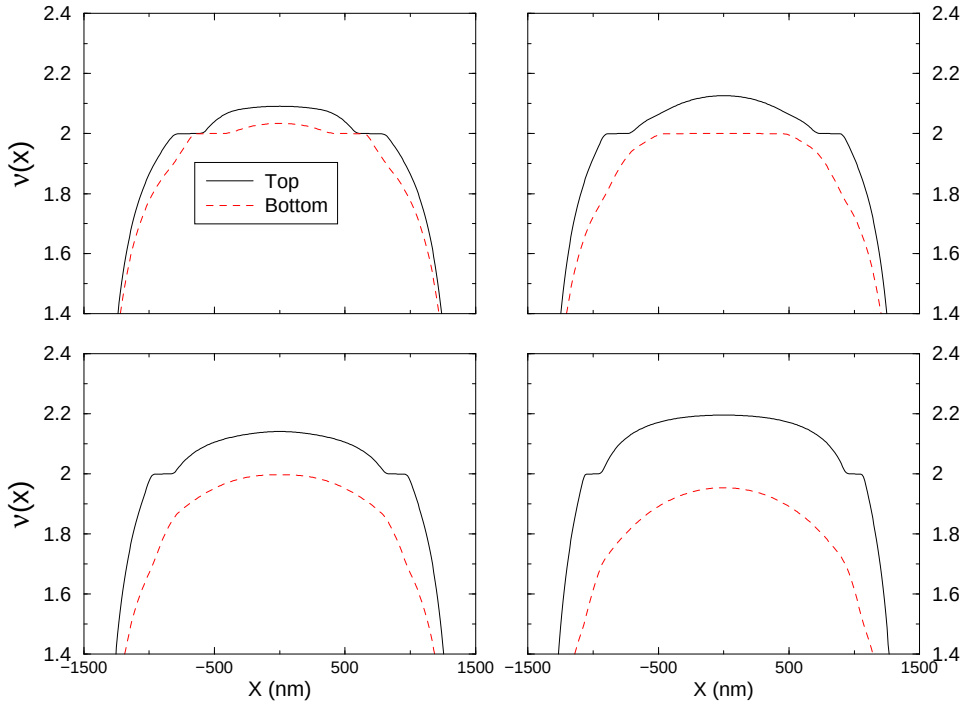

Figure 6.5: The top layer is populated by applying a finite gate potential V_0/E_0^* [a] 0.01, [b] 0.02, [c] 0.03, [d] 0.05 corresponding to density mismatches of $\bar{n}_{el}^B/\bar{n}_{el}^T = 0.967, 0.936, 0.905, 0.846$, respectively. Given at default temperature, with the depletion length, $b/d = 0.9$ and the total average filling factor is fixed to two.

tial profile self-consistently at finite T and B. This yields the total potential $V_N(x,z)$ of the non-interacting system. It takes into account the $B-$ dependent intra-layer screening properties in the active layer, but not the $B-$ dependent changes of the intra-layer screening in the passive layer and of the inter-layer screening. Finally we drop the restriction on the passive layer and calculate density and potential profiles for both layers at finite T and B fully self-consistently. This yields the total potential $V_I(x,z)$ of the interacting system.
The potential variation

$$\Delta V(x) = V_I(x,z) - V_N(x,z), \tag{6.8}$$

taken at the $z-$ value of the active layer, describes the $B-$ dependent change of the interaction of the active with the passive layer. It is suitable for studying the effect of the incompressible strips in the passive layer on the effective potential in the active layer. Fig. 6.6 shows potential variation and filling factors across the sample at four different magnetic field values where the superscript $T(B)$ indicates that the top (bottom) layer is the active layer. In Fig. 6.6a the magnetic field strength is chosen such that both layers are compressible, i.e. the center filling

factors of both layers are slightly below two. The potential variation shows a characteristic behavior as the layers are both compressible all over the sample, screening is nearly perfect, and a very small potential fluctuation ($\leq 1\% E_F^*$) is observed within the electron channel. A relatively large variation is seen within the depletion regions, which does not contribute to screening. The reason for this is that, at finite temperature the density profiles leak out at the edges, whereas in the bulk they deviate very little from their zero field distributions. If one decreases the magnetic field strength and obtains a wide incompressible strip in the bulk of the top layer (Fig. 6.6b), a large potential variation is observed at this layer. The variation drastically increases and becomes almost $\sim \ \%40 E_F^*$. Meanwhile, the variation of the bottom layer does not show any significant change. The explanation of these observations is twofold; first as an incompressible strip is formed at the top layer, the finite field density profile strongly deviates from the zero field profile, which essentially creates a huge local (within the incompressible strip) external potential fluctuation to the bottom layer. Second, the bottom layer is completely compressible, so that this large potential fluctuation can be screened by redistribution of the bottom layer electrons, resulting in a density deviation from the zero field profile. Note that as a consequence of the self-consistency the deviation is spread all over the bottom layer, which also generates an external potential fluctuation to the top layer. Here, as we examine how the top layer responds to this external potential fluctuation, we remind the reader that there are two different regions with different screening properties: (i) The compressible regions show similar features to the bottom layer and the external potential fluctuation is well screened, (ii) The incompressible region at the bulk can poorly screen the fluctuation and one observes that $\Delta V(x)/E_F^*$ can be large as half the Fermi energy.

At this point it is useful to summarize stepwise:

Step (1): The incompressible strip in the bulk of the top layer generates a strong potential fluctuation to the bottom layer, due to its large deviation from the zero field distribution.

Step (2): As the bottom layer is completely compressible, the potential fluctuation generated in step (1) is screened by redistribution of its electrons, generating an almost homogeneous potential variation to the top layer.

Step (3): The potential fluctuation generated in step (2) is well screened within the compressible regions and a small potential fluctuation is observed.

Step (4): The potential fluctuation generated in step (2) is poorly screened within the incompressible region, hence a large potential fluctuation is observed.

In Fig. 6.6c, the magnetic field strength is slightly decreased in order to obtain a wide incompressible strip at the bottom layer, meanwhile the wide incompressible strip of the top layer splits into two ribbons which are shifted towards the edges. For this B value, one observes similar effects as for the previous case, but this time for both of the layers. Following our stepwise explanations we conclude that, as both layer's density distributions deviate from their zero field

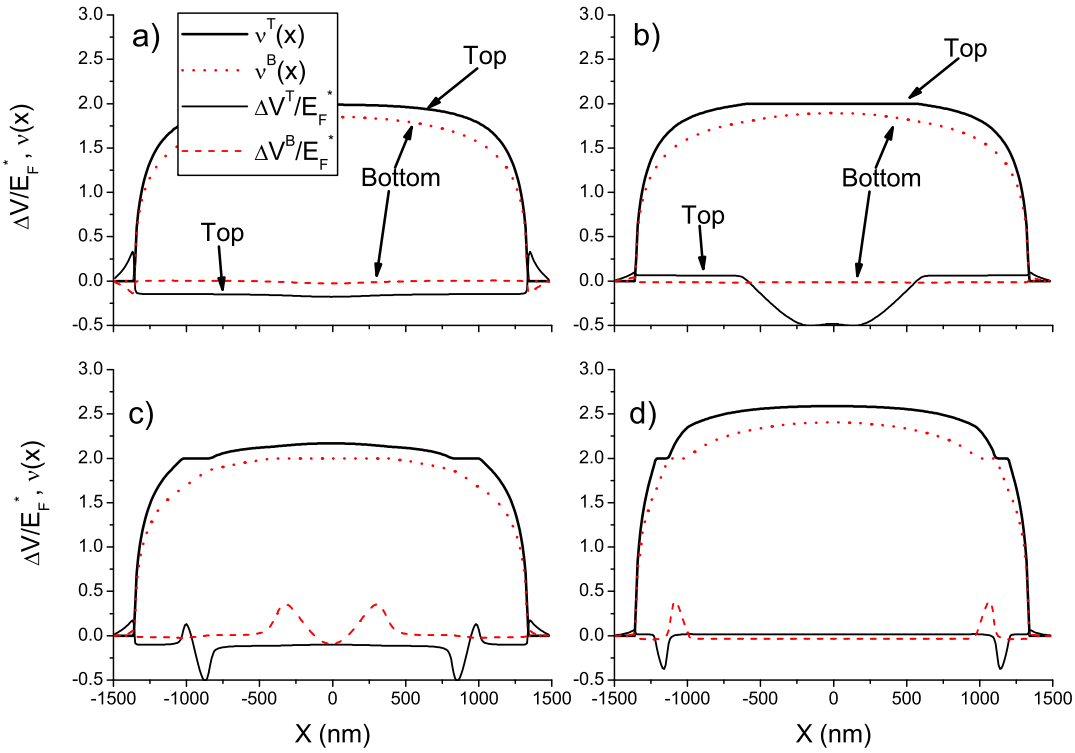

Figure 6.6: Position dependent filling factors and magnetic field induced potential variations, for four characteristic magnetic field values. The variations are multiplied by 10 in [a] and 5 in [c], [d]. The gate potential is set to $V_0/E_0^* = 0.03$, for default temperature and depletion.

profiles, an external potential fluctuation is generated, which can be screened perfectly within the compressible regions, but poorly at the incompressible strip. Since there are two incompressible strips at the top layer, the potential fluctuates in two separated intervals. On the other hand there is only one incompressible strip at the bottom layer the variation is observed at a single interval. Figure 6.6d shows the case, where two well developed incompressible strips are present at both of the layers and the potential fluctuations are confined to these regions. We should emphasize that the variation amplitude depends on the width of the incompressible strip which generates the fluctuation, since the charge imbalance becomes larger if the incompressible strip is wide.

The potential fluctuations discussed above play an important role when one considers a fixed external current flowing through both of the layers. These fluctuations are generated by local charge imbalances, with respect to zero field density distributions, and can be observed in the

interval where the other layer has an incompressible strip as they are poorly screened.

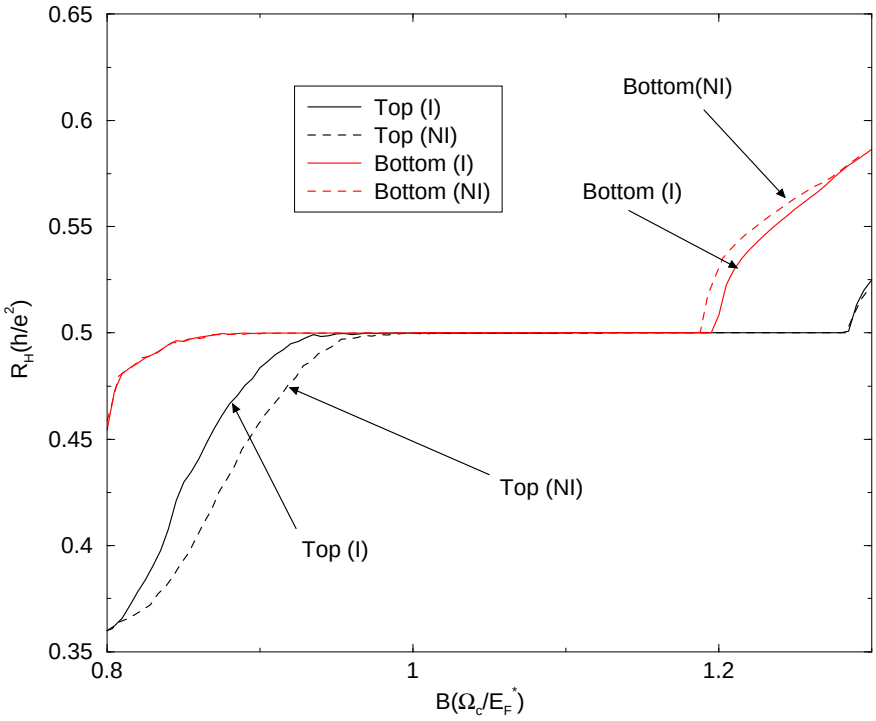

Figure 6.7: Comparison of the interacting (solid-lines) and non-interacting (dashed-lines) Hall resistance curves for fixed electron densities at default temperature. The Hall resistance curve is shifted for the top layer as the potential fluctuation created by the bottom layers incompressible strip.

6.4 The Hall resistance curves

In this section we investigate the effects of potential fluctuations on the Hall resistances using the findings of chapter 4 within the linear response regime. We consider these fluctuations in the frame of chapter 5, where we concluded that the (long-range) potential fluctuations can widen, stabilize and shift the quantized Hall (QH) plateaus as they affect the position and the existence of the incompressible strips. Here we use the general expressions derived in chapter 4, for a given electron density and fixed current, to calculate the Hall and longitudinal resistances, from Eqs.(4.7), of the bilayer system. We also note that the averaging procedure of the conductivities is carried over a length scale (λ_{av}), which is comparable with the Fermi wavelength and, in particular is set to be $40nm$ in our calculations. We apply these results to two cases considered in Sec. 6.3.2, namely the interacting and non-interacting systems. We remind that, in

the case of non-interacting system, the active layer does not have information about the density inhomogeneities caused by the incompressible strips of the passive layer. Hence comparing the resistance curves of these two cases essentially gives a method to extract the effect of the incompressible strips on the other layer.

In order to investigate the relation between the incompressible strips of the passive layer and the magneto-transport coefficients of the active layer qualitatively, we calculate the Hall resistances for a magnetic field interval, where QH plateaus are observed for both layers around filling factor two. A harmonic density modulation is added to the background charge distribution in order to simulate the long-range fluctuations of the confining potential similar to Sec. 5.3. It is assumed that the spatial distribution of the donors is given by

$$n_d(x) = n_0\big(1 - \delta\cos(5\pi x/2d)\big) \tag{6.9}$$

with $\delta = 0.01$, i.e. the donor distribution fluctuates $\%1$ around its average value, n_0, locally. In Fig. 6.7 we show the Hall resistances (in units of the von Klitzing constant) *vs.* magnetic field for interacting (solid-lines) and non-interacting (dashed lines) systems. We start the discussion with the high-magnetic field regime, which essentially corresponds to a density distribution similar to that shown in Fig. 6.6a. As there are no incompressible strips within both layers, no noticeable potential fluctuations are created due to local charge imbalance, therefore the Hall resistances of both layers are the same for interacting and non-interacting cases. If we examine the QH regime of the top layer, it is seen that at least one incompressible strip is formed (cf. Fig. 6.6b), creating a potential fluctuation in the bottom layer. Meanwhile, the bottom layer is still compressible all over the sample, so the fluctuation can be screened nearly perfect, leading to a very small change in the R_H curves, due to finite temperature. The situation is different if incompressible strips are formed at both of the layers (corresponding to Fig. 6.6c and Fig. 6.6d). Now both layers produce fluctuations due to local charge imbalance and for this B interval the fluctuation can not be screened perfectly everywhere, which should result in a difference in the Hall resistance curves. This is observed for the top layer at the high-magnetic field edge, since the perturbation shifts the maximum magnetic field value of the QH plateau, from $\Omega_c/E_F^* \sim 1.18$ to $\Omega_c/E_F^* \sim 1.21$. Since the quantized value of the Hall resistance only depends on the presence of the incompressible strip, the case for the bottom layer is quite different as it is already in the plateau regime. Although the potential fluctuation is created by the top layer and is not screened perfectly, this perturbation changes only the position or the width of the incompressible strip, but not the value of the R_H within the plateau regime. Eventually it depends on the amplitude of the perturbation, i.e. if the amplitude is large enough to destroy the incompressible strips one does not observe the quantized value for R_H. The change in R_H can be observed for the bottom layer at somewhat smaller values of the magnetic field strength ($0.92 \lesssim \Omega_c/E_F^* \lesssim 0.97$) as the perturbation now stabilizes the plateau. In fact the fluctuation widens the incompressible strips, with respect to the non-interacting case and

creates incompressible strips larger than the averaging length, λ_{av}. Finally one ends with a wider plateau. The difference in the Hall resistance curves between the interacting and non-interacting systems, tends to disappear as the incompressible strips become narrower and move towards the edges by decreasing the magnetic field. This is consistent with the previous observation, that the amplitude of the fluctuation depends on the width of the incompressible region.

In summary four magnetic field intervals are observed: (i) both layers are compressible and there exists no difference for the R_H curves as calculated for the interacting and non-interacting case, (ii) bottom layer has an incompressible strip and creates a fluctuation, which shifts for the top layer the edge of the Hall plateau to higher magnetic field values, (iii) both layers show incompressible regions, the perturbation generated by the top layer widens the incompressible strips of the bottom layer, leading to a wider plateau, (*iv*) the incompressible strips of both layers become narrower and move towards the edges and the fluctuation becomes inefficient, hence the difference is smeared out. It is useful to mention that the *interacting* system is an *equilibrium* solution, in the sense that the electrons of both layers rearrange their distribution until a full convergence is obtained (within a numerical accuracy), for a given external potential profile. In view of the following discussion of experiment, we want to recall some facts about our equilibrium calculations. It is clear that there is no preferable sweeping direction of the magnetic field as we do not include time dependency in our calculations. Also one can not expect a memory effect, since the initial values considered in the calculations are independent of each other, i.e. in each magnetic field value one starts with $T = 0$, $B = 0$, then calculates the screened potential for a given magnetic field and temperature, thus the information of the density distribution is not carried to the next magnetic field value. These equilibrium results will become comparable with the experimental findings if the system reaches thermodynamic equilibrium in each magnetic field value while sweeping. On the other hand it is well known that a hysteresis-like behavior is a non-equilibrium effect, which in fact can not be calculated within the prescription described above. This difficulty will be overcome in Sec. 6.6 where we propose a scheme to simulate the non-equilibrium.

6.5 The Experiments

Here we report on the magneto-transport hysteresis observed in the bilayer systems measured at the *Max-Planck Institut-Stuttgart* by S. Kraus [75]. In the experiments discussed here, the magneto-resistances are measured as a function of the applied perpendicular magnetic field. The sweep direction dependence is investigated for matched and mismatch densities. For our particular interest, measurements were also performed with the same set of samples, where the system was heated up to ~ 10K and cooled down again at each magnetic sweep step, in the magnetic field interval where hysteresis is observed. Similar findings have already been pre-

sented in the literature [53, 54], however, have been discussed in a different theoretical content and the "equilibrium" case was not studied.

The samples are $GaAs/AlGaAs$ double quantum well structures grown by molecular beam epitaxy (MBE). Separate Ohmic contacts to the two layers are realized by a selective depletion technique [76]. A technique developed by Rubel *et al.* [77] was used to fabricate backgates. The metal gate on top of the sample acts as frontgate. The samples were processed into 80μm wide and 880μm long Hall bars. The high mobility samples are grown at the *Walter-Schottky Institut*. They have as grown densities in the range $1.5 - 2.5 \times 10^{11}$cm^{-2} and mobility is 100 m^2/Vs per layer. The barrier thickness is 12nm and the quantum wells are 15nm wide. The experiments were performed at low-temperatures ($T \sim 270$mK) and the imposed current is always in the linear response regime ($I \sim 50$nA). Other details of the experimental setup and samples could be found in an upcoming publication [75].

We show the measured Hall (Fig. 6.8 upper panel) and longitudinal (Fig. 6.8 lower panel) resistances of the top layer (solid lines) as a function of magnetic field strength for an interval where the bottom layer (dotted lines) is within the QH regime. The equilibrium curves (solid lines with symbols) are obtained as follows: at each B value, the base temperature is increased up to a sufficiently high value and then cooled down again, so that any possible "memory effect" due to thermodynamic non-equilibrium is eliminated. We observe that in this limit the system is insensitive to the sweep direction, since the up sweep values coincide with the down sweep values (black solid lines with filled circles) as expected. In accord with our numerical results (previous section) obtained for the "interacting" system, the measured quantities are independent of their history. We claim that the measured equilibrium resistances are the analogues of the calculated resistances for the interacting system. In the same figure, we also show the measured magneto-resistances for matched densities (green solid lines). We see that the equilibrium plateau is wider than that of the matched case (this is most clearly seen for the longitudinal resistances). This is an unexpected observation since it is believed that the plateau widths should be the same for the same electron densities with same mobilities, since the density of the active layer is the same in matched and mismatched cases. We proceed our investigation with the density mismatched and non-equilibrium case. The data were taken at a sweep rate $0.01T/min$ and the base temperature is always kept at 270mK. Apparently it is seen that the resistances of the top layer follow different traces depending on whether the sweep is in up (red solid lines) or down (black solid lines) direction. The resistances at low magnetic field interval ($B \lesssim 6.75T$) do not show a prominent difference for two sweep directions. The plateau regime is extended up to $B \sim 7.25T$ for down sweep and ends at $B \sim 6.8T$ for up sweep, meanwhile the bottom layer is also in the QH regime. It is easy to understand why the QH regime is wider for the down sweep considering the widths of the incompressible strips as follows: while coming form high magnetic field to low fields we **first** encounter with a wide incompressible region

(see for example Fig.4.7b) that generates a large potential fluctuation (c.f. Fig.6.6b) yielding a wide plateau. However, for the other sweep direction two narrow incompressible strips are observed **first**, which creates relatively weak fluctuations, that have a negligible effect on the plateau width. Of course, the word **first** has an importance if a time sequence is considered, this discussion is left to the next section. It is worthwhile to note that both up sweep and equilibrium plateau regimes coincide up to same magnetic field strength ($B \approx 6.8T$).

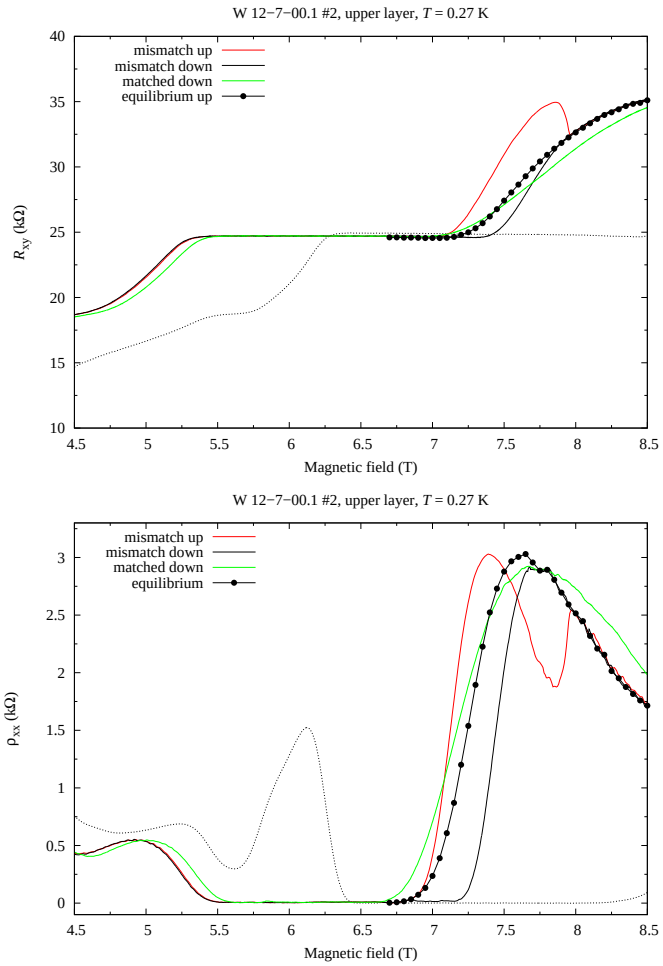

Figure 6.8: Measured Hall (upper panel) and longitudinal (lower panel) resistances for the top (solid lines) and bottom (dotted lines) layer at a base temperature of 270mK. Hysteresis is not observed for the matched-density (green solid line) and the equilibrium (solid line with circles)

In Fig.6.9 measured longitudinal resistances of both layers are shown for two sweep directions. We see that the sweep direction has no effect on the resistances at high magnetic fields ($B \gtrsim 8T$). The first exiting feature is observed when the bottom layer is in the plateau regime and the top layer is approaching to its plateau regime (yellow shaded region). It is seen that the

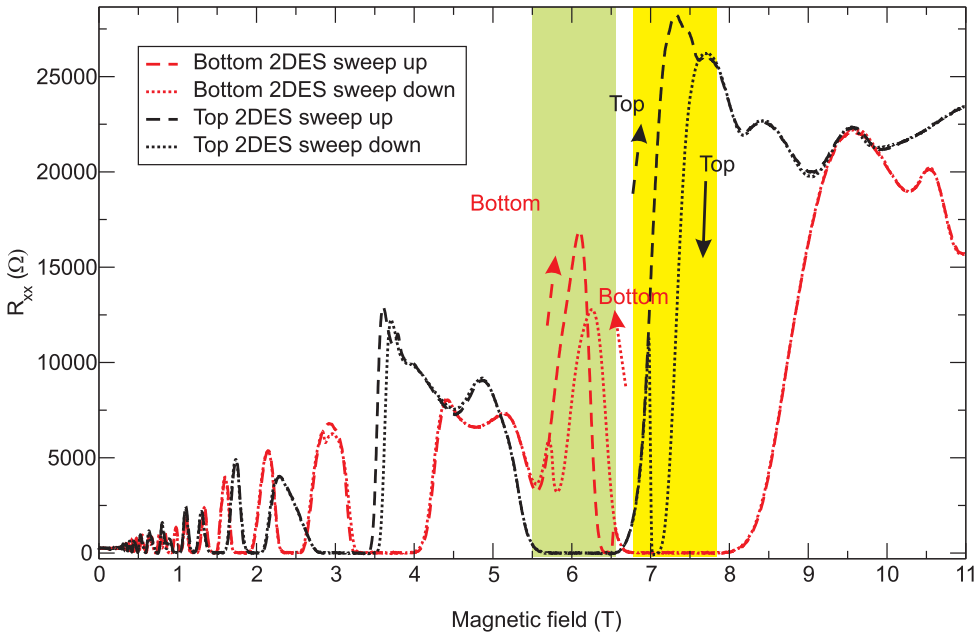

Figure 6.9: The longitudinal resistances as a function of magnetic field for a GaAs electron bilayer system with a barrier width 12nm, considering two sweep directions. Data is taken at a magnetic sweep rate 0.01T/min. A strong hysteresis develops in ρ_{xx} when the other layer is in a plateau. No significant effect is observed at low field regime.

longitudinal resistance of the top layer follows two different traces depending on the sweeping direction, meanwhile the bottom layers resistance is insensitive and assumes the zero value. For smaller values of the magnetic field, we observe at the top layer that up and down sweep curves follow the same trace and fall to zero at $B \sim 6.8T$. A similar hysteresis behavior is seen at the bottom layer resistance curves (green shaded region), now the top layer is in the plateau regime for both sweeping directions. A less pronounced repetition of these features are observed at the $\nu = 2$ plateau regimes, e.g. $3.4T \lesssim B \lesssim 3.6T$ and $2.9T \lesssim B \lesssim 3.2T$. A common feature (also observed at different density mismatches) is that the hysteresis is seen at the active layer only if the passive layer is in the plateau regime. No hysteresis is observed if the QH regimes of the layers coincide (see discussion above for the matched densities).

We summarize the experimental observations as follows: (i) the equilibrium plateaus are wider than the ones of the matched densities, (ii) the hysteresis is observed in the active layer only if the passive layer is in the plateau regime.

The first observation can be interpreted by using the analogy between interacting⇔equilibrium and noninteracting⇔matched-density cases. We have already mentioned that the "interacting" system is an equilibrium solution and it is easy to grasp the similarity between the "equilibrium"

measurements. On the other hand, in the "non-interacting" case the passive layer is unaffected by the potential fluctuations generated by local density imbalances at the active layer. In the experiments, for matched densities, we would expect that both layers will have the same density profiles, therefore the incompressible strips will reside in the same x intervals at both layers and, as a consequence the potential fluctuations will not be as efficient as they are for the *offset* case. By offset we mean that the incompressible strips of the layers are not placed on top of each other. Hence, we can conclude that for the matched densities, the macroscopic quantities (e.g. resistance curves) will be effected very little by the incompressible strips of the other layer, although microscopic quantities (such as local densities) will still be sensitive to the potential fluctuations. Thus, from the effect of the potential fluctuation (generated by the incompressible strips) point of view we claim that the "non-interacting" system is the analog of the matched-density case. Therefore we attribute the widening of the top layer's plateau to the potential fluctuations created by the bottom layer, as already shown for the "interacting" case in Fig. 6.7. The observations of the non-equilibrium measurements (ii) require an explanation that can cover the hysteresis, which is proposed in the next section.

6.6 Simulation of non-equilibrium

This section is devoted to build a model, that allows us to explore the underlying mechanism of the hysteresis-like effect observed in the experiments [53, 54] and the ones considered in Sec. 6.5. Our model is based on the following arguments: First, it is shown both experimentally [22] and theoretically [65] that there exists at least one wide incompressible strip ($> \lambda_{av}$) within the QH regime (also cf. chapter 4, in particular Fig. 4.9), second this incompressible strip creates an external potential fluctuation to the other layer, as it is shown in Sec. 6.3.2 (see Fig.6.6) and third, the relaxation time to the thermodynamic equilibrium is much larger than the magnetic sweep-time within the QH regime, as the existing incompressible strips impose thermodynamic boundary conditions to the 2DESs [57]. The thermodynamic boundary conditions are imposed as follows: changing the magnetic field shifts the incompressible strips so that more electrons are redistributed across the incompressible strips, where no states exist at the Fermi level. So that it becomes nearly impossible for the 2DES to reach the thermodynamic equilibrium at $k_B T \ll E_F$, which results in a long relaxation time. In other words, in the QH plateau regime the non-equilibrium is caused by the incompressible strips, which lead the system to "remember" the density distribution of the previous magnetic field value(s), so that one should take into account the sweeping direction, as the 2DES can not redistribute its electrons due to the formation of incompressible strips.

A weak modulation potential (see Eq.6.9) is added to the confinement potentials of both layers in order to simulate the long-range-part of the impurity potentials as it was done in the

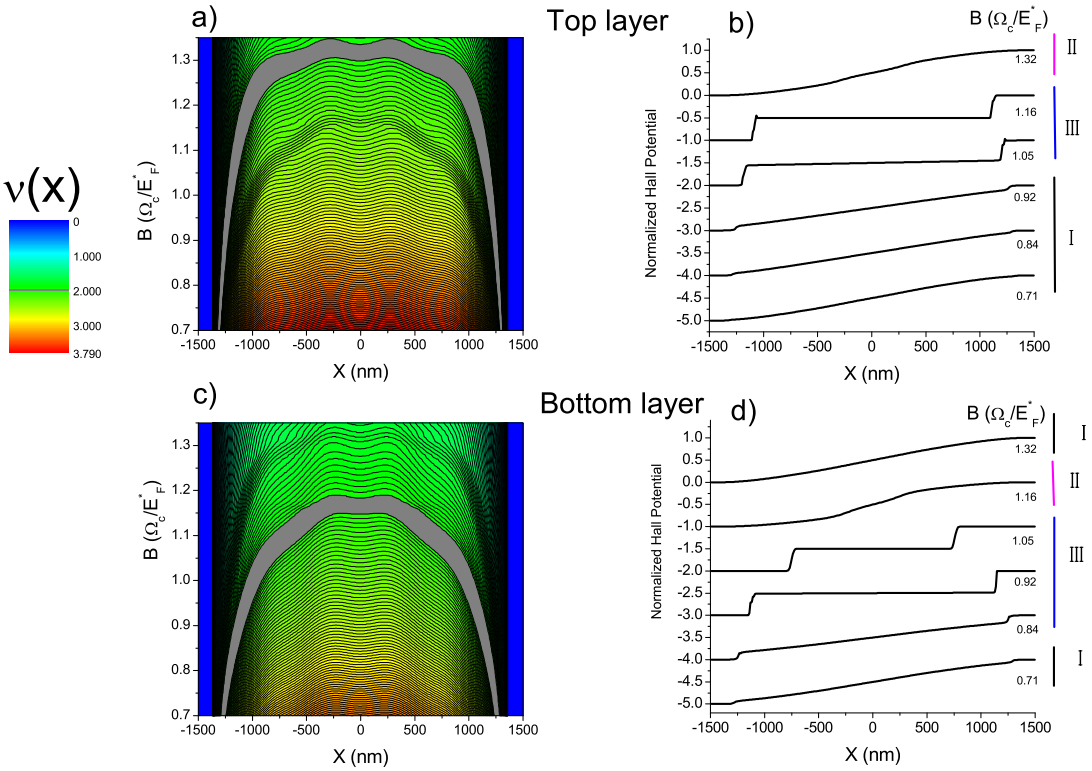

Figure 6.10: Self-consistently calculated density profiles (color scale) across the sample as a function of magnetic field (left panel) and (normalized) Hall potential profile of both layers for selected B values (right panel). The density mismatch is obtained by setting $V_0/E_0 = 0.05$ which results in $n_{el}^B/n_{el}^T = 0.84$ at a low temperature $k_BT/E_F^* = 0.0124$ for fixed $b/d = 0.9$.

previous chapter. To visualize this system, in Fig.6.10 the local filling factors (color scale) as a function of magnetic field is plotted for both layers together with the Hall potential profiles at selected magnetic field values. If one starts with a high magnetic field $\Omega_c/E_F^* \gtrsim 1.35$, i.e. $\nu(0) < 2$, the Fermi energy is pinned to the lowest LL and the system is compressible all over the sample, therefore equilibrium can be established within the sweeping time interval. This case corresponds to type I Hall potential profile in Fig. 4.13. Meanwhile the bottom layer is also compressible and exhibits a linear Hall potential variation. By decreasing the field strength one also decreases the energy separation between the LLs ($= \hbar\omega_c$). For a fixed average electron density, the Fermi energy is unpinned from the lowest LL at the minima, leading to an incompressible strip at the center ($\Omega_c/E_F^* \sim 1.32$) with a Hall potential profile of type II at

the top layer, whereas the bottom layer is still compressible and exhibits almost a linear Hall potential variation. At a smaller $B(\Omega_c/E_F^* \sim 1.27)$ the incompressible strip at the top layer becomes wider and then splits into two strips at $\Omega_c/E_F^* \sim 1.22$, that move towards the edges which results in a type III Hall potential profile ($0.92 \lesssim \Omega_c/E_F^* \lesssim 1.22$). In this interval the bottom layer changes its Hall potential profile **first** from type I to type II ($\Omega_c/E_F^* \sim 1.16$) **then** to type III ($\Omega_c/E_F^* \sim 1.1$). At a lower magnetic field ($\Omega_c/E_F^* \sim 0.92$) the incompressible strips at the top layer become ineffective as their widths become comparable with the magnetic length (known from Hartree calculations). This is a situation where the top layer again becomes compressible all over the sample and type I Hall potential profile is expected. Meanwhile there are two incompressible strips at the bottom layer, which are larger than the averaging length that results in type III Hall potential profile. We shall also note the contour lines in the left panel of Fig.6.10 that indicates the influence of the passive layers density distribution as a shadow to the active layer. This is due to the poor screening of the ISs at the passive layer, so that the active layer experiences the potential generated by the passive layer's donors.

In the interval, ($0.70 \lesssim \Omega_c/E_F^* \lesssim 0.84$) both layers are again compressible exhibiting type I Hall potential profile. For the other sweeping direction, one starts with an intermediate magnetic field value, e.g. $2 < \nu(0) < 4$ and $\Omega_c/E_F^* \sim 0.84$, where the 2DESs are compressible (type I), which is then followed by a type III potential at the bottom layer ($0.85 \lesssim \Omega_c/E_F^* \lesssim 1.11$) and type II at a higher magnetic field interval ($1.12 \lesssim \Omega_c/E_F^* \lesssim 1.16$). For $\Omega_c/E_F^* \gtrsim 1.16$ one ends with a compressible system (type I) at the bottom layer. To summarize, we see that the top layer experiences two different external potential sequences generated by the bottom layer as, for the down sweep the order is I-II-III-I and for the up sweep it is I-III-II-I. Here we finalize the promised discussion about **first** since, we can *now* define an order. For the down sweep starting from type I we first encounter with type II then with type III, whereas for the up sweep we first encounter with type III then with type II.

From the above observations we make a crucial assumption to handle the hysteresis-like effect as following: The symmetry breaking of the sweep direction can be simulated by considering the formation of the incompressible strips, namely by freezing the density distribution of the passive layer at two different magnetic field values corresponding to two sweep directions, within the QH plateau interval of the passive layer. To be more precise, we fix the passive layers density distribution at a magnetic field that corresponds to high B type III profile (similar to the curve in Fig.6.10b at $\Omega_c/E_F^* = 1.16$) for down sweep, whereas for the up sweep the field is fixed to a value of type III at low B (similar to the curve in Fig.6.10b at $\Omega_c/E_F^* = 0.92$).

Now we discuss the results obtained from the above model by examining the resistance curves for a constant total electron density. In Fig. 6.11 we show the longitudinal resistances calculated for two frozen density distributions. The density mismatch is obtained by applying a finite bias ($V_G/E_0 = 0.05$) to the top gate, such that the high plateau-edge of the bottom

layer coincides with the low plateau-edge of the top layer. We start our investigation again with the high magnetic field regime ($\Omega_c/E_F^* > 1.32$). Since both of the 2DESs are compressible, the distribution of the electrons do not affect the macroscopic resistance quantities as the total number of the electrons contributing to the dissipative current is preserved and no potential fluctuations are created. At a slightly lower magnetic field ($1.25 \lesssim \Omega_c/E_F^* \lesssim 1.3$) the top layer goes through the plateau regime, while the bottom layer is still compressible and, no significant change is observed in both R_l curves as the potential fluctuation created by the top layer is well screened by the bottom layer electrons. For the intermediate magnetic field values ($1.15 \lesssim \Omega_c/E_F^* \lesssim 1.25$) an interesting feature is observed in the resistance curves as $R_{xx}^B[down]$ (i.e. the longitudinal resistance of the bottom layer while sweeping the magnetic field down) and $R_{xx}^B[up]$ follows different paths. This is because of two assumed (different) external potentials for two sweep directions. For the down sweep we assume that the top layer electron distribution is frozen at $\Omega_c/E_F^* = 1.3$, whereas it is frozen at $\Omega_c/E_F^* = 1.1$ for the up sweep, in the QH plateau regime of the top layer. Hence, the bottom layer experiences strong potential fluctuations created by a large incompressible strip for down sweep, whereas it is weakly perturbed for the up sweep as there are only two narrow incompressible strips that generate the fluctuation. We have seen that the widths of the QH plateaus are effected by the strength of the perturbing potential (see also Fig.5.6 and related text). Therefore, $R_{xx}^B[down]$ is wider than $R_{xx}^B[up]$ yielding two different traces. For $0.70 \lesssim \Omega_c/E_F^* \lesssim 0.95$ interval both layers have incompressible strips, which are narrower than the averaging length. Now we concentrate on the hysteresis observed at the top layer in the interval $0.98 \lesssim \Omega_c/E_F^* \lesssim 1.2$. We freeze the bottom layers density distribution at $\Omega_c/E_F^* = 1.05$ for the up sweep and to $\Omega_c/E_F^* = 1.16$ for the down sweep. We see that, $R_{xx}^T[down]$ is wider than $R_{xx}^T[up]$. This is due to the large incompressible strip at the bottom layer that generates a large potential fluctuation to the top layer. Hence the $R_{xx}^T[down]$ curve is more stable and wide compared to $R_{xx}^T[up]$. There is no significant difference between sweep directions for both of the layers for $\Omega_c/E_F^* < 1.05$. In this B interval both layers have incompressible strips which are narrower than the averaging length. So that, although both layers can produce potential fluctuations they can be screened almost perfectly.

To summarize, simulating the non-equilibrium by two effective external potential profiles, the resistance curves follow different paths, whenever QH regimes of the layers coincide. This difference occurs due to the formation of the incompressible strips and is enhanced if these incompressible strips are large and stable. Meanwhile out-of-plateau regimes do not exhibit considerable differences, other than the small deviation at low magnetic field values caused by the incompressible strips narrower than the averaging length.

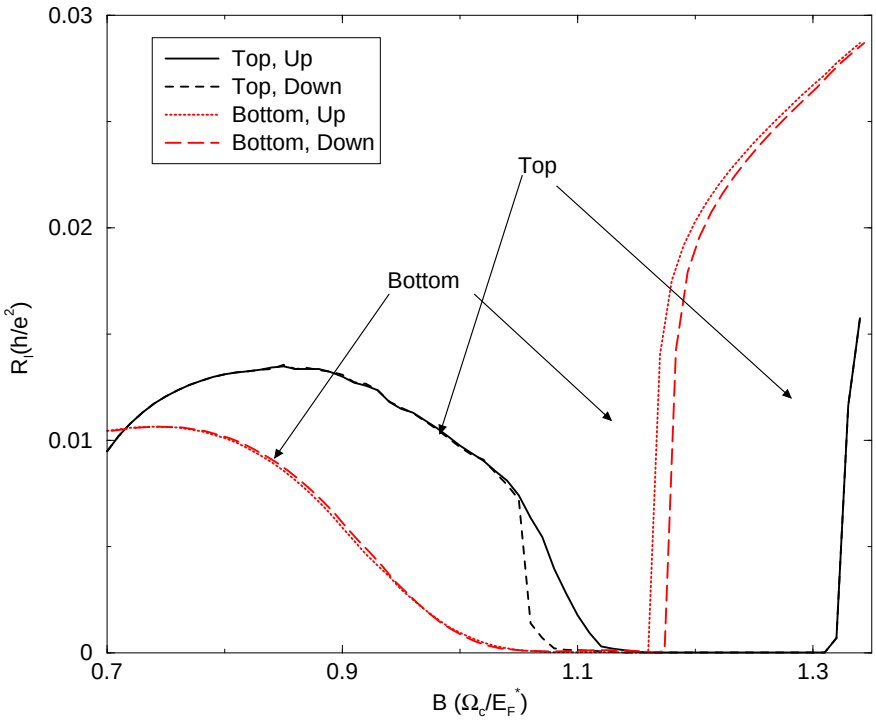

Figure 6.11: Longitudinal resistances for high density mismatch parameter. The plateau regions coincide between the high-magnetic field edge of the plateau of the bottom layer and the low-B edge of the top layer plateau.

6.7 Summary

In this chapter we have studied the screening properties of an electron-electron bilayer system. The electrostatic part is solved numerically using a self-consistent screening theory by exploiting the slow variation of the confining potential. We compared the electron distributions for vanishing magnetic field and temperature with the finite ones, and observed that a local charge imbalance is created due to the formation of incompressible strips. These dipolar strips produce external potential fluctuations, as a function of applied magnetic field, to the other layer. We have investigated properties of this potential fluctuation by comparing the interacting and non-interacting systems for a few characteristic B values and obtained the Hall resistances by a local scheme proposed in our recent work [65]. We considered these fluctuations as a perturbation to the other layer and observed that they widen, stabilize and shift the plateaus as expected. In Sec. 6.6 we have attempted to obtain qualitative arguments for the hysteresis-like behavior by reconsidering the symmetry breaking of the sweep direction, based on the long relaxation times of the incompressible regions. This is done by considering two external potential profiles. Our results show that the longitudinal resistance curves (also the Hall resistance curves) follows different paths if both of the layers have incompressible strips within the sample. The amplitude

of the deviation depends on the widths and the positions of the incompressible regions.

Chapter 7

Conclusion

Two and a half decades after the discovery of the quantized Hall effect [14] the microscopic picture of current distribution in the sample and its interplay with the Hall plateaus is still under debate. In this work, we attempt to contribute to the present understanding. We improved on the existing theories, and developed a self-consistent scheme starting from screening calculations, which provides theoretical results at an excellent agreement with the recent experiments [21]. Moreover, by a critical investigation of the disorder we have predicted a characteristic behavior for the high-temperature Hall resistance crossing the low-temperature one. Such that this crossing should occur at the high-magnetic field edge of the QH plateaus for a high mobility ($\mu > 2.0 \times 10^6 cm^2/Vs$) wide (2d=10$\mu$m) sample and the crossing is at the low-magnetic field edge for a narrow (2d=2μm) sample. Finally we implemented our model to an electron-electron bilayer system and obtained qualitative understanding of the basic features observed in the experiments.

In chapter 2 we introduced our formalism and gave a prescription to obtain self-consistent solutions of the Poisson-Schrödinger equations. In chapter 3 we examine, within the self-consistent Thomas-Fermi-Poisson approach, the low-temperature screening properties of a two-dimensional electron gas subjected to strong perpendicular magnetic fields. Numerical results for the unconfined 2DEG are compared with those for a simplified Hall bar geometry realized by two different confinement models. It is shown that in the strongly non-linear screening limit of zero temperature the total variation of the screened potential is related by simple analytical expressions to the amplitude of an applied harmonic modulation potential and to the strength of the magnetic field.

We studied the current and charge distribution in a two dimensional electron system, under the conditions of the integer quantized Hall effect in chapter 4, on the basis of a quasi-local transport model, that includes non-linear screening effects on the conductivity via the self-consistently calculated density profile. The existence of "incompressible strips" with integer Landau level filling factor is investigated within a Hartree-type approximation, and non-local

effects on the conductivity along those strips are simulated by a suitable averaging procedure. This allows us to calculate the Hall and the longitudinal resistance as continuous functions of the magnetic field B, with plateaus of finite widths and the well-known, exactly quantized values. We emphasize the close relation between these plateaus and the existence of incompressible strips, and we show that for B values within these plateaus the potential variation across the Hall bar is very different from that for B values between adjacent plateaus, in agreement with recent experiments [21].

Chapter five was devoted to investigate the effect of the disorder to the confining potential. There we demonstrate that, representing the impurity potential by a Gaussian potential is not sufficient to introduce long-range fluctuations. Therefore, we replaced them by Coulombic ones and obtained rough estimates of the range and the amplitude of the fluctuations. In the light of these findings, we added a harmonic perturbation potential to the confining potential in order to generate the long-range-part of the overall impurity potential in the translation invariant model. This treatment of the long-range fluctuations allowed us to resolve apparent discrepancies such as the dependence of the QH plateau width on the mobility and to understand the crossing values of the high and low temperature Hall resistances. An interesting outcome of this model is that, it predicts different crossing values depending on the sample width and mobility.

In the sixth chapter we implement the self-consistent Thomas-Fermi approach and local conductivity model to an electron-electron bilayer system. The presence of an incompressible strip, originating from screening calculations at the top (or bottom) layer is considered as a source of an external potential fluctuation to the bottom (or top) layer. This essentially yields modifications to the magneto-transport quantities as one drives an external fixed current through both of the layers. The effect of the density mismatch on the density and the potential fluctuations are systematically investigated. It is observed that the existence of the incompressible strips plays an important role simply due to their poor screening properties. The magneto-resistance hysteresis observed in the experiments is presented, which is a non-equilibrium effect, and simulated by freezing the electron distributions at two different magnetic field values corresponding to magnetic sweep directions. This model provides a qualitative understanding of the related experimental results.

As summary, with this work we provide theoretical and numerical findings that help uncover the not-well-understood microscopic picture of the current distribution in the quantized Hall-effect samples. A close relation between the Hall plateaus and the existence of the incompressible strips is found. The long-range effects of the disorder were found to be important and mistakenly neglected in the previous models as their inclusion to the theory removed discrepancies between the experimental and theoretical results. In addition the model used in this work provides qualitative agreement with the experimental results of an electron-electron bilayer system.

Chapter 8

Zusammenfassung

Diese Arbeit wurde durch Experimente zur Potential- und Stromverteilung in Quanten-Hall-Systemen motiviert, die in den letzten Jahren in der Abteilung von Klitzing am MIP für Festkörperforschung durchgeführt wurden und ergaben, dass elektrostatische Abschirmungseffekte in zweidimensionalen Elektronensystemen (2DES), die den ganzzahligen Quanten-Hall-Effekt (QHE) zeigen, sehr wichtig für das Verständnis der Stromverteilung innerhalb der Probe und der extremen Genauigkeit der gemessenen quantisierten Werte des Hall-Widerstands sind. Daraus ergab sich für die hier vorgelegte Arbeit das folgende Programm.

Zunächst wird, nach einem einleitenden Kapitel, in Kapitel 2 der Formalismus vorgestellt, mit dem in den späteren Kapiteln Elektronendichten und elektrostatische Potentiale, die z.B. das 2DES auf eine Probe mit Streifengeometrie eingrenzen, selbstkonsistent berechnet werden. Diese Selbstkonsistenz besteht aus zwei Teilen. Erstens wird, bei vorgegebenem Potential, die Elektronendichte berechnet. Zweitens wird aus vorgegebener Ladungsverteilung, bestehend aus (positiven) Hintergrundladungen und der (im ersten Schritt berechneten) Elektronenladungsdichte, und geeigneten Randbedingungen (konstantes Potential auf metallischen Gates) durch Lösen der Poisson-Gleichung das elektrostatische Potential berechnet. Wenn wir im ersten Schritt, unter Berücksichtigung der Fermi-Dirac-Statistik, die Elektronendichte quantenmechanisch aus den Energieeigenfunktionen und -werten berechnen, erhalten wir die Hartree-Näherung, die die Dichte als nichtlokales Funktional des Potentials liefert. Wenn man die Ausdehnung der Wellenfunktionen auf der Längenskala, auf der sich das Potential typischerweise ändert, vernachlässigen kann, so vereinfacht sich die Hartree-Näherung zur Thomas-Fermi-Näherung, die einen lokalen Zusammenhang zwischen Elektronendichte und Potential beschreibt. Die meisten der konkreten Rechnungen wurden im Rahmen dieser selbstkonsistenten Thomas-Fermi-Poisson-Näherung durchgeführt.

Im Kapitel 3 wird allgemein das Abschirmverhalten eines 2DES im hohen Magnetfeld untersucht. Wir betrachten die Antwort auf eine harmonische Potentialmodulation im unbegrenzten 2DES und in streifenförmig begrenzten Systemen mit zwei unterschiedlichen Arten von

Randbedingungen. Bei tiefen Temperaturen und hohen Magnetfeldern finden wir extrem nichtlineare Abschirmung. Im unbegrenzten 2DES charakterisieren wir die Abschirmung, indem wir die gesamte Variation des selbstkonsistent berechneten Potentials als Funktion der Amplitude des aufgeprägten $cosinus$-Potentials berechnen. Bei festem Magnetfeld ergeben sich so Stufenfunktionen, deren Gestalt stark vom Füllfaktor der Landau-Niveaus im homogenen Zustand ohne aufgeprägtes Potential abhängt (siehe Abbildungen 3.2- 3.6). Vielleicht noch unerwartetere Kurven ergeben sich, wenn man bei festem Modulationspotential die Varianz des selbstkonsistenten Potentials gegen das Magnetfeld B aufträgt (Abb. 3.9). Die Resultate lassen sich aber leicht verstehen und (bei Temperatur $T = 0$) in einem einfachen Schema (Abb. 3.7) zusammenfassen. Als ordnendes Prinzip stellt sich heraus, dass sich stets Zustände einstellen, in denen die Elektronendichte möglichst wenig von der bei verschwindendem Magnetfeld abweicht. Wenn die Zyklotronenergie groß gegen die thermische Energie k_BT ist, erfordert das, dass in den großen Bereichen, in denen die Dichte variiert, ein Landau-Niveau unmittelbar an dem, im Gleichgewicht konstanten, elektrochemischen Potential liegen muss ($E_n \approx \mu^\star$, "pinning"). Man nennt diese Bereiche kompressibel. In den kompressiblen Bereichen können Elektronen leicht umverteilt werden, d.h. die Dichte ist leicht veränderbar und in diesen Bereichen gibt es extrem effektive Abschirmung. Existieren kompressible Bereiche mit unterschiedlichen Landau-Niveaus (E_n) am elektrochemischen Potential, z.B. bei großer Modulation oder weil die Dichte zum Probenrand hin abnimmt, so gibt es zwischen benachbarten kompressiblen Bereichen mit unterschiedlichen Landau-Quantenzahlen n "inkompressible" Bereiche, in denen $\mu^\star$ zwischen zwei Landau-Niveaus liegt. Dort sind alle Landau-Niveaus unterhalb von $\mu^\star$ besetzt, die oberhalb leer. Folglich ist dort der Füllfaktor ganzzahlig und die Dichte konstant. Das Wechselspiel zwischen kompressiblen und inkompressiblen Bereichen bestimmt das Abschirmverhalten. Randeffekte erweisen sich nur in solchen Magnetfeldintervallen als wichtig für die Abschirmung im Inneren einer streifenförmigen Probe, in denen (schon ohne aufgeprägte Modulation) in der Probenmitte ein neuer inkompressibler Streifen entsteht.

Im Kapitel 4 wird die Rolle der inkompressiblen Streifen in einer idealisierten, streifenförmigen Hall-Probe untersucht. Mithilfe einer lokalen Version des Ohmschen Gesetzes berechnen wir bei vorgegebenen Gesamtstrom die Stromdichte und das nun ortsabhängige elektrochemische Potential, dessen Gradient die Stromdichte treibt. Für den lokalen Leitfähigkeitstensor nehmen wir ein für homogenes 2DES berechnetes Resultat und ersetzen den Füllfaktor jeweils durch den lokalen Wert. Dadurch ergibt sich, dass bei Existenz inkompressibler Streifen der gesamte Strom auf diese Streifen eingeschränkt ist, in denen die Komponenten des spezifischen Widerstands die Werte des freien, idealen 2DES haben, also verschwindenden longitudinalen und quantisierten Hall-Widerstand. Aus Hartree-Rechnungen zeigen wir, dass es inkompressible Streifen nur in Magnetfeldintervallen endlicher Breite (um ganzzahlige Füllfaktoren) gibt und dass in der Nähe von Füllfaktor 4 es nur inkompressible Streifen mit dem lokalen Füll-

faktor $\nu(x) = 4$ gibt, aber nicht solche mit $\nu(x) = 2$, in Gegensatz zu dem Ergebnis der Thomas-Fermi-Poisson-Näherung, die hier nicht gültig ist. Um diese Unzulänglichkeit der Thomas-Fermi-Poisson-Näherung und Artefakte des strikt lokalen Modells zu beheben, führen wir die Rechnungen mit einem (auf der Skala des mittleren Elektronenabstands) gemittelten Leitfähigkeitstensors aus. Damit erhalten wir, im Rahmen einer Linear-Response-Rechnung, sehr schöne Übereinstimmung mit den Potentialmessungen, die diese Dissertation motivierten, einen kausalen Zusammenhang zwischen der Existenz inkompressibler Streifen und der Existenz von Plateaus im QHE, und ein Verständnis der extremen Genauigkeit, mit der die quantisierten Widerstandswerte reproduziert werden können, unabhängig von Probenmaterial und -geometrie.

Im Kapitel 5 untersuchen wir das Zufallspotential, in dem sich die Elektronen bewegen. Wir gehen davon aus, dass sich hinter einer undotierten Schicht eine Ebene mit zufällig verteilten ionisierten Donatoren befindet, deren Coulomb-Potentiale sich zu dem Zufallspotential überlagern. Wir weisen darauf hin, dass sich die langreichweitigen Fluktuationen dieses Potentials anders verhalten als die kurzreichweitigen. Die kurzreichweitigen klingen mit dem Abstand der Donatorebene von der Ebene des 2DES exponentiell ab, werden aber (bei $B = 0$) nur schwach durch das 2DES abgeschirmt. Diese Fluktuationen haben wir durch die endlichen Leitfähigkeiten und die Stoßverbreiterung der Landau-Niveaus berücksichtigt. Die langreichweitigen Fluktuationen, andererseits, sind nur schwach von der Entfernung der Donatorebene abhängig, werden aber stark vom 2DES abgeschirmt. Diese sollte man bei der selbstkonsistenten Abschirmungsrechnung explizit berücksichtigen. Erste Versuche in dieser Richtung zeigen, dass sie die Quanten-Hall-Plateaus verbreitern, verschieben und stabilisieren können. Sie sollten besonders bei breiten Proben wichtig werden, bei denen sie zusätzliche inkompressible Streifen im Probeninneren verursachen können.

Schließlich diskutieren wir in Kapitel 6 Abschirmungseffekte in einem Doppelschichtsystem aus zwei parallelen 2DES. Interessante neue Effekte treten auf, wenn die Schichten verschiedene Dichten haben. Das Auftreten inkompressibler Streifen in der einen Schicht kann dann drastische Auswirkungen auf die andere Schicht haben. Widerstandsmessungen in Abhängigkeit vom Magnetfeld, die kürzlich an solchen Systemen durchgeführt wurden, zeigen, dass am Rande eines QH-Plateaus Hysterese auftritt, d.h. dass die für ansteigendes Magnetfeld gemessene Kurve nicht mit der für abfallendes Magnetfeld gemessenen Kurve übereinstimmt, wenn dieser Magnetfeldbereich in ein QH-Plateau der anderen Schicht fällt. Wir entwickeln ein Modell und beschreiben Modellrechnungen, die dieses Phänomen plausibel machen.

Appendix A

The Kernels

In this appendix I recall the relevant solutions of the Laplace equation in two dimensions following Ref. [60].

A.1 Periodic boundary conditions and perpendicular gates

The solution of the Poisson equation

$$\vec{\nabla}^2_{x,z}\Phi(x,z) = \frac{\partial^2\Phi(x,z)}{\partial x^2} + \frac{\partial^2\Phi(x,z)}{\partial z^2} = -4\pi\delta(x-x_0)\delta(z-z_0) \tag{A.1}$$

corresponding to a unit line 'charge' (a long thin wire, perpendicular to the xz-plane of unit charge, q, per unit length of wire) concentrated at the point (x_0, z_0) is the Green's function

$$G(x,z|x_0,z_0) = q\Re e[-2\ln(\xi-\xi_0)] = q\ln(1/|\xi-\xi_0|^2) \tag{A.2}$$

with the complex argument $\xi = x + iz$. One can obtain the potential, $\Phi(x,z)$, due to a unit line charge at point (x_0, z_0), placed by an infinite conducting plane with zero potential located at $z = 0$ as

$$\Phi(x,z) = \ln[\frac{(x+x_0)^2+(z-z_0)^2}{(x-x_0)^2+(z-z_0)^2}] \tag{A.3}$$

using the method of 'image charges', i.e. one replaces the infinite conducting plane by an image charge with an opposite sign concentrated at point $(-x_0, z_0)$. One can extend this scheme to calculate the Green's function for homogeneous 2DES. First I consider a line source at x_0, in between two infinite conducting planes at $x = 0$ and $x = a$, which are kept at zero potential. Then n^{th} image charge will have a zero at $(\xi-\xi_0)-(na)$ thus G_n is given by,

$$G_n = -2q\ln[1/|(\xi-\xi_0)-(na)|] \tag{A.4}$$

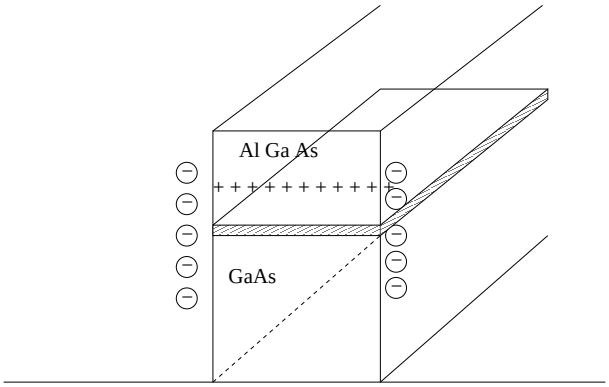

Figure A.1: The 2DES is formed at the interface of the AlGaAs heterostructure and electrons are depleted from the edges by the surface charges.

and note that

$$G = \sum_{n=-\infty}^{\infty} G_n.$$

With a little manipulation G_n can be written as

$$G_n = -q \ln[|\frac{1}{1 - (\frac{\pi(\xi-\xi_0)/a}{n\pi})^2}|] \tag{A.5}$$

and the summation becomes

$$G = -2q \sum_{n=1}^{\infty} \ln[|\frac{1}{1 - (\frac{\pi(\xi-\xi_0)/a}{n\pi})^2}|] + \ln[1/|\frac{\xi\pi}{a}|]. \tag{A.6}$$

Using the identity

$$\frac{\sin((\xi-\xi_0)\pi/a)}{((\xi-\xi_0)\pi/a)} = \prod_{n=1}^{\infty}(1 - (\frac{\pi(\xi-\xi_0)/a}{n\pi})^2)$$

the solution is calculated as

$$G = 2q \ln[|\sin((\xi-\xi_0)\pi/a)|]. \tag{A.7}$$

Similarly one can obtain the relevant kernel for the homogeneous 2DES by replacing the conducting planes at $x = \pm a/2$, and implying periodic boundary conditions, i.e. $V(-a/2) = V(a/2)$ at the $z = 0$ plane as:

$$K(x, x_0) = -\ln\left|2\sin\frac{\pi}{a}(x - x_0)\right|, \tag{A.8}$$

and for the mesa etched geometry one takes the period as $2d$ and places the plates at $x = \pm d$, with the boundary conditions

$$V(-d) = V(d) = 0.$$

Then the kernel is obtained as

$$K_{\perp}(x, x_0, z, z_0) = -\ln\left(\frac{\cos^2 \frac{\pi}{4d}(x + x_0) + \gamma^2}{\sin^2 \frac{\pi}{4d}(x - x_0) + \gamma^2}\right) \tag{A.9}$$

where $\gamma = \sinh(\pi|z - z_0|/4d)$ gives the z dependence of the potential.

A.2 In-plane gated Hall bar

This model was introduced to study the electrostatics of edge channels at the gate-induced 2DES in the absence of magnetic fields [78]. Since then it has been used extensively to investigate the electrostatic properties of the 2DES also in the presence of magnetic field [10–13]. It is assumed that all charges reside in the plane $z = 0$, which is a reasonable approximation if the width of the electron channel, $2d$, is much larger than the separation between electrons and donors. The 2DES is laterally confined by in-plane gates located at $x < -d$ and $x > d$, which are kept at voltages V_L and V_R, respectively (See Fig. A.3 and Fig. A.4). The electrostatic potential, $V(x, z)$, is obtained by solving the 2-D Laplace equation

$$\vec{\nabla}^2_{x,z} V(x, z) = 0 \tag{A.10}$$

using the theory of complex functions as follows: One assumes that the solution can be divided into two parts, i.e. $V(x, z) = V_1(x, z) + V_2(x, z)$. Solution for $V_1(x, z)$ can be obtained by considering the conventional theory of analytic functions, with the boundary conditions

$$V_1(x, z = 0) = \begin{cases} V_L, & x < -d \\ V_R, & x > d \end{cases} \tag{A.11}$$

and,

$$\left.\frac{\partial V_1(x, z)}{\partial z}\right|_{z\to 0} = 0 \quad |x| < d \tag{A.12}$$

and the solution is obtained as

$$V_1(x, z) = V_R + \frac{V_L - V_R}{\pi} \Im m \ln\{\frac{\xi}{d} - \sqrt{\xi^2/d^2 - 1}\}, \tag{A.13}$$

where the complex variable ξ is defined by

$$\xi = x + iz.$$

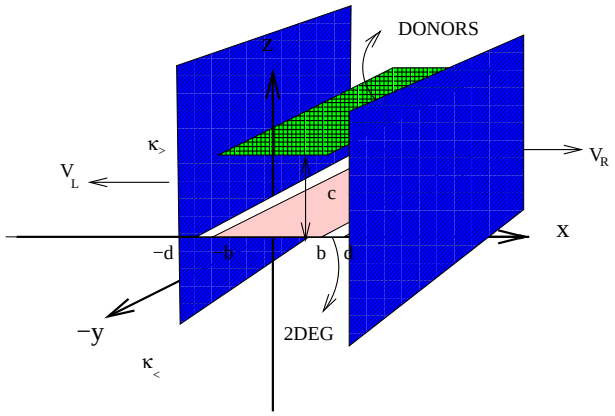

Figure A.2: Electron channel is formed in the interval $|x| < |b|$ of xy- plane, and the positive charges reside on the plane at a distance c, distributed homogeneously in the interval $|x| < |d|$, with density n_0.

Rewriting Eq.(A.13) in the interval $|x| < d$ and at $z = 0$, one obtains

$$V_1(x,z) = \frac{V_R + V_L}{2} - \frac{V_L - V_R}{\pi} \arcsin(\frac{x}{d}). \tag{A.14}$$

The potential $V_2(x,z)$, depends on the boundary conditions resulting from the displacement field of the charge density $\rho(x)$ given by

$$\rho(x) = e[n_0 - n_{el}(x)], \tag{A.15}$$

where n_0 is the density of positive background charges. The solution satisfies the boundary conditions

$$\kappa_> \frac{\partial V_2(x, z = 0^+)}{\partial z} - \kappa_< \frac{\partial V_2(x, z = 0^-)}{\partial z} = -4\pi\rho(x), \tag{A.16}$$

for $|x| < d$, and $V_2(x,0) = 0$ for $|x| > d$. One writes $V_2(x,z)$ as the imaginary part of a holomorphic function $F(\xi)$ in the complex plane

$$V_2(x,z) = \Im m F(\xi), \tag{A.17}$$

where $F(\xi)$ satisfies;

$$\Re e \frac{dF}{d\xi}\bigg|_{\xi=x+i0^+} = r(x), \qquad \text{for} |x| < d$$

$$\Im m \frac{dF}{d\xi}\bigg|_{\xi=x+i0^+} = 0, \qquad \text{for} |x| > d$$

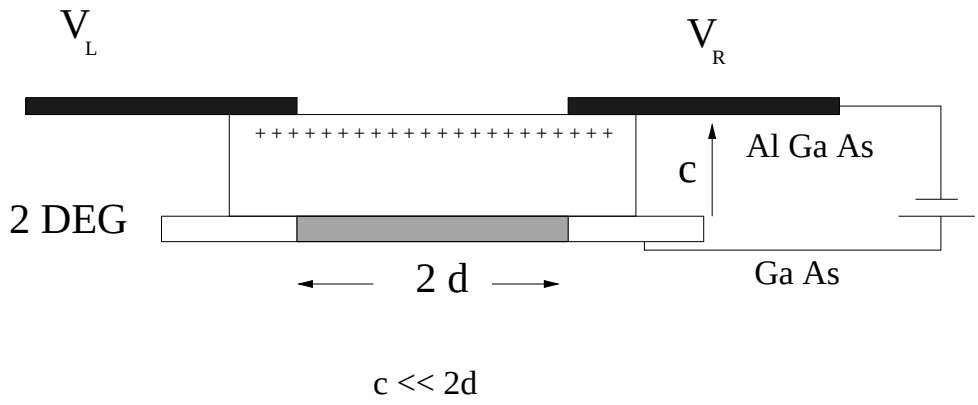

Figure A.3: The 2DES is formed at the interface of the AlGaAs heterostructure and electrons are depleted from the edges by the gate potentials.

with $r(x) = -4\pi\rho(x)/(\kappa_> + \kappa_<)$, therefore the imaginary part of the analytical function

$$f(\xi) = i\frac{dF}{d\xi}[d^2 - \xi^2]^{1/2}$$

is known along the whole real axis:

$$\Im m(f(x)) = r(x)[d^2 - \xi^2]^{1/2}, |x| < d$$

$$\Im m(f(x)) = 0, |x| > d.$$

To reconstruct $f(\xi)$ for the whole lower half-plane one uses the Schwartz integral

$$f(\xi) = \frac{1}{\pi i}\int_{-\infty}^{\infty}\frac{\Im m(f(x))}{x-\xi}dx + c_*$$

$$= \frac{1}{\pi i}\int_{-d}^{d}\frac{\Im m(f(x))}{x-\xi}dx + c_*$$

where c_* is the real constant of integration. Setting the constant to be zero one obtains the potential,

$$V_2(x) = -\frac{1}{\pi}\int_{-d}^{d} dt r(t)K(x,t), \tag{A.18}$$

and the kernel in Eq. (2.2), with $-x_l = x_r = d$, is obtained as [13]

$$K_{\|}(x,t) = \ln\left|\frac{\sqrt{(d^2-x^2)(d^2-t^2)} + d^2 - tx}{(x-t)d}\right|. \tag{A.19}$$

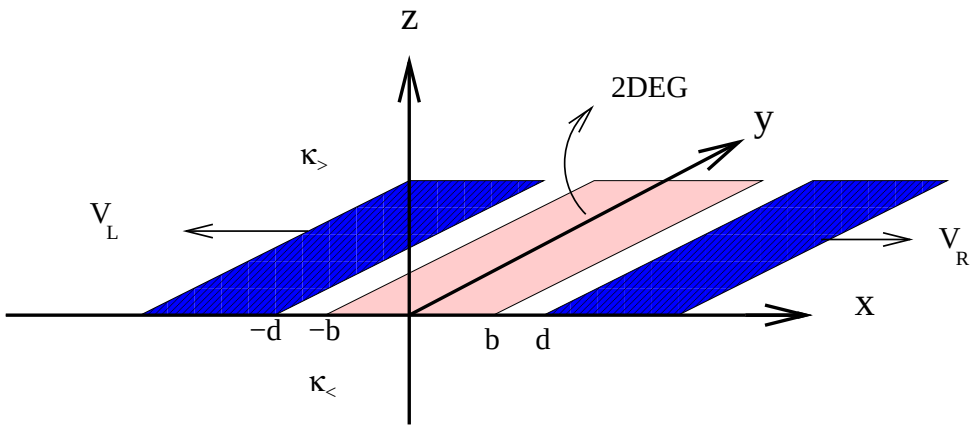

Figure A.4: Electron channel is formed in the interval $|x| < |b|$ of xy- plane, and the positive charges at the same plane distributed homogeneously in the interval $|x| < |d|$, with density n_0.

Appendix B

SCBA conductivities

The low-temperature, high-field magnetotransport, determined by elastic scattering of the 2D electrons by randomly distributed impurities with scattering potentials of arbitrary range, has been studied by Ando and coworkers. [59, 68, 69] The results for the case of non-overlapping LLs can be summarized as

$$\nu = g_s \sum_{n=0}^{\infty} \int dE\, A_n(E)\, f(E-\mu)\,, \tag{B.1}$$

$$\sigma_l = g_s \sum_{n=0}^{\infty} \int dE \left[-\frac{\partial f}{\partial E}\right] \sigma_{xx}^{(n)}(E)\,, \tag{B.2}$$

$$\sigma_H = \frac{e^2}{h}\,\nu - \Delta\sigma_H\,, \tag{B.3}$$

$$\Delta\sigma_H = g_s \sum_{n=0}^{\infty} \int dE \left[-\frac{\partial f}{\partial E}\right] \Delta\sigma_{yx}^{(n)}(E)\,, \tag{B.4}$$

with the spectral functions of widths Γ_n,

$$A_n(E) = \frac{2}{\pi\Gamma_n}\sqrt{1-\left(\frac{E-E_n}{\Gamma_n}\right)^2}\,, \tag{B.5}$$

centered around the Landau energies (2.7), and

$$\sigma_{xx}^{(n)}(E) = \frac{e^2}{h}\,\frac{\pi}{2}\left[\Gamma_n^{xx}\, A_n(E)\right]^2, \tag{B.6}$$

$$\Delta\sigma_{yx}^{(n)}(E) = \frac{e^2}{h}\,\frac{\pi^2}{4}\frac{\Gamma_n^{yx}}{\hbar\omega_c}\left[\Gamma_n^{yx}\, A_n(E)\right]^3. \tag{B.7}$$

Assuming a single type of impurities with the Gaussian potential (4.11), these parameters can be expressed in terms of the integrals

$$(\Gamma_n^{(j)})^2 = \Gamma^2 \int_0^{\infty} dx\, g_n^{(j)}(x)\, \exp(-[1+\alpha^2]x)\,, \tag{B.8}$$

where $\Gamma^2 = 4n_I V_0^2/(2\pi l^2)$ and $\alpha = R/l$, and the weight functions

$$g_n^{(0)}(x) = \left[L_n^0(\alpha^2 x)\right]^2, \quad g_n^{(d)}(x) = \frac{1-x}{2\alpha^2}\, g_n^{(0)}(x)\,,$$
$$g_n^{(\pm)}(x) = \frac{x}{\sqrt{2n+1\pm 1}}\, L_n^0(\alpha^2 x) L^1_{n-(1\mp 1)/2}(\alpha^2 x)$$

are determined by the associated Laguerre polynomials $L_n^m(x)$. With these notations one obtains

$$\Gamma_n^2 = (\Gamma_n^{(0)})^2\,, \quad (\Gamma_n^{xx})^2 = (\Gamma_n^{(d)})^2\,, \tag{B.9}$$
$$(\Gamma_n^{yx})^4 = (\Gamma_n^{(+)})^4 + (\Gamma_n^{(-)})^4\,. \tag{B.10}$$

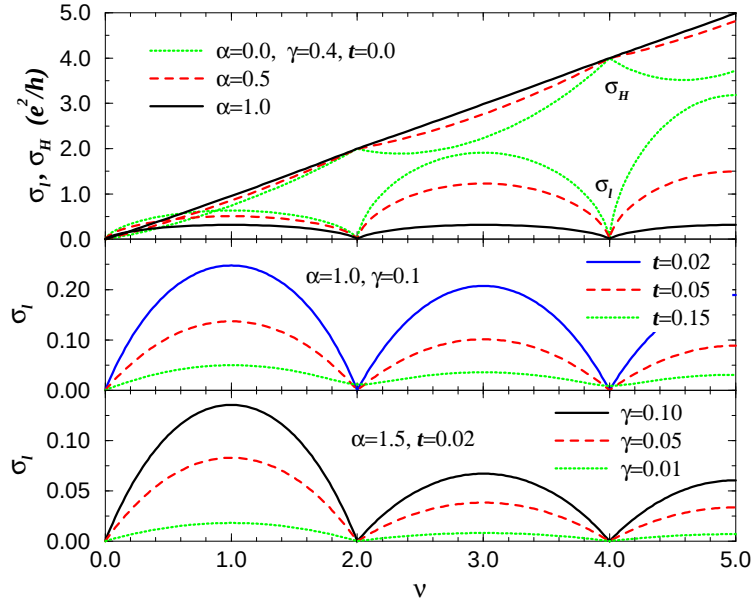

Figure B.1: SCBA results for longitudinal (σ_l) and Hall (σ_H) conductivity, in units of e^2/h, versus filling factor, at fixed magnetic field for different values of impurity range ($\alpha = R/l$) and strength ($\gamma = \Gamma/\hbar\omega_c$), and of temperature ($t = k_B T/\hbar\omega_c$). For the two lower panels the correction $-\Delta\sigma_H$ to $\sigma_H^0 = e^2\nu/h$ is negligible, and σ_H is not shown.

In the limit of short-range scattering potentials, $\alpha \to 0$, one has $\Gamma_n^2/\Gamma^2 = 1$, $(\Gamma_n^{xx}/\Gamma)^2 = n + 1/2$ and $(\Gamma_n^{yx}/\Gamma)^4 = n + 1/2$. With increasing α these parameters decrease and remain for $\alpha > 1$ about an order of magnitude smaller than their $\alpha = 0$ values. [68, 69]

Some typical SCBA results are shown in Fig. B.1. In general, σ_l and the correction $\Delta\sigma_H$ to the free electron Hall conductivity $\sigma_H^0 = e^2\nu/h$ decrease with increasing range of the scattering potentials.

At zero temperature, $\Delta\sigma_H$ is proportional to $\Gamma/\hbar\omega_c$ with a factor depending only on the range parameter $\alpha = R/l$. The longitudinal conductivity $\sigma_l(\nu)$, on the other hand, depends only on α and not on $\Gamma^2 = (2/\pi)\hbar\omega_c\,\hbar/\tau_0$, i.e. depends not on the impurity concentration n_I and strength V_0 entering the $B = 0$ relaxation rate $\hbar/\tau_0 = n_I V_0^2 m/\hbar^2$. This is very different from the $B = 0$ conductivity $\sigma_0 = e^2 n_{\rm el}\tau_{tr}/m$ obtained for the impurity model (4.11), which depends on $n_{\rm el} = k_F^2/2\pi$ and via τ_{tr} on both the potential strength and range. For $B = 0$ collision broadening effects can be neglected, and one obtains for elastic scattering at the Fermi egde

$$\begin{aligned} \frac{\hbar}{\tau_{tr}} &= \frac{n_I m}{\hbar^2}\int_{-\pi}^{\pi}\frac{d\varphi}{2\pi}\left[v_q\right]^2_{q=k_F[2(1-\cos\varphi)]^{1/2}}(1-\cos\varphi) \\ &= \frac{\hbar}{\tau_0}\left[e^{-x}(I_0(x)-I_1(x))\right]_{x=(Rk_F)^2}, \end{aligned} \tag{B.11}$$

where the last equality holds for our impurity potential (4.11), with Fourier transform $v_q = V_0\exp(-R^2q^2/4)$, and $I_\nu(x)$ is a modified Bessel function. This leads for $Rk_F \gg 1$ to $\tau_0/\tau_{tr} \approx [\sqrt{8\pi}\,(Rk_F)^3]^{-1}$. With increasing temperature, the peak values of $\sigma_l(\nu)$ decrease and the minima at even integer ν values are no longer exponentially small for $k_BT/\hbar\omega_c > 0.1$. This behavior of the SCBA results, shown in the middle panel of Fig. B.1, is similar to that of the Gaussian model treated in Ref. [27]. At finite temperature, the longitudinal conductivities $\sigma_l(\nu)$ increase with γ, i.e., with increasing scattering strength (bottom panel of Fig. B.1). This is as expected from the Drude picture for $\omega_c\tau_{tr} \gg 1$: $\sigma_l \approx \sigma_0/(\omega_c\tau_{tr})^2 \propto 1/\tau_{tr}$.

List of Figures

List of Tables

Bibliography

[1] U. Wulf, V. Gudmundsson and R. R. Gerhardts, Phys. Rev. B **38**, 4218 (1988).

[2] A. L. Efros, Solid State Commun. **67**, 1019 (1988).

[3] A. L. Efros, F. G. Pikus and V. G. Burnett, Phys. Rev. B **47**, 2233 (1993).

[4] V. G. Burnett, A. L. Efros and F. G. Pikus, Phys. Rev. B **48**, 14365 (1993).

[5] N. R. Cooper and J. T. Chalker, Phys. Rev. B **48**, 4530 (1993).

[6] V. Tsemekhman, K. Tsemekhman, C. Wexler, J. H. Han and D. J. Thouless, Phys. Rev. B **55**, R10201 (1997).

[7] K. Güven, R. R. Gerhardts, I. I. Kaya, B. E. Sagol and G. Nachtwei, Phys. Rev. B **65**, 155316 (2002).

[8] I. I. Kaya, G. Nachtwei, K. von Klitzing and K. Eberl, Europhys. Lett. **46**, 62 (1999).

[9] I. I. Kaya, G. Nachtwei, B. E. Sagol, K. von Klitzing and K. Eberl, Physica E **6**, 128 (2000).

[10] D. B. Chklovskii, B. I. Shklovskii and L. I. Glazman, Phys. Rev. B **46**, 4026 (1992).

[11] D. B. Chklovskii, K. A. Matveev and B. I. Shklovskii, Phys. Rev. B **47**, 12605 (1993).

[12] K. Lier and R. R. Gerhardts, Phys. Rev. B **50**, 7757 (1994).

[13] J. H. Oh and R. R. Gerhardts, Phys. Rev. B **56**, 13519 (1997).

[14] K. von Klitzing, G. Dorda and M. Pepper, Phys. Rev. Lett. **45**, 494 (1980).

[15] H. Bachmair, E. O. Göbel, G. Hein, J. Melcher, B. Schumacher, J. Schurr, L. Schweitzer and P. Warnecke, Physica E **20**, 14 (2003).

[16] C. Wexler and D. J. Thouless, Phys. Rev. B **49**, 4815 (1994).

[17] M. R. Geller and G. Vignale, Phys. Rev. B **50**, 11714 (1994).

[18] M. R. Geller and G. Vignale, Phys. Rev. B **52**, 14137 (1995).

[19] R. Knott, W. Dietsche, K. v. Klitzing, K. Eberl and K. Ploog, Semicond. Sci. Technol. **10**, 117 (1995).

[20] P. Weitz, E. Ahlswede, J. Weis, K. v. Klitzing and K. Eberl, Physica E **6**, 247 (2000).

[21] E. Ahlswede, P. Weitz, J. Weis, K. von Klitzing and K. Eberl, Physica B **298**, 562 (2001).

[22] E. Ahlswede, J. Weis, K. von Klitzing and K. Eberl, Physica E **12**, 165 (2002).

[23] P. Weitz, E. Ahlswede, J. Weis, K. v. Klitzing and K. Eberl, Appl. Surf. Sci. **157**, 349 (2000).

[24] A. Siddiki and R. R. Gerhardts, Phys. Rev. B **68**, 125315 (2003).

[25] A. M. Chang, Solid State Commun. **74**, 871 (1990).

[26] D. Pfannkuche and J. Hajdu, Phys. Rev. B **46**, 7032 (1992).

[27] K. Güven and R. R. Gerhardts, Phys. Rev. B **67**, 115327 (2003).

[28] R. E. Prange, Phys. Rev. B **23**, 4802 (1981).

[29] B. Kramer, S. Kettemann and T. Ohtsuki, Physica E **20**, 172 (2003).

[30] H. Aoki and T. Ando, Solid State Commun. **18**, 1079 (1981).

[31] R. B. Laughlin, Phys. Rev. B **23**, 5632 (1981).

[32] B. I. Halperin, Phys. Rev. B **25**, 2185 (1982).

[33] T. Ando, J. Phys. Soc. Japan **53**, 3101 (1984).

[34] L. Schweitzer, B. Kramer and A. MacKinnon, Z. Physik B **59**, 379 (1985).

[35] D. Vollhardt and P. Wölfle, Phys. Rev. B **22**, 4666 (1980).

[36] R. Woltjer, R. Eppenga, J. Mooren, C. E. Timmering and J. P. André, Europhys. Lett. **2**, 149 (1986).

[37] R. Woltjer, R. Eppenga and M. F. H. Schuurmans, in *High Magnetic Fields in Semiconductor Physics*, Vol. 71 of *Springer Series in Solid-State Sciences*, edited by G. Landwehr (Springer-Verlag, Berlin, 1987), p. 104.

[38] P. J. Price, Physica **117B**, 750 (1983).

[39] T. J. Gramila, J. P. Eisenstein, A. H. MacDonald, L. N. Pfeiffer and K. W. West, Phys. Rev. Lett. **66**, 1216 (1991).

[40] U. Sivan, P. M. Solomon and H. Shtrikman, Phys. Rev. Lett. **68**, 1196 (1992).

[41] N. P. R. Hill, J. T. Nicholls, E. H. Linfield, M. Pepper, D. A. Ritchie, A. R. Hamilton and G. A. C. Jones, J. Phys.:Condens Matter **8**, L577 (1996).

[42] H. Rubel, A. Fischer, W. Dietsche, K. von Klitzing and K. Eberl, Phys. Rev. Lett. **78**, 1763 (1997).

[43] X. Feng, H. Noh, S. Zelakiewicz and T. J. Gramila, Bull. Am. Phys. Soc. **42**, 487 (1997).

[44] J. P. Eisenstein, L. N. Pfeiffer and K. W. West, Bull. Am. Phys. Soc. **42**, 486 (1997).

[45] A. P. Jauho and H. Smith, Phys. Rev. B **47**, 4420 (1993).

[46] H. C. Tso and P. Vasilopoulos, Phys. Rev. B **45**, 1333 (1992).

[47] L. Zheng and A. H. MacDonalds, Phys. Rev. B **48**, 8203 (1993).

[48] B. I. Halperin, P. A. Lee and N. Read, Phys. Rev. B **47**, 7312 (1993).

[49] S. Shaki, Phys. Rev. B **56**, 4098 (1997).

[50] M. C. Bonsager, K. Flensberg, B. Y. K. Hu and A. P. Jauho, Phys. Rev. B **56**, 10314 (1997).

[51] J. P. Eisenstein, L. N. Pfeiffer and K. W. West, Phys. Rev. Lett. **68**, 674 (1992).

[52] B. Tanatar and D. M. Ceperley, Phys. Rev. B **39**, 5005 (1989).

[53] E. Tutuc, R. Pillarisetty, S. Melinte, E. D. Poortere and M. Shayegan, Phys. Rev. B **68**, 201308 (2003).

[54] W. Pan, J. Reno and J. Simmons, cond-mat/0407577 (2004).

[55] G. Bertotti, in *Hysteresis and Magnetism* (Academic Press, New York, 1998).

[56] V. Dolgopolov, A. Shashkin, N. Zhitenev, S. Dorozhkin and K. v. Klitzing, Phys. Rev. B **46**, 12560 (1992).

[57] J. Huels, J. Weis, J. Smet, K. v. Klitzing and Z. R. Wasilewski, Phys. Rev. B **69**, 085319 (2004).

[58] A. Siddiki and R. R. Gerhardts, in *Proc. 15th Intern. Conf. on High Magnetic Fields in Semicond. Phys.*, edited by A. R. Long and J. H. Davies (Institute of Physics Publishing, Bristol, 2002).

[59] T. Ando, A. B. Fowler and F. Stern, Rev. Mod. Phys. **54**, 437 (1982).

[60] P. M. Morse and H. Feshbach, *Methods of Theoretical Physics* (McGraw-Hill, New York, 1953), Band II, p. 1240.

[61] F. Stern, Phys. Rev. Lett. **18**, 546 (1967).

[62] U. Wulf and R. R. Gerhardts, in *Physics and Technology of Submicron Structures*, Vol. 83 of *Springer Series in Solid-State Sciences*, edited by H. Heinrich, G. Bauer and F. Kuchar (Springer-Verlag, Berlin, 1988), p. 162.

[63] I. S. Gradshteyn and I. M. Ryzhik, *Table of Integrals, Series, and Products* (Academic Press, New York, 1994).

[64] A. Siddiki and R. R. Gerhardts, International Journal of Modern Physics B **18**, 3541 (2004).

[65] A. Siddiki and R. R. Gerhardts, Phys. Rev. B **70**, 195335 (2004).

[66] H. Akera, J. Phys. Soc. Jpn. **70**, 1468 (2001).

[67] H. Akera, J. Phys. Soc. Jpn. **69**, 3174 (2000).

[68] T. Ando and Y. Uemura, J. Phys. Soc. Japan **36**, 959 (1974).

[69] T. Ando, Y. Matsumoto and Y. Uemura, J. Phys. Soc. Japan **39**, 279 (1975).

[70] M. Büttiker, Phys. Rev. B **38**, 9375 (1988).

[71] D. B. Chklovskii and P. A. Lee, Phys. Rev. B **48**, 18060 (1993).

[72] M. Büttiker, Phys. Rev. Lett. **57**, 1761 (1986).

[73] S. Datta, in *Electronic Transport in Mesoscopic Systems* (University press, Cambridge, 1995).

[74] M. Raikh and T. V-Shahbazyan, Phys. Rev. B **47**, 1522 (1993).

[75] S. Kraus private communication.

[76] J. P. Eisenstein, L. N. Pfeiffer and K. W. West, Appl. Phys. Lett. **57**, 2324 (1990).

[77] H. Rubel, A. Fischer, W. Dietsche, K. von Klitzing and K. Eberl, Mater. Sci. Eng. **57**, 207 (1998).

[78] L. I. Glazman and I. A. Larkin, Semicond. Sci. Technol. **6**, 32 (1991).

Acknowledgments

Yaşamak şakaya gelmez,
büyük bir ciddiyetle yaşayacaksın
bir sincap gibi mesela,
yani, yaşamanın dışında ve ötesinde hiç bir şey beklemeden,
yani bütün işin gücün yaşamak olacak.

I would like to express my sincere thanks to all those who helped me on my way to reach this page.
I am indebted to my Doktor-"Gross"-vater Professor Rolf R. Gerhardts, for his invaluable advises, critical suggestions and for sharing his wisdom. I am thankful for his patience and *self-consistency*.
Particular thanks go to:
Professor Klaus von Klitzing for creating a center for valuable colleagues, discussions and for giving me the opportunity to be a part of it.
Professor Reiner Kümmel for his really kind interest and refereeing.
Dr. Jürgen Weis, Dr. Erik Ahlswede and Frank Dahlem for fruitful discussions, which helped me to understand their measurements and "real" world.
Professor Werner Dietsche and Dr. Stefan Kraus, providing their kind interest, the experimental facilities and data.
Dr. Omar Stern, for his support, discussions and being my Mexican brother, that also includes being a good Fenerbahçe fan.
Dr. Sjoerd Lok, for his valuable criticisms, suggestions, "political" discussions and the clean-room journey.
I would also like to thank all the past and present members of the department and institute with

whom I have had the pleasure of working, learning and socializing during my time in Germany (almost in random order)
Eleonora Storace for nice dinners and the wind she brought from Mediterranean, Ulrike Waizmann for being a good "Schwäbische" host, Mark Lynass for his relaxing attitude and jokes, Martin Geisler for all his helps and being always kind to me, my office-mate Gerhard Ulbricht for his patience during this long period, Rodney Wiersma for long discussions about the meaning of life, Armin Welker for not leaving me alone while smoking, Denis Maryenko for being together at the coldest day that I ever seen, Dr. Kaan Güven for his assistance and encouragement at the beginning of my Ph.D work.
I am also indebted to the Turkish "mafia" in Max-Planck, Nuri Solak, Şahakalkan family, Sinan Balcı, Yener Kuru, Gürlü family and Arda Erhan Araç by whom I never felt alone in all "Bayrams" and sport events and especially to my recent home-mates Güliz and Hasan Çakmak for their kindness, patience and family "simulation" efforts during my stay at home.
I would like to extend my indebtedness to Dr. Alpan Bek for all the time interval that we have walked through.
I have to find a new language to express my gratitude to my family, to my mother, my Aba, my sister and my bilader.
Finally, I am most grateful to my wife, my friend, my collogue, my little sparrow for her patient and cheerful accommodation of many inconveniences, which, happily, are over now.

Lebenslauf

Name:	Afif SIDDIKİ
Geburtsdatum:	15.05.1973
Geburtsort:	Ankara, Türkei

1979-1984	Privat Grundschule Nese, Ankara
1984-1987	Yükselis-Gymnassium, Ankara
1987-1991	Ortadoğu-Gymnassium, İstanbul
1991-1997	B.Sc. an der İstanbul Technische Universität, İstanbul Thema: Canonical Transformation of Hubbard Hamiltonian to t-J Model.
1997-1999	M.Sc. an der Bilkent Universität, Ankara Thema: Low Temperature Thermodynamics of Finite and Discrete Quartic Quantum Oscillator in One Dimension
1999-2001	Gastwissenschaftler an der Nahost Technische Universität, Ankara
seit 08/01	Anfertigen der vorliegenden Dissertation am Max-Planck-Institut für Festkörperforchung Stuttgart, bei Prof. R. R. Gerhardts